

Numerical Studies for Membrane Viscous Effects on Red Blood Cell Dynamics in Flows

by

Ali Rezghi

A thesis submitted in partial fulfillment
of the requirements for the degree of
Master of Applied Science in Engineering Science

The Office of Graduate Studies
Laurentian University
Sudbury, Ontario, Canada

©Ali Rezghi, February 2022

THESIS DEFENCE COMMITTEE/COMITÉ DE SOUTENANCE DE THÈSE
Laurentian University/Université Laurentienne
 Faculty of Graduate Studies/Faculté des études supérieures

Title of Thesis Titre de la thèse	Numerical Studies for Membrane Viscous Effects on Red Blood Cell Dynamics in Flows	
Name of Candidate Nom du candidat	Ali Rezghi	
Degree Diplôme	Master of Science	
Department/Program Département/Programme	Engineering	Date of Defence Date de la soutenance February, 2022

APPROVED/APPROUVÉ

Thesis Examiners/Examineurs de thèse:

Dr. Junfeng Zhang
(Supervisor/Directeur(trice) de thèse)

Dr. Derek Gransden
(Committee member/Membre du comité)

Dr. Chris Lane
(Committee member/Membre du comité)

Dr. Tathagata Acharya
(External Examiner/Examineur externe)

Approved for the Office of Graduate Studies
 Approuvé pour la Faculté des études supérieures
 Dr. Tammy Eger
 Vice-President, Research
 Laurentian University

ACCESSIBILITY CLAUSE AND PERMISSION TO USE

I, **Ali Rezghi**, hereby grant to Laurentian University and/or its agents the non-exclusive license to archive and make accessible my thesis, dissertation, or project report in whole or in part in all forms of media, now or for the duration of my copyright ownership. I retain all other ownership rights to the copyright of the thesis, dissertation or project report. I also reserve the right to use in future works (such as articles or books) all or part of this thesis, dissertation, or project report. I further agree that permission for copying of this thesis in any manner, in whole or in part, for scholarly purposes may be granted by the professor or professors who supervised my thesis work or, in their absence, by the Head of the Department in which my thesis work was done. It is understood that any copying or publication or use of this thesis or parts thereof for financial gain shall not be allowed without my written permission. It is also understood that this copy is being made available in this form by the authority of the copyright owner solely for the purpose of private study and research and may not be copied or reproduced except as permitted by the copyright laws without written authority from the copyright owner.

Abstract

In this thesis, three-dimensional simulations are performed to investigate the effects of membrane viscosity on behaviors of red blood cells (RBCs) in simple shear flow and the migration processes of viscoelastic capsules in tube flow. The lattice Boltzmann method is used as the fluid solver, whereas the immersed boundary method is employed to capture the dynamic interaction between the flow and membrane. The RBC membrane follows the Skalak constitutive law for elasticity, and the resistances to area dilation and bending deformation are also included. In addition, the membrane viscosity is incorporated using the recently developed finite difference scheme. The methodology and computer programs are validated carefully by conducting several benchmark test simulations.

The lateral migration of viscoelastic capsules in tube flow is investigated in details with various combinations of viscosity ratio, membrane shear viscosity and capillary number. In general, the migration process starts with an initial transient phase, where the capsule deformation and migration velocity suddenly increase from zero to a maximum value. Following that, the deformation and migration velocity gradually reduce as the capsule moves toward the tube centerline. The capsule also performs continuous rotation during the migration, and the rotation gradually slows down with the capsule migration. The interior-exterior fluid viscosity contrast and the membrane viscosity have similar effects in reducing the capsule deformation and inclination angle to the flow direction; however, a strong membrane viscosity may introduce significant oscillations in the capsule deformation, inclination, and migration velocity. Due to the reduced capsule deformation, the migration velocity and capsule rotation become slower for capsules with higher viscosity contrast and/or membrane viscosity. Moreover, the influence of membrane viscosity on the migration dynamics intensifies at higher capillary number.

In addition, tank-treading behaviors of RBC in simple shear flow is scrutinized over a wide range of shear rate and exterior fluid viscosity. Detailed comparisons of the tank-treading frequency, deformation, and inclination angle of the cell with experiments are

conducted by considering different combinations of membrane and interior fluid viscosities. According to the results, tank-treading frequency diminishes with both membrane viscosity and internal fluid viscosity, although elevating the interior viscosity alone does not sufficiently retard the tank-treading motion to achieve favorable agreement with experimental results. This stronger impact of membrane viscosity has also been noticed for the cell deformation and inclination angle. In particular, including membrane viscosity is essential to reproduce experimental results for the cell orientation. Furthermore, the results indicate that a reasonable agreement can be obtained in comparison to experiments even without applying the shear-thinning model for membrane viscosity. Hence, more supporting evidence is required to justify necessity and applicability of shear-thinning models for membrane viscosity of RBCs. Suggestions for future research have been proposed as well.

Acknowledgements

I would like to express my sincere thanks to my supervisor, Professor Junfeng Zhang, for his guidance in my Master's program. I would also give my thank to my current and former lab colleagues, Ping Li, Mayssaa Jbeili, and Farhad Abbasi Amiri.

I am also grateful to my committee members, Dr. Tathagata Acharya, Dr. Derek Gransden, and Dr. Chris Lane for reading this thesis, attending the defense exam, and providing valuable comments.

Contents

Acknowledgements	v
1 Introduction	1
1.1 Background	1
1.2 RBC Behaviors in Flow Fields	3
1.3 Scope of the Thesis	4
2 Literature Review and Research Objectives	7
2.1 Experimental Techniques for RBC Mechanics	7
2.2 Numerical Methods	9
2.3 RBC Dynamics in Simple Shear Flow	11
2.4 Lateral Migration of Capsules	14
2.5 Motivations and Objectives	15
3 Theory and Methodology	17
3.1 The Lattice Boltzmann Method	17
3.2 The Immersed Boundary Method	20
3.3 RBC Membrane Mechanics	21
3.3.1 Membrane in-Plane Elasticity	23
3.3.2 Membrane Bending	24
3.3.3 Membrane Surface and Volume Energies	25
3.3.4 Membrane Viscosity	25
3.4 Finite-Difference Method for Membrane Viscosity in IBM Simulations	26
3.5 The Computational Procedure	28
4 Lateral Migration of Viscoelastic Capsules in Tube Flow	31

4.1	Model and Program Validations	31
4.1.1	Tank-Treading Dynamics of Elastic Capsule in Linear Shear Flow	31
4.1.2	Lateral Migration of a Neutrally-Buoyant Rigid Sphere	36
4.2	Simulation Setup for Capsule Migration in Tube Flow	38
4.3	Effect of Viscosity Ratio on Capsule Migration	39
4.4	Effect of Membrane Shear Viscosity on Capsule Migration	48
4.5	Effect of Capillary Number on Capsule Migration	51
4.6	Empirical Relationships for Migration Velocity and Rotation Period	56
4.7	Summary and Further Discussions	58
5	Membrane Viscous Effects on the Tank-Treading Dynamics of RBC in Simple Shear Flow	61
5.1	RBC Deformation Under External Stretching Load	61
5.2	Simulation Setup for Tank-Treading Dynamics of RBC	64
5.3	Membrane and Interior Viscous Effects on the Tank-Treading Dynamics of RBC	65
5.3.1	Tank-Treading Frequency	67
5.3.2	RBC Deformation	69
5.3.3	RBC Orientation	72
5.3.4	Assessment of Shear-Thinning Model for Membrane Viscosity	73
5.4	Summary and Concluding Remarks	75
6	Summary and Future Research	77
6.1	Summary	77
6.2	Future Research	78

List of Figures

1.1	Schematic illustration of microvascular networks in microcirculation with arteriole, capillaries and venule [2].	1
1.2	An overview of blood components in human bodies [4].	2
1.3	(a) A scanning electron microscope image of human RBCs [5] and (b) schematic view of RBC membrane structure [6].)	2
1.4	Typical behaviors of a RBC in simple shear flow. The numbers (1 to 3) and colors (black, blue, and red) indicate the successive shapes of the cell during (a) tank-treading, (b) tumbling, and (c) swinging motions. The circular symbols represent a membrane marker point to demonstrate the membrane rotation [21].	4
2.1	Examples of experimental techniques for measuring mechanical properties of RBCs: (a) micropipette aspiration [24]. (b) and (b') optical tweezers [28], and (c) rheoscope [29].	8
3.1	Schematic illustration of the D3Q19 lattice model. The cube is displayed by the solid black lines with edge length of $2\delta x/\delta t$. The lattice velocities \mathbf{e}_{1-18} are denoted by arrows starting from the cube center, whereas the lattice velocity \mathbf{e}_0 is indicated as a blue circle at the cube center.	20
3.2	2D illustration of IBM. The membrane nodes are indicated by the filled circles and the open circles display the fluid nodes. The membrane force acting on the membrane node \mathbf{x}_m is spread to the fluid nodes \mathbf{x}_f within the square region (dashed lines) using Eq. (3.8); and the membrane velocity $\mathbf{u}_m(\mathbf{x}_m)$ is interpolated from the local ambient flow within the square through Eq. (3.10) [75].	21

3.3	An example of recursive subdivision of an icosahedron for triangulation of (a) a sphere [78] and (b) RBC with a segment of the membrane enlarged; and (c) the membrane element convention for the bending energy. n_1 and n_2 represent the normal vectors of the two adjacent elements sharing the same edge j	22
3.4	Schematic views of (a) the Kelvin-Voigt model for modeling the membrane viscoelasticity (spring k represents the membrane elasticity and the membrane viscosity is indicated by dashpot μ) and (b) the standard linear solid model with an artificial spring k'	27
3.5	Schematic view of the simulation algorithm. It proceeds from the initialization step.	29
4.1	Schematic illustrations of (a) the imposed linear shear flow and (b) the deformed capsule shape in the shear plane with the largest axis L , smallest axis W , and the inclination angle θ . Also shown in (b) are the definitions for the rotation angle ϕ for a membrane marker (blue circle), the membrane rotation (red arrows), and the interior and exterior fluid viscosities μ_i and μ_o , respectively.	33
4.2	Schematic diagrams of the simulation setup for particle and capsule migration processes: (a) the side view along the Y direction, and (b) the axial view along the flow direction. The tube is represented by black lines and the particle/capsule is shown as red circles. See the text for more detailed information on the system parameters.	36
4.3	Lateral positions of the particle centroid as it migrates toward its equilibrium position in the tube flow. Results from previous publications are also shown for comparison.	37

- 4.4 Capsule shapes during migration in the tube flow for different viscosity ratios: (a) $\lambda = 1$, (b) $\lambda = 5$, and (c) $\lambda = 10$. These shapes are taken at the same lateral locations Z^* (labeled on top of a), and the corresponding time t^* at each Z^* is shown below the individual shape. The blue point represents a membrane marker point to demonstrate the capsule rotation during the migration. 40
- 4.5 Streamlines for the flow around and inside the capsule in the $Y = 0$ plane in (a) the original reference frame and (b) a reference frame moving with the velocity of the capsule centroid. The capsule shape is shown in red color and the vertical dashed lines show three representative axial positions: far from the capsule x_1 , on the center of capsule x_2 , and close to the capsule x_3 . The velocity profiles at these three representative axial positions are depicted in (c) along with the theoretical Poiseuille velocity profile. Here, $\lambda = 1$ and the capsule is at lateral location $Z^* = 0.25$ 42
- 4.6 Temporal evolution of (a) the lateral position and (b) the axial location of the capsule with different λ values. 43
- 4.7 Variations in (a1 and a2) the migration velocity, (b1 and b2) the axial velocity, and (c1 and c2) the slip velocity plotted with the migration time t^* (a1, b1, c1) and the lateral position Z^* (a2, b2, c2) at different λ values. Also shown in (b2) as a gray curve is the flow velocity from Eq. (4.2) for the undisturbed tube flow. 44
- 4.8 Evolutions of (a) the deformation index D and (b) the inclination angle θ versus the lateral location Z^* with different λ values. The filled symbols are plotted based on the D and θ results in shear flow at capillary number $Ca = 0.0375$ (Table 4.1). 46
- 4.9 Variations of (a) the rotation angle ϕ with migration time t^* and (b) the rotation period T^* with lateral location Z^* and local capillary number Ca^* . The filled symbols in (b) depict the converted tank-treading period TTP values for capsules in shear flow with $\lambda = 0.2, 1$, and 5 at $Ca = 0.0375$. . . 47

4.10	Effects of the membrane viscosity Bq_s on (a) the lateral location, (b) the migration velocity, and (c) the slip velocity during the migration process. Capsule shapes with different membrane viscosities are also compared in (d) at several time instants.	49
4.11	Effects of membrane viscosity Bq_s on (a) the capsule deformation and (b) the capsule orientation as a function of lateral position Z^*	50
4.12	Effects of the membrane viscosity Bq_s on (a) the rotation angle ϕ and (b) the rotation period T^* . Both the lateral position Z^* and the local capillary number Ca^* are labeled in (b) along the horizontal axis.	51
4.13	Effects of the capillary number Ca on (a) the lateral location, (b) the migration velocity, and (c) the slip velocity during the migration process. Here the viscosity ratio is $\lambda = 5$ and three different membrane viscosity values are considered: $Bq_s = 0, 10,$ and 40 . Capsule shapes with different Ca and Bq_s values are also compared in (d) at several time instants.	53
4.14	Effects of the capillary number Ca and membrane viscosity Bq_s on (a) the capsule deformation D and (b) the inclination angle θ . Both the lateral position Z^* (bottom) and the local capillary number Ca^* (top) are labeled along the horizontal axis. Please note that, since different capillary numbers Ca are used in these cases, the local capillary number Ca^* is different for cases with $Ca = 0.05$ and $Ca = 0.4$, even at a same position Z^* . The filled symbols represent the tank-treading results in shear flow for elastic capsules at capillary number $Ca = 0.0375$ and 0.075 with $\lambda = 5$	54
4.15	Effects of Ca and Bq_s on (a) the capsule rotation angles ϕ and (b and c) the rotation period T^* . Since the cases with $Ca = 0.05$ and 0.4 have different local capillary number Ca^* values at a same lateral position Z^* , the data points for $Ca = 0.05$ and 0.4 appear as two separate groups in the $T^* \sim Ca^*$ plot in (c). Also added there are the results (in red color) from Figs. 4.9b and 4.12b for $Ca = 0.2$, and the tank-treading results (filled symbols) for capsules with $\lambda = 0.2, 1$ and 5 at $Ca = 0.0375$ and 0.075	55

4.16	Comparisons of (a) the migration velocities and (b) the rotation periods from numerical simulations (symbols) with the predictions from Eqs. (4.5) and (4.6) (gray lines).	57
5.1	Schematic illustrations of (a) the undeformed RBC at rest with silica microbeads attached to the cell surface from opposite sides and (b) the elongated cell under external load of F . W is the transverse length of the cell and the axial lengths L_{min} , L_{middle} , and L_{max} are indicated based on different methods for calculating the axial length (see text for details).	62
5.2	Comparisons between (a) the axial L and transverse W lengths of the RBC and (b) the deformation index D_{xz} obtained from present simulations and those from optical tweezers experiments [101]. Also shown in (b) as green symbols are the simulation results from Tsubota [64].	63
5.3	Illustration of the deformed RBC subject to the simple shear flow. The projected length L_p and width B of the cell in XY plane are used to characterize the cell deformation as L_p/B . The inclination angle θ is defined as the angle between the flow direction and the major axis, and the membrane rotation is indicated by blue arrows.	64
5.4	Range of the exterior fluid viscosity μ_o and shear rate $\dot{\gamma}$ used in present simulations and experiments [30, 48, 49]. The conditions considered in Refs. [62, 64] are also shown for comparison.	66
5.5	Effects of membrane viscosity μ_s and interior fluid viscosity μ_i on tank-treading frequency TTF of the RBC in simple shear flow with different exterior fluid viscosities. The error bars for the present results indicate the minimum and maximum values of TTF , while the filled symbols present the mean values of TTF . The gray symbols with error bars indicate the experimental results from Fischer [30], where the measured TTF values for the cells of all 3 donors are included. Insets are also adopted to show more details.	68

5.6	Variations of TTF with respect to shear rate $\dot{\gamma}$ for different shear flow conditions, membrane viscosities, and interior fluid viscosities. The experimental results from Fischer [30] are also shown for comparison, and the insets are presented to show more details.	69
5.7	Comparison of the deformation index obtained from present simulations with experimental results of Fischer [30] for different shear flow conditions. The shear rate is presented in a logarithmic scale and the insets are adopted to present clearer views of the results.	70
5.8	Impact of membrane viscosity and interior fluid viscosity on the RBC deformation L_p/B with respect to shear stress $\mu_o\dot{\gamma}$. The shaded areas are calculated through linear regression of maximum and minimum values of L_p/B versus $\mu_o\dot{\gamma}$ (see the text for details).	71
5.9	Sensitivity of the RBC inclination angle to membrane viscosity and interior fluid viscosity for various flow conditions. The experimental results from Fischer and Korzeniewski [49] (FK 2015) are also presented for comparison.	72

Chapter 1

Introduction

1.1 Background

Blood is conveyed from heart to arteries, which branch into arterioles with inner diameter less than $100\ \mu\text{m}$. Further branching occurs along the length of arterioles, which leads to smaller vessels called capillaries with inner diameter of $5\sim 10\ \mu\text{m}$. The capillaries converge and combine to form venules, which continue to unite and become veins. At the end, the blood flow returns back to the heart through the venae cavae. Circulation of blood in these microvessels (arterioles, capillaries, and venules) is referred to as the microcirculation [1], as shown schematically in Fig. 1.1. The microvessels are the major sources of pressure losses in the circulatory system due to their small diameters. Furthermore, biological functions of blood, such as delivering oxygen and nutrition and removing metabolic wastes from tissues, are primarily accomplished within these small vessels.

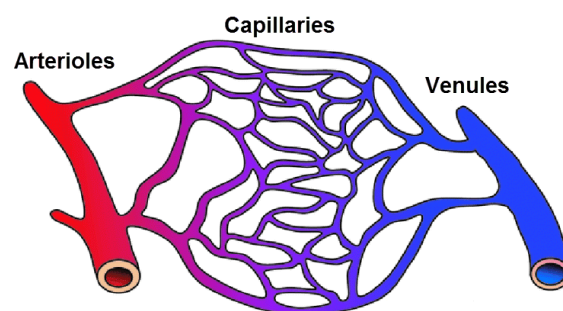


FIGURE 1.1: Schematic illustration of microvascular networks in microcirculation with arteriole, capillaries and venule [2].

Blood consists of plasma, erythrocytes (also called red blood cells, RBCs), white blood cells, and platelets, as shown in Fig. 1.2. The suspending fluid, plasma, is a dilute aqueous solution of proteins, glucose, and electrolytes, with a viscosity of ~ 1.2 cP. RBCs, with volume concentration (hematocrit) of 40% to 45% in an adult human body, vastly outnumber white blood cells and platelets. The stress-free shape of a healthy RBC is a biconcave disk, as shown in Fig. 1.3a, with a diameter of $\sim 8 \mu\text{m}$, a surface area of $\sim 140 \mu\text{m}^2$, and a volume of $\sim 90 \mu\text{m}^3$ [3]. Cytoplasm, the interior fluid of RBCs, is a high-concentration hemoglobin solution, and it can be considered as an incompressible and Newtonian fluid. The life span of RBCs is about 120 days: old RBCs are separated and dismantled in the spleen, and new RBCs are continuously produced in the bone marrow network. The large number density of RBCs along with their distinctive properties, such as the biconcave shape and high deformability, make them the most influential component for blood rheology.

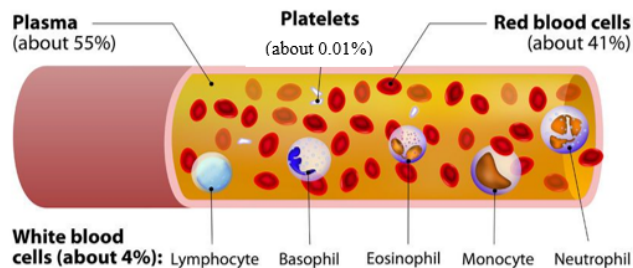


FIGURE 1.2: An overview of blood components in human bodies [4].

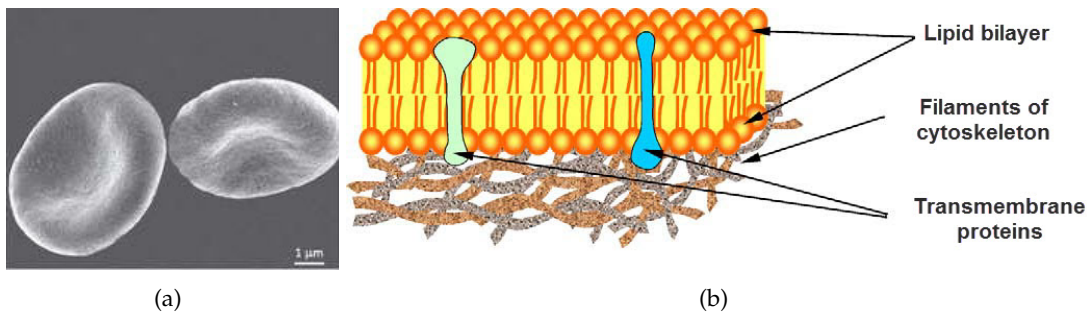


FIGURE 1.3: (a) A scanning electron microscope image of human RBCs [5] and (b) schematic view of RBC membrane structure [6].

For healthy metabolism in the body, RBCs need to deform from their original biconcave shape in order to travel through the microvascular network. The deformability of a RBC is determined by its geometry and membrane mechanics [7]. The RBC membrane, which is made up of a lipid bilayer, transmembrane proteins, and a cytoskeleton network, separates the interior cytoplasm and exterior plasma (Fig. 1.3b). The thickness of the membrane is ~ 10 nm, which is significantly small compared to the RBC diameter [8]. RBC membrane exhibits a large resistance to area dilation, but a low resistance to shear deformation, and certain bending elasticity [9]. Moreover, the RBC membrane shows viscous resistance to strain rate due to dynamic membrane deformation as demonstrated in many experimental measurements [10, 11, 12, 13, 14, 15]. From a physical point of view, the membrane viscous effect is induced by the fluid-like behavior of the lipid bilayer, while the elastic resistance is induced by the stretching of the cytoskeleton.

These mechanical properties of the membrane are typically characterized in terms of elastic shear modulus, bending and dilation moduli, and membrane viscosity [16]. In addition, clinical studies have found that various diseases, such as malaria and sickle cell anemia, can affect these RBC properties. For example, the sickle cell anemia leads to mis-shaped RBCs with low membrane deformability [1, 17].

1.2 RBC Behaviors in Flow Fields

For the important roles of RBCs in maintaining normal metabolism, substantial research has been devoted to investigate behaviors of RBCs in various flow fields. The RBC flow in microcirculation at normal hematocrit is complex because of RBC motion and deformation, wall-induced effects, nonuniformity of shear fields, and mutual interactions among them. To circumvent these complexities, many studies have investigated RBC dynamics in dilute suspensions. When suspended at low concentrations in a simple shear flow, RBCs may exhibit three types of motion (Fig. 1.4). With sufficiently high shear rates and/or exterior viscosity, the membrane rotates around the elongated cell in an approximately stable shape and the interior cytoplasm performs an eddy-like circulation flow [18, 19]. This motion is called tank-treading, as shown in Fig. 1.4a. This behavior can be observed for RBCs flowing near the arteriole wall, where a high shear rate exists. Another

type of motion is tumbling, which occurs usually at low shear rates, and the cell flips like a soft particle (Fig. 1.4b). At moderate shear rates between the tank-treading and tumbling modes, the cell can oscillate about a mean inclination angle, while its membrane rotates around the liquid inside. This motion has been observed by Abkarian et al. [20] for the first time and it is called the swinging motion.

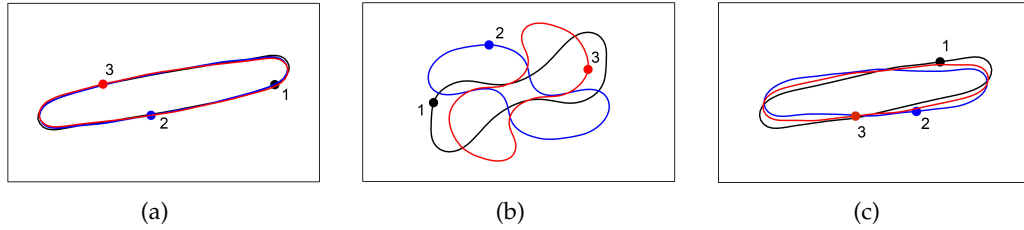


FIGURE 1.4: Typical behaviors of a RBC in simple shear flow. The numbers (1 to 3) and colors (black, blue, and red) indicate the successive shapes of the cell during (a) tank-treading, (b) tumbling, and (c) swinging motions. The circular symbols represent a membrane marker point to demonstrate the membrane rotation [21].

For flows of RBC suspensions in tubes, observations *in vitro* and *in vivo* have indicated that the apparent viscosity of blood decreases with the tube diameter as it reduces from $\sim 100 \mu\text{m}$. It attains a minimum at diameters of $\sim 5 - 7 \mu\text{m}$, which is related to the particular size of RBCs. This phenomenon is called the Fahraeus-Lindqvist effect [22], and it is attributed to the lateral migration of RBCs away from the tube wall, which leads to formation of a cell-free layer (CFL) around the tube periphery. Among others, factors responsible for this lateral migration include the flexibility of RBC membrane and the decreased shear gradient away from the tube wall. Presence of the CFL decreases the resistance to flow and plays a decisive role in hemodynamics [1]. In addition, when passing through narrow tubes with diameters comparable to the tube diameter, RBCs arrange themselves in a single file configuration [23].

1.3 Scope of the Thesis

In this thesis, the behaviors of RBCs in shear and tube flows are investigated via three-dimensional (3D) simulations to elucidate the effects of the membrane viscosity on the cell dynamics. Chapter 2 provides a review of the previous studies on RBC flow modeling and simulations and presents the motivations and objectives of this study. Chapter 3

details the the theory and methodology used in this thesis. The migration processes of viscoelastic capsules are accessed in Chapter 4, which is followed by the results for the effects of membrane viscosity on RBC dynamics in shear flow in Chapter 5. Chapter 6 presents the summary and major findings of the thesis, and outlines future work.

Chapter 2

Literature Review and Research

Objectives

This chapter presents a review of the relevant literature in RBC flow modeling and simulations. At first, the experimental measuring techniques and numerical methods are described. Then, previous studies on the tank-treading dynamics of RBC and lateral migration of capsules are reviewed. Finally, motivations and objectives of this thesis are presented.

2.1 Experimental Techniques for RBC Mechanics

During the past several decades, substantial research has been devoted to measure RBC mechanics and investigate their behavior experimentally. Researchers have utilized various techniques to measure RBC mechanical properties, such as micropipette aspiration [24], atomic force microscopy [25], rheoscopy [26], optical tweezers [27], and magnetic twisting cytometry [15].

Fig. 2.1 illustrates the basic setups and working principles of the micropipette aspiration, optical tweezers, and rheoscopy techniques. Mechanical behavior of RBC has been extensively studied using the micropipette aspiration method, in which the cell is aspirated into the mouth of the micropipette by applying a suction pressure (Fig. 2.1a). The aspiration pressure is adjusted using a manometer and the amount of the cell membrane aspirated into the micropipette can be measured using a microscope. This method has

been applied to measure mechanical properties of RBC, including shear, bending, and area compressibility moduli and membrane viscosity. For example, to measure the membrane viscosity, the suction pressure is removed after the RBC aspiration and the cell recovers its biconcave shape. The membrane viscosity can then be obtained by measuring the relaxation time of the cell [16].

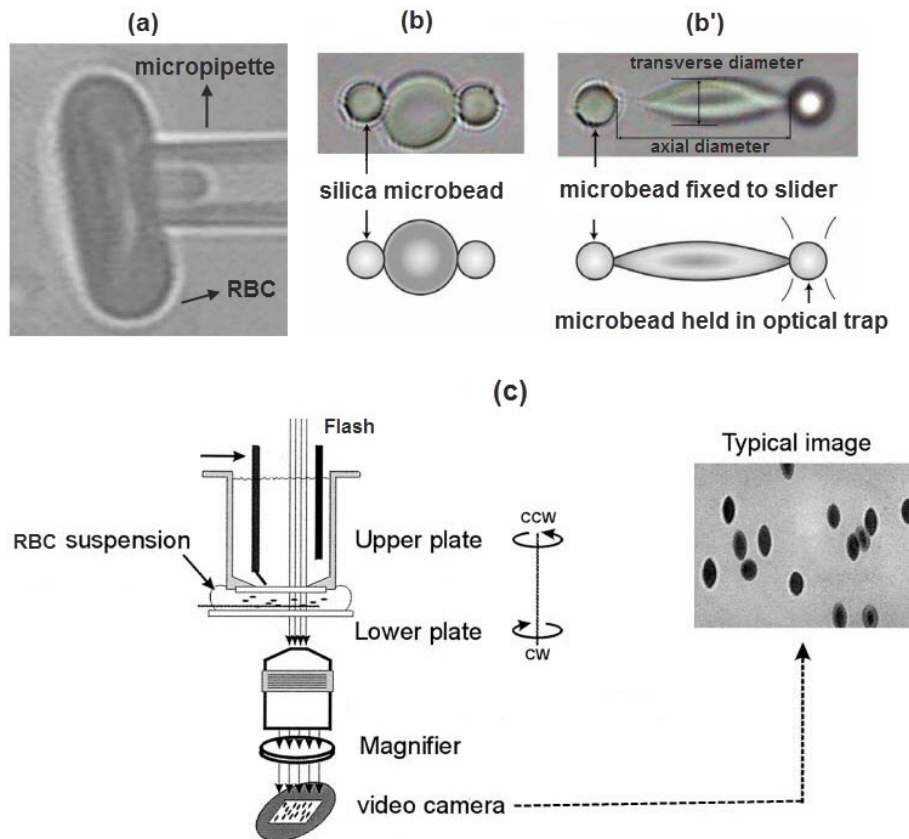


FIGURE 2.1: Examples of experimental techniques for measuring mechanical properties of RBCs: (a) micropipette aspiration [24]. (b) and (b') optical tweezers [28], and (c) rheoscope [29].

The mechanical properties of RBCs can also be measured using optical tweezers. In this technique, two microbeads adhere to the cell surface from opposite sides (Fig. 2.1b). Generally, one of the beads are optically trapped by focusing a laser beam on the bead and another one is attached to the surface of a slider. With the trapped bead remaining stationary, the cell undergoes tensile deformation by moving the slider. For instance, the elastic shear modulus of the RBC membrane can be obtained by measuring the diameters of the elongated cell [28]. Another approach for studying RBC mechanics is through

rheoscopy. A rheoscope (Fig. 2.1c) is generally comprised of a counter-rotating transparent cone-plate chamber, where RBCs are suspended at low hematocrits in a high-viscosity solution inside the chamber. This method generates a simple shear flow in the solution and provides useful means to analyze RBC dynamics in shear flow. For example, the tank-treading frequency of RBC can be determined by tracking marker particles attached to the cell surface [30].

A major challenge of these experimental methods is that the generated stress on the cells during measurements may not represent the real situation experienced by RBCs in microcirculation. In addition, the reported values for RBC mechanical properties from different techniques show large variations. Furthermore, the experiments are vulnerable to technical difficulties such as measurement inaccuracy and intraindividual distributions of cell parameters in the sample [31, 9].

2.2 Numerical Methods

RBC dynamics have been also investigated in theoretical studies, however, theoretical analyses are usually restricted to simplified situations with small deformations of the idealized cell shapes [32, 33]. Numerical investigations can then be a useful tool to investigate RBC behaviors in flow fields to avoid the difficulties in experimental studies and simplifications in theoretical analyses. RBC flow modeling can be performed by continuum approaches or explicit modeling of the cell. The main limitation of the continuum methods is that they cannot capture the dynamic deformations of cells and the mutual interactions between them. Therefore, explicit modeling of RBCs is a more appropriate approach for RBC flow simulations, particularly when RBC diameter is comparable to the vessel size [34, 35]. Typical numerical methods for blood flow simulations that can account the particulate nature of blood include the boundary integral method (BIM), dissipative particle dynamics (DPD), and immersed boundary method (IBM). Unlike conventional approaches that use body-conformal mesh, BIM, DPD, and IBM do not require mesh regeneration and hence they are computationally more efficient.

With the Reynolds number of blood flow in the microcirculation being small (typically

lower than 0.2 [1]), the boundary integral method can be adopted to solve the linear Stokes equation using the Greens function techniques and taking surface integrals over the membranes and boundaries. A comprehensive description of the method can be found in Ref. [36]. BIM has been employed in simulations of several RBC phenomena, including RBC tank-treading motion [37]. An advantage of this method is that it only demands discretization of the surfaces. However, its computational efficiency can be of concern as the number of cells in the flow field increases [38]. In addition, the BIM cannot incorporate finite inertia and it is also difficult for complex boundary geometry.

The dissipative particle dynamics can be considered as a coarse-grained molecular dynamics method, which was initially developed for mesoscale simulation of complex fluids. In DPD, the fluid is represented by particles interacting with each other by conservative, dissipative, and random forces, and their motion is governed by the Newton's second law. DPD has been adopted in investigating the stretching process and tank-treading dynamics of RBC and a good agreement was found in comparison to experimental results [39]. A particular benefit of using DPD for RBC simulations is that the cell membrane can be conveniently modeled as a layer of particles. However, DPD demands a large number of particles, particularly at regions with sharp cell edges, which is computationally expensive [35].

The immersed boundary method was originally developed by Peskin [40] in the 1970s to simulate the blood flow in the heart and later, Eggleton and Popel [41] employed this method to simulate dynamics of a RBC in a shear flow. In IBM, the boundary is represented by a Lagrangian mesh and the fluid is solved on an Eulerian mesh. The interaction between the boundary and the surrounding fluid is accomplished via force distribution and velocity interpolation steps. A detailed description of IBM is provided in Chapter 3. Since the Lagrangian and Eulerian meshes do not need to conform to each other, the cumbersome task of mesh regeneration is obviated. A further advantage of IBM is that it is not restricted to any specific numerical schemes and can be adopted in different numerical flow solvers [42]. Due to these benefits, IBM has become a popular choice to study motion and deformation of RBCs in two-dimensional (2D) [19, 43] and 3D [9, 44] simulations.

2.3 RBC Dynamics in Simple Shear Flow

From the fluid mechanics point of view, RBCs can be considered as capsules (liquid drops surrounded by deformable membranes) and the complex molecular structure of the cell membrane is neglected [45, 46]. Single RBC freely suspended in simple shear flow may experience tumbling, swinging, or tank-treading motions, as mentioned in Chapter 1. Studying these behaviors of RBC is of significant importance. For instance, the tank-treading frequency (TTF) of RBCs can serve as a sign for pathological disorders.

The tank treading dynamics of RBCs in simple shear flow have already been extensively investigated experimentally [47, 30, 20, 48, 49]. Under this flow field, the cell gradually elongates and aligns itself with an angle from the flow direction. In the meantime, the membrane rotates around the interior fluid similar to the tread of a tank. Several definitions have been employed to characterize the tank-treading dynamics, including the deformation index, inclination angle, and tank-treading frequency. Of particular interest is the study conducted by Fischer [30], where RBCs were suspended at low concentration in a high-viscosity solution, and the RBC rotation frequency was measured in a rheoscope (Fig. 2.1c). Later, RBC deformation index [48] and inclination angle [49] have also been measured. The results showed that at higher shear rates the frequency increases, with a faster slope in a more viscous solution. Furthermore, it was found that the impact of suspending viscosity on the cell elongation is more important than that from the shear rate. However, relatively large variations in elongation were observed.

The tank-treading motion of RBCs has been also studied theoretically and numerically. An early theoretical study was performed by Keller and Skalak [33], in which they modeled the cell as an ellipsoid with its surface rotating. This theory is not capable of predicting the swinging motion of RBCs and shear rate-dependent transition from tank-treading to tumbling. For the first time, Eggleton and Popel [41] conducted 3D simulations on RBC dynamics in linear shear flow. They calculated the cell shapes and deformation, however, their simulations became unstable due to membrane buckling resulted from neglecting the membrane bending properties. Pozrikidis [50] included the RBC membrane elasticity and bending resistance to simulate the cell dynamics in a simple shear flow. The results

indicated that the RBC undergoes a flipping motion accompanied by periodic deformations, however, numerical instabilities were encountered. Sui et al. [51] carried out numerical simulations on the swinging motion of RBC and the shear rate induced transition from swinging to tumbling motion. They also calculated the tank-treading frequency of the cell, although formation of wrinkles on the cell membrane was observed due to a lack of bending resistance. Similarly, Yazdani et al. [52] investigated the tank-treading and tumbling motions of a RBC in a simple shear flow over a broad range of viscosity ratio and shear rate. They found a nonmonotonic behavior between the tank-treading frequency and shear rate, and attributed this to the breathing-like dynamics of the cell. However, the calculated frequencies showed a relatively poor agreement with experimental results of Fischer [30]. Oulaid et al. [9] used realistic cell properties to simulate the tank-treading motion of a RBC with different values of viscosity ratio and shear rate. Their results for tank-treading frequency and deformation of the cell were in good agreement with experimental observations, although the cell orientation was not compared to experimental results.

The above mentioned studies did not consider RBC membrane viscosity. The RBC membrane shows viscous resistance to the temporal change in membrane strain, which is characterized by the membrane viscosity. Although membrane viscosity is acknowledged as an important part of the membrane mechanics, its impacts on RBC or capsule dynamics in simple shear flow are not well addressed. An early theoretical study on viscoelastic capsules in a linear shear flow was performed by Barthes-Biesel and Sgaier [53], in which a small-deformation theory was developed and their results indicated that the membrane viscosity restricts the capsules deformation. Such theoretical approaches are not applicable to cells with large deformation as in most natural and practical situations. Yazdani and Bagchi [54] applied the standard-linear-solid (SLS) model with the immersed boundary method to simulate the large deformation of viscoelastic capsules in shear flow. It was observed that the membrane viscosity diminishes the membrane deformation and causes oscillations in the capsule orientation and deformation. These oscillations have been also observed in simulations of Gounley and Peng [55] for a spherical capsule in a linear shear flow. Recently, Li and Zhang [56] developed a finite difference method to incorporate the

membrane viscosity for immersed boundary simulations. The efficiency, accuracy and stability have been analyzed meticulously [57], and it has recently been employed for viscoelastic capsules [57] in shear flow, and also RBC relaxation processes after being stretched in shear flow or by optical tweezers [58, 59].

Regarding the tank-treading dynamics of RBCs, Fedosov and co-workers [39, 60] presented a multiscale RBC model within the framework of dissipative particle dynamics with considering membrane viscosity. They calculated the tank-treading frequency of the cell in a simple shear flow and found a good agreement in comparison to the experimental results of Fischer [30]. However, they did not provide any comparison for the cell deformation and orientation. In addition, the membrane viscosity in this study had the unit of $\text{Pa} \cdot \text{s}$, which is different from the classical membrane viscosity definition (unit $\text{N} \cdot \text{s}/\text{m}$) [14]. Guglietta et al. [61] analyzed the impact of the membrane viscosity on the tumbling to tank-treading transition of a RBC in a simple shear flow. The authors found a qualitatively similar but quantitatively distinct behavior for membrane viscosity and viscosity ratio, particularly at small values. Although they did not report the effect of membrane viscosity on the tank-treading frequency of the cell, their results indicated that the membrane viscosity should be incorporated for realistic description of RBC dynamics. Matteoli et al. [62] also investigated the tank-treading motion of RBC with viscoelastic membrane and successfully validated the calculated tank-treading frequency against experimental results. However, similar to Refs. [39, 60], no validation tests were performed for the cell deformation and orientation. In addition, they applied a shear-thinning model for the membrane viscosity by considering higher membrane viscosity at smaller shear rates. In this way, the authors used different values for the membrane viscosity at different shear rates to reproduce the experimental results with less than 5% difference. Although the membrane viscosity can change with shear rate [63, 14], attempting to obtain good agreement with the experiments by adjusting the membrane viscosity could be open to question, particularly when the cell deformation and inclination angle are not taken into account. Tsubota [64] used the boundary element method to investigate the effect of membrane viscosity on the tank-treading motion of a RBC. Similar to Ref. [62], the author applied the shear-thinning model for the membrane viscosity and achieved a good

agreement for the cell deformation and tank-treading frequency in comparison to the experimental results. However, several concerns exist there: before presenting the results for the cell tank-treading motion, the author simulated the stretch testing of a RBC with optical tweezers and found a relatively poor agreement in comparison to experimental results. Then, the impact of membrane viscosity on the tank-treading dynamics of the cell was accessed by considering the shear-thinning model. Although the experimental results are available for several suspending viscosities, such as 14.6, 28.9, and 55.9 cP, the simulation results were compared only for one specific suspending viscosity (28.9 cP). Last but not least, no validation tests were conducted for the cell orientation.

2.4 Lateral Migration of Capsules

As mentioned in Chapter 1, due to the lateral (cross-stream) migration of RBCs away from the microvessel wall, the cell depleted layer or cell free layer is formed. This cell depleted layer reduces the apparent viscosity of blood flow and plays a key role in hemodynamics [1]. The significance of understanding this migration is not restricted to RBC flow in microcirculation, but also has other significant applications. For instance, the lateral migration of capsules in fluid flows is of paramount importance in biomedical applications, such as particle separating devices [65]. It should be mentioned that the migration process of RBCs in microvessels is more complicated compared to the RBCs dynamics in simple shear flow because of the wall-induced effects and variations of gradient of shear, among others. In addition, including the membrane viscosity increases the complexity of the problem.

In absence of the inertia effect at small Reynolds number, there are three mechanisms responsible for the lateral migration of deformable particles in flows: the wall-induced lift force, the presence of shear gradient, and the mutual interactions between the particles [66]. Capsule migration in unbounded parabolic flow was investigated theoretically by Helmy and Barthes-Biesel [67]. Their results showed that the capsule continuously migrates toward the flow axis, however, with the migration velocity gradually reduced with the flow shear rate. This study was limited to small capsule deformation and the

wall effect was not considered. Pozrikidis [68] used the BIM to investigate capsule migration in a tube flow, and found that an initially spherical capsule migrates toward the tube centerline, at a faster speed for a more flexible membrane. Again the wall effect is neglected by releasing the capsule at a relatively large distance from the tube wall. To include the wall effect, Nix et al. [69] assumed a linear superposition of the lift effects from the unbounded parabolic flow and the linear shear flow, and showed that the wall effect dominates the migration velocity when the capsule is close to the surface. In addition, Doddi and Bagchi [70] carried out immersed boundary simulations for the migration process of a single spherical capsule in the planar Poiseuille flow. The impacts of viscosity ratio, capillary number, and degree of confinement on the cell deformation, orientation, migration, and slip velocities were systematically examined. However, the planar flow configuration is not a realistic representation of microvessel geometry.

The above mentioned studies on capsule lateral migration have only considered the elastic membrane stresses, and hence the role of membrane viscosity in the capsule migration processes is still unclear.

2.5 Motivations and Objectives

As discussed above, in most of the studies on RBC dynamics in flow fields, the membrane viscosity was neglected. There have been a few studies that address the effects of membrane viscosity on RBC tank-treading motion in simple shear flow, generally without a detailed study of its effects. In addition, based on my up-to-date literature search, the impact of membrane viscosity on lateral migration of a RBC or capsule in tube flow has not been investigated. To fill these gaps, the following specific objectives are pursued in my research:

1. To develop computer programs to simulate RBC dynamics in simple shear flow and the migration processes of viscoelastic capsules in tube flows.
2. To validate the models, algorithms, and computer programs by performing benchmark test simulations.

3. To investigate the impact of membrane viscosity on RBC deformation, inclination angle, and tank-treading frequency and compare the results with previously published experimental studies.
4. To study the membrane viscosity effects on dynamics and migration process of viscoelastic capsules in tube flow.

Chapter 3

Theory and Methodology

The relevant theory, models, and numerical techniques used in this work are presented in this chapter. At first, the lattice Boltzmann method (LBM) is described, which is used as the fluid solver. Then, the framework and formulations of the immersed boundary method (IBM) are presented to explain the mechanism for capturing the dynamic interaction between the flow and the RBC membrane. In addition, the RBC membrane mechanics and models are described with a focus on the membrane viscosity. Finally, the numerical procedure is presented.

3.1 The Lattice Boltzmann Method

As mentioned in Chapter 1, RBCs are suspended in plasma, a dilute aqueous solution of proteins, glucose, and electrolytes. The interior fluid, cytoplasm, is a high-concentration hemoglobin solution. Both of these fluids can be considered as Newtonian fluid. In continuum fluid mechanics, the flow field of an incompressible fluid is governed by the continuity and momentum equations:

$$\begin{aligned} \nabla \cdot (\rho \mathbf{u}) &= 0 \quad , \\ \rho \left[\frac{\partial \mathbf{u}}{\partial t} + (\mathbf{u} \cdot \nabla) \mathbf{u} \right] &= - \nabla p + \mu \nabla^2 \mathbf{u} + \mathbf{F}_f \quad , \end{aligned} \tag{3.1}$$

where ρ represents the fluid density, \mathbf{u} is the fluid velocity, p is the pressure, and μ is the dynamic viscosity of fluid. The body force on the fluid, \mathbf{F}_f , can arise from an external effect (such as the gravitational field), or the flow-membrane interaction in the

immersed boundary treatment to be described in Section 3.2. In the present work, the lattice Boltzmann method [71] is applied to solve these equations. In LBM, the fluid mass is represented by distribution functions, in which consecutive propagation and collision processes are accomplished over a discrete lattice mesh. Owing to its particulate nature and local dynamics, LBM has several benefits over other fluid solvers, particularly for systems with complex boundaries and parallel computing implementation [71].

In LBM, a fluid is modeled as pseudo-particles moving over a lattice domain at discrete time steps. The density distribution $f_i(\mathbf{x}, t)$ indicates the particle amount moving with the i -th lattice velocity \mathbf{e}_i at position \mathbf{x} and time t . Since $\mathbf{e}_0 = (0, 0, 0)$ in most lattice models, f_0 represents the amount of particle that does not move at all. When one time step δt is elapsed, $f_i(\mathbf{x}, t)$ reaches its adjacent lattice site $\mathbf{x} + \mathbf{e}_i \delta t$ in the direction of the lattice velocity \mathbf{e}_i . This process is usually called the streaming or propagation process. In the meantime, other particles arrive at this same site from different directions, and therefore, collision among them will occur at this site, which alters distribution of the particle along each direction. Subsequently, a new set of density distributions leave the collision site in different lattice velocities, and next streaming process follows. These streaming and collision operations are repeated till satisfactory results are obtained. The above mentioned dynamics can be described by the lattice Boltzmann equation (LBE)

$$f_i(\mathbf{x} + \mathbf{e}_i \delta t, t + \delta t) - f_i(\mathbf{x}, t) = \Omega_i(f) \quad , \quad (3.2)$$

where Ω_i denotes the collision operator that incorporates the change in f_i caused by the particle collision. The left-hand side of Eq. (3.2) indicates the streaming step as discussed above. In presence of an external body force \mathbf{F}_f (such as gravity) or the distributed membrane force, a forcing term f_i^F [72] can be added to the right-hand side of Eq. (3.2),

$$f_i^F = w_i \left(1 - \frac{1}{2\tau} \right) \left(\frac{\mathbf{e}_i - \mathbf{u}}{c_s^2} + \frac{\mathbf{e}_i \cdot \mathbf{u}}{c_s^4} \mathbf{e}_i \right) \cdot \mathbf{F}_f \quad . \quad (3.3)$$

Here, c_s and w_i are lattice sound speed and weight factors, respectively. In the LBM development, an important simplification is to express the collision operator with the

Bhathagar-Gross-Krook (BGK) single relaxation time approximation, which was originally proposed for the Boltzmann equation in continuum kinetic theory [73]. In this treatment, it is assumed that f_i linearly evolves toward an equilibrium distribution f_i^{eq} with a relaxation time τ . The collision operator can then be expressed as:

$$\Omega_i(f) = -\frac{f_i(\mathbf{x}, t) - f_i^{eq}(\mathbf{x}, t)}{\tau} . \quad (3.4)$$

The equilibrium distribution f_i^{eq} can be expressed as:

$$f_i^{eq} = \rho w_i \left[1 + \frac{\mathbf{u} \cdot \mathbf{e}_i}{c_s^2} + \frac{1}{2} \left(\frac{\mathbf{u} \cdot \mathbf{e}_i}{c_s^2} \right)^2 - \frac{\mathbf{u} \cdot \mathbf{u}}{2c_s^2} \right] . \quad (3.5)$$

Here the fluid density ρ and velocity \mathbf{u} can be readily obtained from the density distributions at each lattice site through

$$\rho = \sum_i f_i \quad , \quad \mathbf{u} = \frac{\sum_i f_i c_i}{\rho} + \delta t \frac{\mathbf{F}_f}{2\rho} . \quad (3.6)$$

Typical D2Q9 (two dimensional, with nine velocities) square and D3Q19 (three dimensional with nineteen velocities) cubic lattice structures are commonly utilized in LBM simulations among many other options. In this study, the D3Q19 (Fig. 3.1) lattice model is adopted, and the 19 lattice velocities are

$$\begin{pmatrix} e_0 \\ e_1 \\ e_2 \\ \vdots \\ e_{18} \end{pmatrix}^T = \begin{bmatrix} 0 & 1 & 0 & -1 & -1 & 0 & 0 & 1 & -1 & -1 & 1 & 1 & -1 & -1 & 1 & 0 & 0 & 0 & 0 \\ 0 & 0 & 1 & 0 & 0 & 0 & 0 & 1 & 1 & -1 & -1 & 0 & 0 & 0 & 0 & 1 & -1 & -1 & 1 \\ 0 & 0 & 0 & 0 & -1 & 1 & -1 & 0 & 0 & 0 & 0 & 1 & 1 & -1 & -1 & 1 & 1 & -1 & -1 \end{bmatrix} \begin{pmatrix} \delta x \\ \delta t \end{pmatrix} , \quad (3.7)$$

where δx and δt are the lattice length unit and time step, respectively. For the D3Q19 model, $c_s = (1/\sqrt{3})\delta x/\delta t$ and $w_0 = 1/3, w_{1-6} = 1/18, w_{7-18} = 1/36$.

Through the Chapman-Enskog expansion [74], the macroscopic continuity and momentum (Navier-Stokes) equations (Eq. 3.1) can be recovered from the above defined LBM dynamics with the fluid viscosity expressed as $\mu = (2\tau - 1)c_s^2\delta t/2\rho$, and the fluid pressure given by $p = c_s^2\rho$.

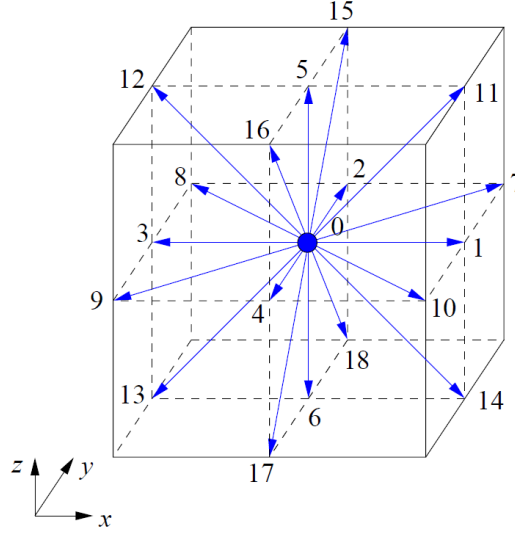


FIGURE 3.1: Schematic illustration of the D3Q19 lattice model. The cube is displayed by the solid black lines with edge length of $2\delta x/\delta t$. The lattice velocities \mathbf{e}_{1-18} are denoted by arrows starting from the cube center, whereas the lattice velocity \mathbf{e}_0 is indicated as a blue circle at the cube center.

3.2 The Immersed Boundary Method

Fig. 3.2 illustrates a 2D representation of a segment of the cell membrane immersed in the fluid domain. As the membrane deforms with the fluid flow, internal stresses are developed regarding the constitutive model of the membrane material, as to be discussed in Section 3.3. In the framework of IBM, the dynamic interaction between the flow and the membrane is captured via the force distribution and the velocity interpolation steps.

In the force distribution step, the membrane force \mathbf{F}_m computed at a membrane node \mathbf{x}_m is to be spread to the local fluid nodes \mathbf{x}_f as body forces \mathbf{F}_f using a discrete delta function $D(\mathbf{x})$:

$$\mathbf{F}_f(\mathbf{x}_f) = \sum_{\mathbf{x}_m} D(\mathbf{x}_f - \mathbf{x}_m) \mathbf{F}_m(\mathbf{x}_m) \quad , \quad (3.8)$$

$$D(\mathbf{x}) = \frac{1}{(4\delta x)^3} \left(1 + \cos \frac{\pi x}{2\delta x}\right) \left(1 + \cos \frac{\pi y}{2\delta x}\right) \left(1 + \cos \frac{\pi z}{2\delta x}\right) \quad , \quad (3.9)$$

$$|x| \leq 2h \quad , \quad |y| \leq 2h \quad , \quad \text{and} \quad |z| \leq 2h$$

$$D(\mathbf{x}) = 0, \quad \text{otherwise.}$$

Here, x , y , and z are the three elements of location vector \mathbf{x} , and $h = \delta x$ is the lattice grid resolution.

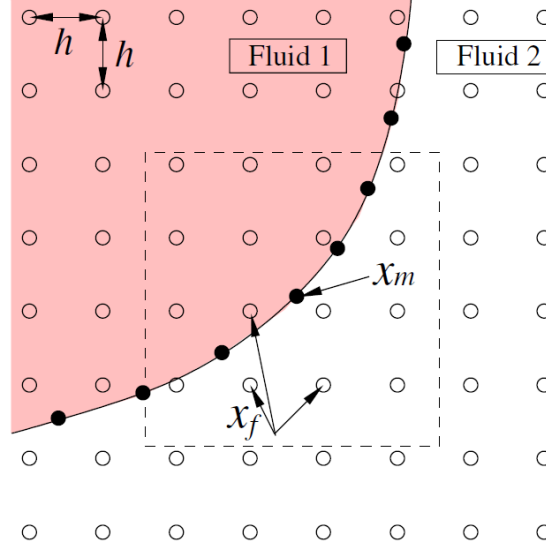


FIGURE 3.2: 2D illustration of IBM. The membrane nodes are indicated by the filled circles and the open circles display the fluid nodes. The membrane force acting on the membrane node \mathbf{x}_m is spread to the fluid nodes \mathbf{x}_f within the square region (dashed lines) using Eq. (3.8); and the membrane velocity $\mathbf{u}_m(\mathbf{x}_m)$ is interpolated from the local ambient flow within the square through Eq. (3.10) [75].

To ensure that the no-slip boundary condition is satisfied, in the velocity interpolation step, the membrane velocity $\mathbf{u}_m(\mathbf{x}_m)$ is calculated from the local flow field \mathbf{u} also via the function $D(\mathbf{x})$:

$$\mathbf{u}_m(\mathbf{x}_m) = h^3 \sum_{\mathbf{x}_f} D(\mathbf{x}_f - \mathbf{x}_m) \mathbf{u}(\mathbf{x}_f) \quad . \quad (3.10)$$

Here, the summation runs over all fluid nodes with $D(\mathbf{x}) > 0$. Once the membrane node velocity \mathbf{u}_m is calculated from Eq. (3.10), its position can then be updated, for example, using the Euler approximation, accordingly. More detailed descriptions of the IBM are provided in the literature [40, 76, 42].

3.3 RBC Membrane Mechanics

Healthy RBCs of human have a biconcave disk shape at rest, which can be described by [12]:

$$\bar{z} = 0.5(1 - \bar{r}^2)^{0.5} (c_0 + c_1 \bar{r}^2 + c_2 \bar{r}^4) \quad , \quad (3.11)$$

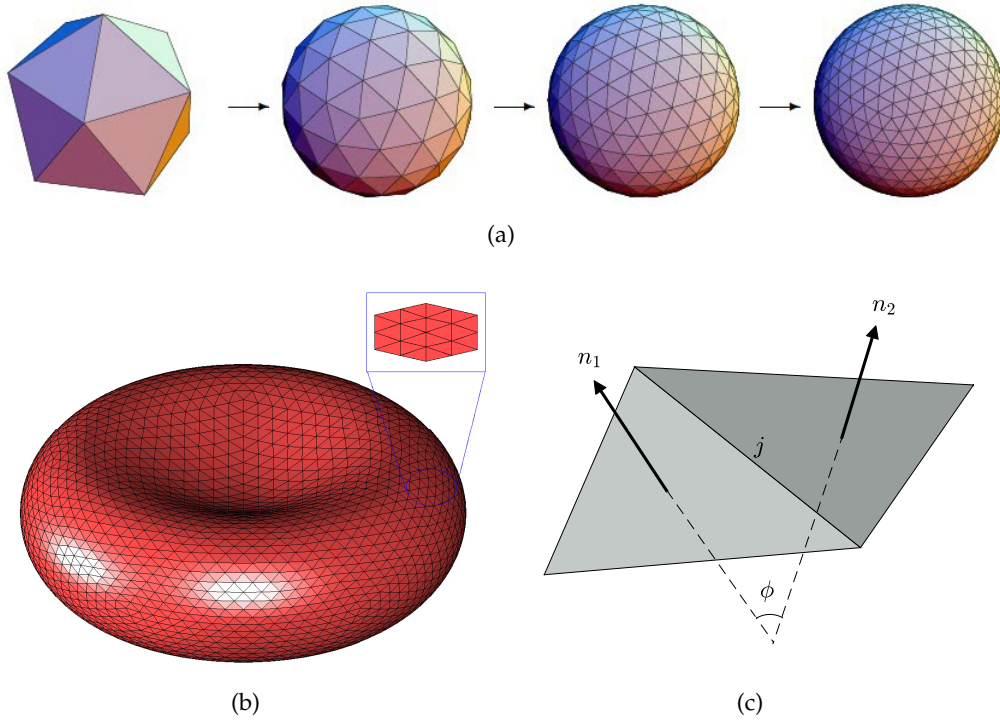


FIGURE 3.3: An example of recursive subdivision of an icosahedron for triangulation of (a) a sphere [78] and (b) RBC with a segment of the membrane enlarged; and (c) the membrane element convention for the bending energy. n_1 and n_2 represent the normal vectors of the two adjacent elements sharing the same edge j .

where \bar{z} and \bar{r} are dimensionless coordinates based on the RBC radius, and the shape parameters are $c_0 = 0.207$, $c_1 = 2.002$, and $c_2 = -1.122$. In this thesis, the 3D RBC membrane is discretized into flat triangular elements from an icosahedron using recursive subdivision [37, 77], as shown in Fig. 3.3a and b. The geometry of each triangular element is determined by the positions of its three vertices.

For an elastic membrane, deformation of the membrane elements generates forces on the membrane nodes. To obtain these nodal forces, the finite element membrane model developed by Charrier et al. [79] is adopted. The main idea is that the forces exerted on the vertices of each deformed element are calculated from the displacements of its vertices, assuming that the elements preserve their flat geometry. Subsequently, the constitutive law of the membrane material is used to find the relation between the membrane stress and membrane deformation. Then, forces at the membrane nodes can be calculated by applying the principle of virtual work [79].

For RBCs, in addition to the elasticity, the membrane exhibits resistance to bending deformation. Furthermore, surface and volume energies are often considered to penalize and diminish area and volume deviations in numerical simulations. To incorporate the forces due to these aspects, the total membrane energy is defined as [38, 9]

$$W = W_s + W_b + W_A + W_V \quad , \quad (3.12)$$

where W_s , W_b , W_A , and W_V are the total strain, bending, area, and volume energies, respectively. Accordingly, the membrane force \mathbf{F}_m at a location \mathbf{x}_m on the membrane can be obtained via the virtual work principle as

$$\mathbf{F}_m(\mathbf{x}_m) = -\frac{\partial W}{\partial \mathbf{x}_m} \quad . \quad (3.13)$$

Finally, the forces due to the membrane viscosity are calculated and added to the force term in equation 3.13. In the following, the strain, bending, area, and volume energies of RBC are described and then, a detailed discussion on the modeling of the membrane viscosity will be presented.

3.3.1 Membrane in-Plane Elasticity

The RBC membrane can be treated as a 2D sheet since its thickness is very small compared to its size. Skalak et al. [8] developed the following constitutive model for strain energy function for the elastic stress caused by the membrane in-plane deformation:

$$W_s = \frac{E_s}{8} \int [(I_1^2 + 2I_1 - 2I_2) + CI_2^2] dA \quad (3.14)$$

where E_s is the shear modulus, and $C = E_a/E_s$ is dilation coefficient. The membrane of RBCs are nearly area incompressible with a large dilatation module E_a , and hence, the value of C is large. I_1 and I_2 are the strain invariants of the 2D membrane, which can be calculated as functions of the two principle stretch ratios ϵ_1 and ϵ_2 :

$$I_1 = \epsilon_1^2 + \epsilon_2^2 - 2 \quad ; \quad I_2 = \epsilon_1^2 \epsilon_2^2 - 1 \quad . \quad (3.15)$$

The elastic stress tensor $\boldsymbol{\tau}^e$ can then be obtained from the energy function as [80, 8]

$$\boldsymbol{\tau}^e = \frac{1}{\epsilon_2} \frac{\partial W_s}{\partial \epsilon_1} \mathbf{e}_1 \otimes \mathbf{e}_1 + \frac{1}{\epsilon_1} \frac{\partial W_s}{\partial \epsilon_2} \mathbf{e}_2 \otimes \mathbf{e}_2 \quad , \quad (3.16)$$

where

$$\tau_1^e = \frac{1}{\epsilon_2} \frac{\partial W_s}{\partial \epsilon_1} \quad ; \quad \tau_2^e = \frac{1}{\epsilon_1} \frac{\partial W_s}{\partial \epsilon_2} \quad ; \quad (3.17)$$

are the two principle stresses; and \mathbf{e}_1 and \mathbf{e}_2 are their corresponding directions. The principle directions \mathbf{e}_1 and \mathbf{e}_2 can be obtained as the unit eigenvectors of the left Cauchy-Green deformation tensor $\mathbf{G} = \mathbf{F}\mathbf{F}^T$ with \mathbf{F} as the deformation gradient matrix [54, 77]. With the membrane being discretized into triangular elements, the matrix \mathbf{F} can be readily calculated by comparing the deformed and original configurations of each element [79]. Using the matrices \mathbf{G} or \mathbf{F} , the strain tensor \mathbf{E} is calculated as

$$\mathbf{E} = \frac{1}{2}(\mathbf{G}^T - \mathbf{1}) = \frac{1}{2}(\mathbf{F}^T\mathbf{F} - \mathbf{1}) \quad . \quad (3.18)$$

Other constitutive models has also been proposed, such as the neo-Hookean law [41]. Although the cell dynamics of Skalak and neo-Hookean membranes are similar at small deformations, they exhibit, respectively, strain-hardening and strain-softening behaviors at large deformations [81]. In this thesis, the Skalak constitutive law is employed as it is able to reproduce experimental data of RBCs at both small and large deformations [38].

3.3.2 Membrane Bending

The RBC membrane also exhibits resistance to bending deformation, particularly in regions with large local curvatures. The simplified Helfrich expression is applied to model the bending resistance on the triangular mesh [82, 38]:

$$W_b = \frac{E_b}{2} \sum_j (\phi - \phi_0)^2 \quad . \quad (3.19)$$

Here, E_b is the bending modulus and ϕ denotes the angle between the outward normal vectors of the two neighboring face elements sharing the same edge j , as shown in Fig. 3.3c. ϕ_0 is the initial value of ϕ and the summation is taken over all edges of the

membrane elements. Details of the derivation of the bending forces can be found in Refs. [38, 77].

As described in Chapter 2, some studies have neglected the membrane bending resistance. It should be noted, however, that despite the relatively small value of the bending modulus ($\sim 2 \times 10^{-19}$ Nm), a bending resistance is necessary to prevent membrane buckling, especially when large local curvatures are formed.

3.3.3 Membrane Surface and Volume Energies

To enhance the conservation in total volume and membrane area in numerical simulations, the following penalty energy terms can also be incorporated [38]:

$$\begin{aligned} W_A &= \frac{E_A}{2} \frac{(A - A_0)^2}{A_0} \quad , \\ W_V &= \frac{E_V}{2} \frac{(V - V_0)^2}{V_0} \quad . \end{aligned} \quad (3.20)$$

Here, E_A and E_V are the penalty moduli for changes in volume V and total area A , and V_0 and A_0 are the initial volume and total area of an RBC model, respectively. In numerical simulations, small values of the penalty moduli for example, $E_A = 0.5 \text{ Jm}^{-2}$ and $E_V = 7.23 \times 10^5 \text{ Jm}^{-3}$, are usually adopted to control the area and volume deviations below 1% without causing numerical instabilities [38].

3.3.4 Membrane Viscosity

The viscous stress τ^v in membranes is typically decomposed into two parts: the shear viscous stress τ_s^v induced by the shear (deviatoric) part of the strain rate tensor \mathbf{D} , and the dilatational viscous stress τ_d^v from the dilatational (hydrostatic) part of \mathbf{D} [54, 83, 84, 53, 85, 86]:

$$\tau^v = \tau_s^v + \tau_d^v = \mu_s [2\mathbf{D} - \text{tr}(\mathbf{D})\mathbf{I}] + \mu_d \text{tr}(\mathbf{D})\mathbf{I} \quad , \quad (3.21)$$

where μ_s and μ_d are the shear and dilatational membrane viscosities, respectively. The matrix \mathbf{D} is the strain rate tensor of the membrane and \mathbf{I} is the 2×2 unit matrix. The strain rate tensor \mathbf{D} can be computed from the strain tensor \mathbf{E} using a backward finite difference approximation; whereas another approach is applying the membrane velocity

gradient [83, 84, 85, 86]

$$\mathbf{D} = \frac{1}{2} \left[\nabla_m \mathbf{u}_m + (\nabla_m \mathbf{u}_m)^T \right] . \quad (3.22)$$

Here, ∇_m indicates the gradient operator and \mathbf{u}_m denotes the membrane velocity, both in the local membrane plane.

As mentioned previously, the total nodal force at each Lagrangian membrane node is needed in the IBM force distribution step. The calculations for nodal forces from the energy terms W_s , W_b , W_A , and W_V are well-documented in the literature [38, 70]. In the following, the calculation of the membrane viscous stresses is described following Ref. [56].

3.4 Finite-Difference Method for Membrane Viscosity in IBM Simulations

To describe the calculation method for the viscous stress in membrane, we consider the Kelvin-Voigt viscoelastic model, as shown in Fig. 3.4a. The spring element k represents the elasticity of the membrane and the viscous part is displayed as the dashpot element μ . Since the spring and the dashpot elements are joined in parallel, they sustain the same amount of deformation and strain.

To mitigate the numerical noise in the calculated viscous stress, an artificial spring element k' is added in series to the dashpot μ (Fig. 3.4b). Combination of the dashpot μ and the new spring k' represents a Maxwell viscoelastic element. In this way, the original Kelvin-Voigt model is transferred into the so-called standard-linear-solid model [87]. Impact of the stiffness of k' on the system vanishes when its stiffness is set adequately large [56]. Nonetheless, including k' in the system precludes an explicit expression of the Maxwell element's stress for a given strain history $\epsilon(t)$, and a numerical scheme is required. Here, we adopt the finite difference method recently developed by Li and Zhang [56] to calculate the viscous stress in the Maxwell element.

The strain of the Maxwell element is the sum of those for the dashpot μ and artificial spring k' and their internal stress are equal to each other since μ and k' are connected in

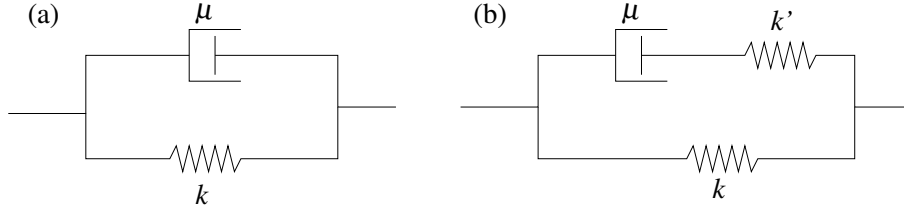


FIGURE 3.4: Schematic views of (a) the Kelvin-Voigt model for modeling the membrane viscoelasticity (spring k represents the membrane elasticity and the membrane viscosity is indicated by dashpot μ) and (b) the standard linear solid model with an artificial spring k' .

series:

$$\sigma_M = \sigma_\mu = \sigma_{k'} \quad ; \quad (3.23)$$

$$\epsilon_M = \epsilon_\mu + \epsilon_{k'} \quad . \quad (3.24)$$

All of these strain terms are defined according to the same undeformed length of the Maxwell element. The stresses and strains are presented by, respectively, σ and ϵ , and subscripts are used to indicate the corresponding components for these properties: M for the Maxwell element, μ for the dashpot μ , and k' for the spring k' . The stresses and strains in the dashpot μ and spring k' are related via the coefficients for the viscous dashpot and the linear spring as

$$\sigma_\mu = \mu \dot{\epsilon}_\mu \quad ; \quad \sigma_{k'} = k' \epsilon_{k'} \quad . \quad (3.25)$$

In this equation, μ and k' have also been used to denote, respectively, the viscosity of the dashpot μ and the Hookean coefficient of the spring k' . Taking the time rate of Eq. (3.24) and using relations in Eqs. (3.23) and (3.25) yield

$$\dot{\epsilon}_M = \frac{\sigma_M}{\mu} + \frac{\dot{\sigma}_M}{k'} \quad . \quad (3.26)$$

This represents the dynamic constitutive relation for the Maxwell element. The stress term $\sigma_M(t)$ can then be obtained by applying the central finite difference approximation for the time rate terms and considering the stress at $t - \Delta t/2$ as the average of those at $t - \Delta t$ and t [56, 57]:

$$\sigma_M(t) \approx \frac{(2\mu - k'\Delta t)\sigma_M(t - \Delta t) + 2\mu k'[\epsilon_M(t) - \epsilon_M(t - \Delta t)]}{2\mu + k'\Delta t} \quad . \quad (3.27)$$

With the initial condition specified [typically the system dynamics starts from a stress-free state $\epsilon_M(0) = 0$ and $\tau_M(0) = 0$] and using an appropriate time interval Δt , the above equation can be employed to calculate the stress in the Maxwell element $\sigma_M(t)$ from the strain function $\epsilon_M(t)$. Please note that we used the one-dimensional representation of membrane viscoelasticity in Fig. 3.4 for clarity. For the 2D membrane model adopted here, the strain and stress terms need to be replaced by 2×2 tensors for membrane elements. See details for substitution in Ref. [56].

3.5 The Computational Procedure

The detailed algorithm and steps for applying the finite difference method to IBM simulations are described here with a focus on implementation of the membrane viscosity. An overview of the computational procedure is depicted in Fig. 3.5. Generally, to initialize the simulations, a computational domain with specific size in lattice units is considered (a 3D simulation box in this thesis) and the RBC will be placed at a specific location inside the domain. To start the calculations at time $t = 0$, the initial values for the distribution functions f_i at all fluid nodes and velocity directions need to be prescribed. Typically, the distribution functions are initialized at equilibrium using Eq. (3.5)

$$f_i(\mathbf{x}, t = 0) = f_i^{eq}(\rho_0, \mathbf{u}_0) \quad , \quad (3.28)$$

where ρ_0 is the initial density and \mathbf{u}_0 is the initial flow field. As in typical LBM simulations [75] we set $\rho_0 = 1$ and $\mathbf{u}_0 = (0, 0, 0)$ for simplicity. Therefore, the initial membrane node positions and state of the fluid are determined. Then, the membrane nodal forces are calculated using the membrane mechanics (Section 3.3). Subsequently, the nodal forces are distributed to the neighboring fluid nodes as body forces using the force distribution step in IBM (Section 3.2). The flow field can then be solved via LBM (Section 3.1). With the new state of the fluid being known, the membrane node velocities can be obtained by applying the velocity interpolation step of IBM (Section 3.2). Using the obtained node velocities, membrane node positions can be updated via the Euler scheme. In this way, the computer program performs a series of computations for time step δt ,

and the simulation time proceeds from t_{i-1} to $t_i = t_{i-1} + \delta t$. This process continues until desired results are obtained.

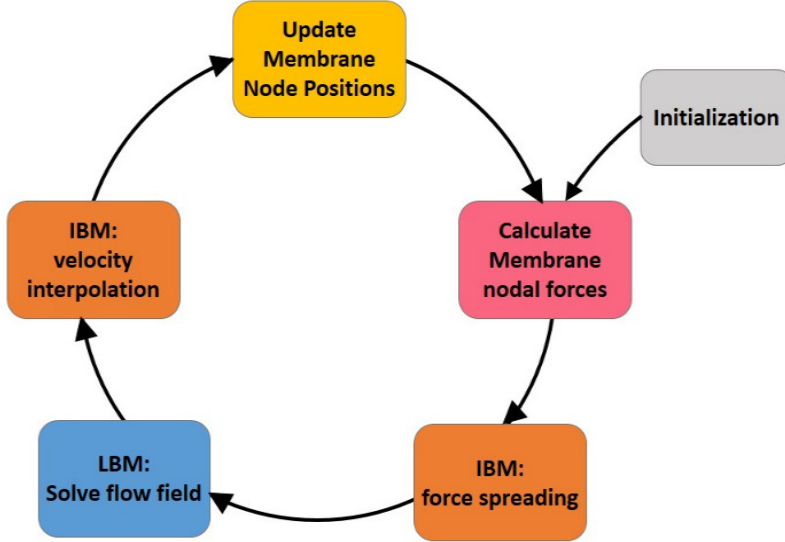


FIGURE 3.5: Schematic view of the simulation algorithm. It proceeds from the initialization step.

The integrated algorithm is described in more detailed steps as follows. With the properties at the end of the $(i - 1)$ -th cycle being known (from the initialization or the previous calculation cycle):

1. Calculate the membrane node velocity $\mathbf{u}_m(t_{i-1})$ using Eq. (3.10).
2. Calculate the new membrane node position $\mathbf{x}_m(t_i)$ via the Euler scheme:

$$\mathbf{x}_m(t_i) = \mathbf{x}_m(t_{i-1}) + \mathbf{u}_m(t_{i-1})\delta t \quad . \quad (3.29)$$

3. Calculate the local membrane strain tensor $\mathbf{E}(t_i) = \begin{bmatrix} E_{11} & E_{12} \\ E_{21} & E_{22} \end{bmatrix}$ by Eq. (3.18) for each membrane element. Note that the strain tensor \mathbf{E} is symmetric and $E_{12} = E_{21}$.
4. Calculate the in-plane elastic membrane stress $\boldsymbol{\tau}^e(t_i) = \begin{bmatrix} \tau_{11}^e & \tau_{12}^e \\ \tau_{21}^e & \tau_{22}^e \end{bmatrix}$ from the constitutive relationship of the membrane material (Eq. 3.14) via Eqs. (3.15-3.17). Details of the implementation of these equations can be found in Refs. [79, 38].

5. Perform the following calculations for the membrane viscous stresses,

(a) Calculate the shear (E_{11}^s and E_{12}^s) and dilatational (E_{11}^d) strain tensor elements:

$$E_{11}^s = \frac{E_{11} - E_{22}}{2} \quad , \quad E_{12}^s = E_{12} \quad , \quad E_{11}^d = \frac{E_{11} + E_{22}}{2} \quad . \quad (3.30)$$

All other elements are directly related to these three ($E_{21}^s = E_{12}^s$, $E_{22}^s = -E_{11}^s$ and $E_{22}^d = E_{11}^d$) or simply zeros ($E_{12}^d = E_{21}^d = 0$).

(b) Calculate the three independent viscous stress elements from the corresponding strain elements above using the following equations, which are direct modifications of Eq. (3.27):

$$\tau_{11}^{v,s}(t_i) \approx \frac{(4\mu_s - k'_s \Delta t) \tau_{11}^{\mu,s}(t_{i-N}) + 4\mu_s k'_s [E_{11}^s(t_i) - E_{11}^s(t_{i-N})]}{4\mu_s + k'_s \Delta t} \quad , \quad (3.31)$$

$$\tau_{12}^{v,s}(t_i) \approx \frac{(4\mu_s - k'_s \Delta t) \tau_{12}^{\mu,s}(t_{i-N}) + 4\mu_s k'_s [E_{12}^s(t_i) - E_{12}^s(t_{i-N})]}{4\mu_s + k'_s \Delta t} \quad , \quad (3.32)$$

$$\tau_{11}^{v,d}(t_i) \approx \frac{(4\mu_d - k'_d \Delta t) \tau_{11}^{\mu,d}(t_{i-N}) + 4\mu_d k'_d [E_{11}^d(t_i) - E_{11}^d(t_{i-N})]}{4\mu_d + k'_d \Delta t} \quad , \quad (3.33)$$

and other viscous stress elements are

$$\tau_{21}^{v,s} = \tau_{12}^{v,s} \quad , \quad \tau_{22}^{v,s} = -\tau_{11}^{v,s} \quad , \quad \tau_{22}^{v,d} = \tau_{11}^{v,d} \quad , \quad \tau_{12}^{v,d} = \tau_{21}^{v,d} = 0 \quad . \quad (3.34)$$

6. Add the elastic and viscous stresses together for each membrane element:

7. Convert the total local membrane stress $\boldsymbol{\tau}$ to nodal forces on the three vertices of each element. See details in Refs. [54, 79].

8. Calculate the bending, area, and volume forces. See details in Ref. [38].

9. Add all the nodal forces obtained in Steps 7 and 8 together.

10. Distribute the nodal forces to neighboring fluid nodes according to Eq. (3.8).

11. Calculate the flow field $\mathbf{u}(t_i)$ using the LBM.

12. Return to Step 1 for the next cycle.

Chapter 4

Lateral Migration of Viscoelastic Capsules in Tube Flow

This chapter presents the simulation results and discussions for the migration processes of viscoelastic capsules in tube flow. Appropriate validation tests are also performed to validate the methods and programs.

4.1 Model and Program Validations

Before performing simulations for lateral migration of capsules in tube flow, we validate the models, algorithms, and computer programs by conducting two benchmark test simulations: the tank-treading dynamics of a spherical elastic capsule in linear shear flow, and the lateral migration of a neutrally-buoyant rigid sphere in tube flow. These validations confirm that the simulation results to be presented in the next section are reliable and accurate.

4.1.1 Tank-Treading Dynamics of Elastic Capsule in Linear Shear Flow

My programs used in this thesis are developed based on the previous codes in our group, which have been validated for different systems [9, 56, 57]. For example, the effects of Lagrangian mesh resolution for membrane have been investigated previously [56]. Accuracy and stability of the finite difference method for membrane viscosity have also

been thoroughly examined for different systems including spherical shells under twisting deformation and capsules and droplets under linear shear flow [56, 57]. Furthermore, detailed comparisons have been made for the tank-treading behaviors of an originally spherical capsule in shear flow in previous publications [9]. However, the interior-exterior fluid viscosity contrast had been maintained at unity, and the tank-treading rotation frequency had not been accessed. To clear these concerns, we first simulate the dynamics of an elastic capsule in shear flow and compare the results with those in the literature. Here, I do not consider the membrane viscosity since the membrane viscous stress calculation has been verified in previous publication [56] and later confirmed by other independent researchers [58].

In this set of simulations, the capsule, which is initially spherical with diameter of $a = 19.1$, is placed at the center of a cubic domain with size of $120 \times 120 \times 120$, all in the lattice unit δx . The capsule membrane is represented by 5120 triangular elements. Such Eulerian and Lagrangian mesh resolutions have been confirmed to be sufficient for these simulations [56, 9, 77]. The Skalak (SK) constitutive law with $C = 1$ in Eq. (3.14) [88, 89, 81] is utilized for the membrane stress calculation. To produce a shear flow around the capsule, the top and bottom domain boundaries are treated as solid walls moving at velocity U_0 , however, in opposite horizontal directions (Fig. 4.1a). This setup creates a linear shear flow with shear rate of $\dot{\gamma} = 2U_0/H$, where H is the height of the simulation box. Periodic boundary conditions are imposed on the other sides of the computational domain. The viscosity ratio is defined as $\lambda = \mu_i/\mu_o$, where μ_i and μ_o are viscosities of the interior and exterior fluids of the capsule, respectively. Another important parameter for this system is the capillary number $Ca = \mu_o \dot{\gamma} a / 2E_s$, which can be interpreted as the relative strength of the fluid viscous effect due to the external flow compared to the membrane elasticity.

After the shear flow is imposed, the capsule gradually elongates to reach a steady shape and aligns itself with an angle from the flow direction. In the meantime, the membrane rotates around the interior fluid, which performs an eddy-like rotation about the capsule center. This is called the tank-treading rotation. Several parameters have been employed

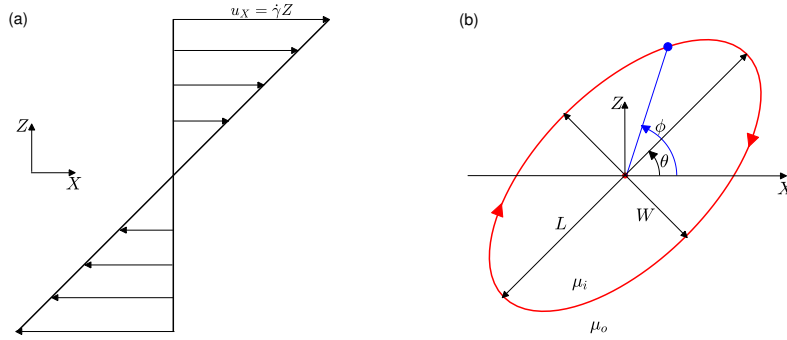


FIGURE 4.1: Schematic illustrations of (a) the imposed linear shear flow and (b) the deformed capsule shape in the shear plane with the largest axis L , smallest axis W , and the inclination angle θ . Also shown in (b) are the definitions for the rotation angle ϕ for a membrane marker (blue circle), the membrane rotation (red arrows), and the interior and exterior fluid viscosities μ_i and μ_o , respectively.

to characterize the capsule dynamics, including the Taylor deformation index D , the inclination angle θ (Fig. 4.1b), and the tank-treading period TTP . For moderate shear rates, the steady capsule shape is similar to an ellipsoid with the largest axis L and the shortest axis W in the shear plane. The deformation index is defined as

$$D = \frac{L - W}{L + W} . \quad (4.1)$$

The inclination angle θ is taken as the angle between the flow direction and the major axis, as shown in Fig. 4.1b. Following Ref. [37], the deformed capsule is approximated by an equivalent ellipsoid based on the inertia tensor, and the deformation index D and inclination angle θ are obtained from the axes and orientation angle of the equivalent ellipsoid. The tank-treading period TTP can be obtained from the trajectory of a membrane marker point in the middle shear plane. Another approach is to integrate the travel time of the membrane marker [37, 89]. These two approaches yield very close values for TTP [70, 46], and thus the results obtained from the first method are presented. Different values for the viscosity contrast λ and the capillary number Ca are considered.

The results are collected in Table 4.1 in comparison to data from several previous studies: Lac et al. [89] (Lac), Li and Sarkar [81] (LS), Foessel et al. [88] (Foessel), Ramanujan and Pozrikidis [37] (RP), and Doddi and Bagchi [70] (DB). It should be mentioned that RP and DB used the neo-Hookean (NH) constitutive relationship for the capsule membrane,

TABLE 4.1: Comparison of steady state results for a spherical capsule in shear flow with different viscosity ratio λ and capillary number Ca to those reported by Lac et al. [89] (Lac), Li and Sarkar [81] (LS), Foessel et al. [88] (Foessel), Ramanujan and Pozrikidis [37] (RP), and Doddi and Bagchi [70] (DB) Abbreviations SK and NH denote, respectively, the Skalak and neo-Hookean membrane constitutive relationships used for the membrane material in these studies.

(a) Deformation index D :																				
$\lambda = 0.2$							$\lambda = 1$							$\lambda = 5$						
Ca	Present (SK)	Foessel (SK)	LS (NH)	LS (NH)	RP (NH)	Present (SK)	Lac (SK)	LS (SK)	Foessel (SK)	LS (NH)	RP (NH)	DB (NH)	Present (SK)	Foessel (SK)	LS (NH)	RP (NH)	LS (NH)	RP (NH)		
0.0375	0.148	0.147	0.151	0.146	0.143	0.145	0.143	0.146	0.143	0.153	0.155	0.162	0.128	0.123	0.138	0.138	-	-		
0.075	0.244	0.237	0.260	0.230	0.260	0.239	0.235	0.230	0.229	0.255	0.262	0.278	0.191	0.179	0.210	0.210	0.183	0.183		
0.15	0.349	0.343	0.380	0.325	0.398	0.334	0.335	0.325	0.335	0.370	0.382	0.392	0.252	0.240	0.286	0.269	0.269	0.269		
0.3	0.448	0.445	0.519	0.429	0.541	0.432	0.432	0.429	0.429	0.490	0.501	0.496	0.299	0.285	0.356	0.289	0.289	0.289		

(b) Inclination angle θ (in π):																				
$\lambda = 0.2$							$\lambda = 1$							$\lambda = 5$						
Ca	Present (SK)	Foessel (SK)	LS (NH)	LS (SK)	RP (NH)	Present (SK)	Lac (SK)	LS (SK)	Foessel (SK)	LS (NH)	RP (NH)	DB (NH)	Present (SK)	Foessel (SK)	LS (NH)	RP (NH)	LS (NH)	RP (NH)		
0.0375	0.204	0.211	0.220	0.207	-	0.205	0.206	0.207	0.200	0.204	0.203	0.201	0.152	0.149	0.159	-	-	-		
0.075	0.197	0.203	0.199	0.184	0.195	0.179	0.182	0.184	0.181	0.178	0.170	0.168	0.115	0.114	0.119	0.105	0.105	0.105		
0.15	0.176	0.184	0.173	0.162	0.170	0.154	0.155	0.162	0.154	0.151	0.142	0.136	0.081	0.078	0.086	0.059	0.059	0.059		
0.3	0.153	0.161	0.141	0.140	0.139	0.130	0.132	0.140	0.132	0.123	0.114	0.107	0.057	0.054	0.059	0.045	0.045	0.045		

(c) Tank-treading period TTP (in γ^{-1}):																				
$\lambda = 0.2$							$\lambda = 1$							$\lambda = 5$						
Ca	Present (SK)	LS (NH)	RP (NH)	LS (SK)	LS (SK)	Present (SK)	Lac (SK)	LS (SK)	LS (SK)	LS (NH)	RP (NH)	DB (NH)	Present (SK)	LS (NH)	RP (NH)	LS (NH)	RP (NH)			
0.0375	13.373	13.032	-	13.120	13.196	13.426	13.120	13.196	13.196	13.495	13.357	13.4	14.609	14.502	-	-	-			
0.075	13.562	13.526	13.628	14.071	13.996	14.581	14.071	13.996	14.496	14.496	14.579	15.0	16.698	16.710	15.481	15.481	15.481			
0.15	14.343	14.903	15.284	16.168	15.511	16.319	16.168	15.511	17.016	16.609	16.609	17.8	19.518	20.008	17.919	17.919	17.919			
0.3	15.472	17.219	18.149	18.013	18.583	18.709	18.013	18.583	21.605	19.699	19.699	21.3	22.331	-	18.985	18.985	18.985			

while the Skalak (SK) strain energy function Eq. (3.14), which was developed for the particular features of RBC membrane [8], was adopted in the present, Lac, and Foessel calculations. LS considered both SK and NH membranes in their simulations; however, their SK calculations were only for $\lambda = 1$ while different λ values were considered for the NH membranes. In addition, although the capsule dynamics of SK and NH membranes are similar at small deformation, they exhibit, respectively, strain-hardening and strain-softening behaviors at large deformations [81]. Quantitative comparisons with the results from previous studies are provided in Table 4.1 for three different viscosity ratios of $\lambda = 0.2, 1, \text{ and } 5$ and a range of Ca from 0.0375 (slightly deformed) to 0.3 (largely deformed). It can be seen from Table 4.1 that there is an excellent agreement between our results and those with SK membranes, for all the capillary numbers and viscosity ratios considered and all the characteristic parameters examined (deformation index D , inclination angle θ , and tank-treading period TTP). Even for the results with NH membranes (LS, RP, and DB), the agreement is fairly good at small capillary numbers. The relatively large difference in the deformation, orientation, and TTP for SK and NH membranes at large capillary numbers is indeed expected considering their different responding behaviors to large strains, as mentioned above.

In addition to the numerical comparison, we notice several general correlations between the system parameters Ca and λ and the tank-treading behaviors, characterized by D , θ , and TTP , in Table 4.1. These correlations have been discussed in previous studies [89, 81, 46]; however, they are helpful for our migration analysis in the next sections and we have a brief description here. For the capsules with elastic membranes considered here, the deformation index D and inclination angle θ both decrease as the viscosity ratio λ increases, but they respond to the capillary number Ca oppositely: the deformation D increases with Ca since a higher Ca means a more flexible membrane, while the inclination angle θ decreases for higher Ca since a more flexible capsule can align closer to the shear direction. It is also noted that the changes in D and θ are much smaller when λ reduces from 1 to 0.2, compared to those when it increases from 1 to 5. As for the tank-treading period TTP , it increases with both λ and Ca , and its responses to the $0.2 \rightarrow 1$ and $1 \rightarrow 5$ changes in λ are not dramatically different.

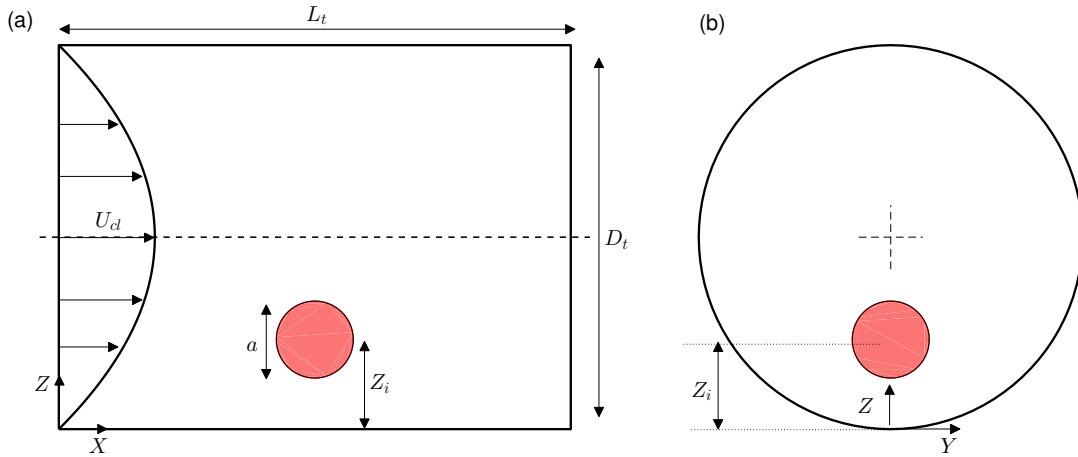


FIGURE 4.2: Schematic diagrams of the simulation setup for particle and capsule migration processes: (a) the side view along the Y direction, and (b) the axial view along the flow direction. The tube is represented by black lines and the particle/capsule is shown as red circles. See the text for more detailed information on the system parameters.

4.1.2 Lateral Migration of a Neutrally-Buoyant Rigid Sphere

The focus of this chapter is the migration process of a capsule in tube flow. Few previous studies utilized the planar Poiseuille flow between flat surfaces [70, 69] or the unbounded tube flow with the wall effect neglected [68]. Also these studies were performed with different systems and their results are not comparable directly. To have a more reliable evaluation of the performance of our program in simulating the migration process, we consider the lateral migration of a neutrally-buoyant rigid sphere in a tube flow. Although not presented here, we have simulated the undisturbed (without sphere) Poiseuille flow in a tube of radius $R = 150 \delta x$ and obtained a relative error of about 0.9% for the maximum velocity in comparison to the theoretical result. It is well-established that, when a rigid spherical particle is released in a tube flow, the particle will gradually approach an equilibrium radial position across the flow. This phenomenon is called the Segre-Silberberg effect [90, 91], and the equilibrium position depends on the relative size of the particle to the tube radius and the Reynolds number [92, 93, 94]. Here, following previous studies [92, 93, 95], we consider the system with particle-tube diameter ratio $a/D_t = 0.15$ and the Reynolds number $Re = \rho U_{cl} D_t / \mu_o = 100$. In these expressions, a and D_t are, respectively, the diameters for the particle and the tube, and U_{cl} is the nominal centerline velocity of the tube flow when the particle is not present (see Fig. 4.2

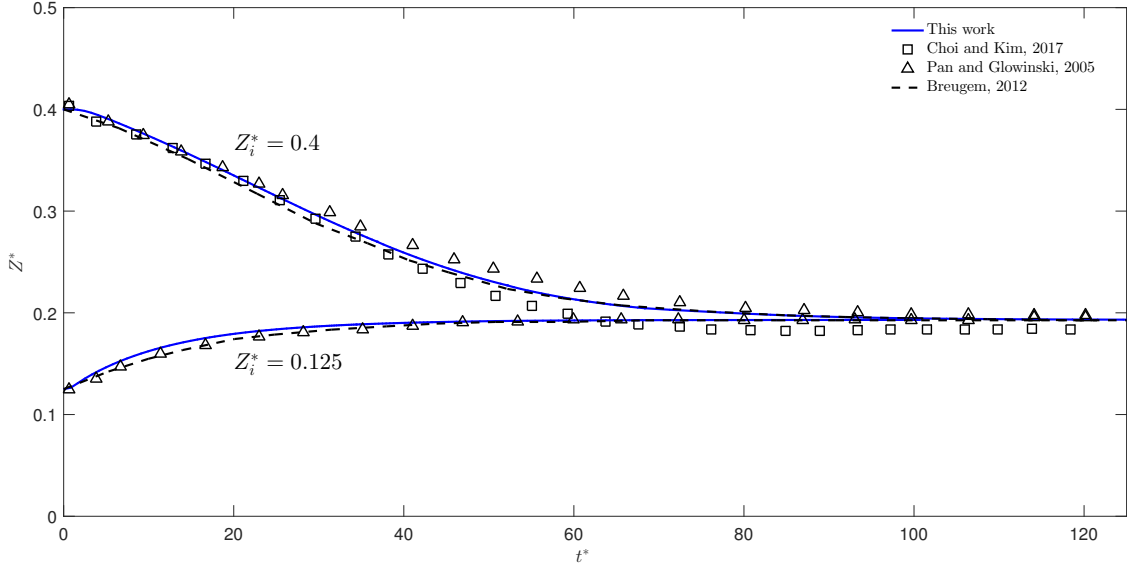


FIGURE 4.3: Lateral positions of the particle centroid as it migrates toward its equilibrium position in the tube flow. Results from previous publications are also shown for comparison.

for the system setup). In our LBM simulation, we use $D_t = 300 \delta x$ and a body force of $f = 16Re\mu_0^2/\rho D_t^3$ to generate the flow. The length of the tube segment is $L_t = 2D_t$, however, with the periodic boundary implemented at the tube ends. At the beginning of the simulation, the particle is located at a distance Z_i from the wall (Fig. 4.2), and it is released to move with the ambient flow freely as the simulation starts. Two initial positions are tested here: $Z_i/D_t = 0.4$ and $Z_i/D_t = 0.125$. Typically, the lateral position in an axisymmetric tube is denoted by the radial distance to the tube centerline; however, for the convenience in describing the migration process, we use the distance Z from the tube wall for the particle and capsule lateral position: the migration proceeds in the same direction as Z and the migration velocity is positive (except the case with $Z_i/D_t = 0.4$ in the rigid particle validation, where the particle migrates outwards to the equilibrium position). To model a rigid particle, we increase the elastic modulus E_s and the interior fluid viscosity to reduce the membrane flexibility. The capillary number based on the centerline velocity U_{cl} [70] is $Ca = \mu_0 U_{cl}/E_s = 10$, the area dilation coefficient $C = 10$, and the viscosity ratio $\lambda = 20$. With this set of capsule parameters, the capsule deformation during the migration process is negligible and thus the results can be compared to those for rigid particles. Similar treatments have been utilized in previous studies of particle dynamics [96, 97].

The particle migration processes from the present simulations are compared to those reported in previous publications [92, 93, 95] in Fig. 4.3. The migration process is slow and it takes up to about $t^* = U_{cl}t/D_t = 100$ for the particle to reach the equilibrium position, which is almost identical for the two different initial positions. When compared to those from previous studies, a good agreement is noticed in the migration processes for both cases. More specifically, the equilibrium radial position from our calculations is $0.195D_t$, which is very close to those reported in previous studies: $0.184D_t$ in Choi and Kim [93], $0.198D_t$ in Pan and Glowinski [95], and $0.193D_t$ in Breugem [92].

4.2 Simulation Setup for Capsule Migration in Tube Flow

With the good agreement obtained in the above validation tests, next the lateral migration of a viscoelastic capsule in the tube flow is simulated. Similar to the setup used in the rigid particle migration validation in Sect. 4.1.2, the circular tube of diameter D_t and length $L_t = 2D_t$ is placed along the X -axis in the XYZ coordinate system (Fig. 4.2). When solving the fluid flow, the no-slip boundary condition is applied on the tube wall surface and the periodic boundary condition is incorporated across the tube inlet and outlet. Again a body force is adopted to generate the fluid flow along the tube. As reported in Ref. [70] and also confirmed in my numerical tests, further increasing the tube length L_t has no apparent influence on the simulation results. The fluids inside and outside of the capsule are both Newtonian with viscosity of, respectively, μ_i and μ_o ; however, they have same density ρ . The Reynolds number is defined as $Re = \rho a U_{cl} / \mu_o$ [70]. Here, we use $Re = 0.02$, and therefore, the inertia effects can be neglected [77]. The undisturbed Poiseuille flow (i.e., if no capsule presents) inside the tube is expressed as

$$u_x = \left(1 - \frac{r^2}{R_t^2}\right) U_{cl} \quad , \quad (4.2)$$

where r is radial position measured from the tube centerline and $R_t = D_t/2$ is the tube radius. At time $t = 0$, the initially spherical capsule with diameter of $a = D_t/4$ is placed at $X_i = L_t/2$, $Y_i = 0$, and $Z_i = 0.175D_t$ measured from the tube wall (Fig. 4.2). The capsule membrane follows the SK constitutive law Eq. (3.14) with $C = 1$ for simplicity,

and only the shear membrane viscosity μ_s is considered for the strong area conservation in typical biological capsules. The membrane shear viscosity is represented by the shear Boussinesq number $Bq_s = \mu_s / \mu_o a$ [56, 83, 58]. For the artificial spring element in Fig. 3.4b, the non-dimensional stiffness coefficient $\kappa = D_t k' / U_{cl} \mu_s$ is set at 30 in our simulations. Here, $D_t = 120$ for the Eulerian grid, and the capsule membrane is discretized into 5120 triangular elements. In our simulations, the constant-volume enhancement technique [9, 77] is not necessary, and the maximum variation in capsule volume is less than 0.2%.

In the result presentation and analysis, the lateral and axial velocities of the capsule are normalized by U_{cl} , and time is presented in dimensionless form as $t^* = t U_{cl} / D_t$. Lateral position of the capsule centroid in the Z and X directions are also normalized as $Z^* = Z / D_t$, and $X^* = X / L_t$, respectively. The nondimensional rotation period of the capsule is denoted by T^* , also normalized in D_t / U_{cl} . The capillary number is defined as $Ca = \mu_o U_{cl} / E_s$, and viscosity ratio is $\lambda = \mu_i / \mu_o$ [70]. Moreover, similar to the definition of capillary number for capsule in linear shear flow, we introduce a local capillary number based on the local shear rate around the capsule as

$$Ca^* = \frac{\mu_o a \dot{\gamma}_p}{2E_s} , \quad (4.3)$$

where $\dot{\gamma}_p$ is the local shear rate of the undisturbed Poiseuille flow Eq. (4.2) at the capsule centroid. Please note that the general capillary number Ca is a system parameter and remains constant during a migration process, while the local capillary number Ca^* varies with the capsule lateral position.

4.3 Effect of Viscosity Ratio on Capsule Migration

At first, the effect of viscosity ratio λ on the capsule migration dynamics is considered. The capillary number is fixed at $Ca = 0.2$ and the membrane viscosity is neglected (i.e., $Bq_s = 0$), while a series of λ values, $\lambda=0.2, 1, 3, 5$, and 10 , are considered. Fig. 4.4 depicts snapshots of capsule shapes at several lateral locations: $Z^* = 0.175$ (initial position), $0.2, 0.25, 0.3, 0.35$, and 0.4 , with the corresponding time elapsed for the capsule to reach that lateral position labeled beneath. Here, only the capsule shapes for $\lambda=1, 5$, and 10 are

presented since the capsule shapes for $\lambda=0.2$ are very similar to those with $\lambda=1$, and the shapes from $\lambda = 3$ lie between those from $\lambda = 1$ and 5 shown in Fig. 4.4.

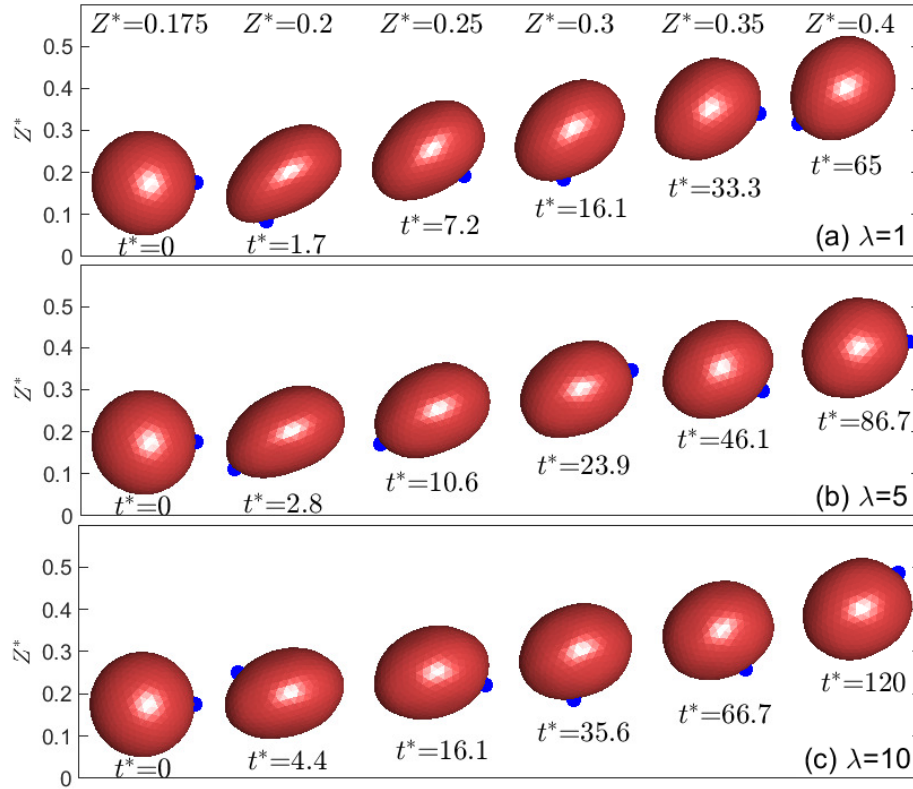


FIGURE 4.4: Capsule shapes during migration in the tube flow for different viscosity ratios: (a) $\lambda = 1$, (b) $\lambda = 5$, and (c) $\lambda = 10$. These shapes are taken at the same lateral locations Z^* (labeled on top of a), and the corresponding time t^* at each Z^* is shown below the individual shape. The blue point represents a membrane marker point to demonstrate the capsule rotation during the migration.

At $Z^* = 0.2$, the capsule has just migrated a lateral distance of $0.025D_t$ and this process finishes within $t^* < 5$. Although over such a short period and distance, the capsule quickly elongates into an ellipsoid-like shape and aligns itself at an angle with the direction of the flow, similar to capsules in simple shear flows. After the dramatic deformation in this initial phase of migration, the capsule deformation gradually reduces as it migrates toward the tube centerline. Several factors might be associated with this short but fast deformation process, including the strong influence from the tube wall, the relatively large shear gradient of the flow, and the initial unstressed membrane state. The effects of

boundary surface and shear gradient on capsule or particle migration have been extensively investigated [90, 93, 69, 68]; however, this phenomenon can be mainly attributed to the initial unstressed spherical shape. At $t = 0$ as the flow starts, the membrane is not deformed and thus there is no resistance force to the flow around the capsule; in another words, the membrane appears very weak in the flow. While the membrane responds immediately to the deformation, it may take some time for the fluid flow to react to the membrane force influence (i.e., momentum injection). As time proceeds, the flow and the membrane gradually *negotiate*; however, since the capsule is moving in the lateral direction and both the wall influence and the shear gradient are continuously changing, a balance (i.e, a steady state) cannot be established. I have tested other release locations, and similar transient periods are observed. For this reason, the later discussions and analyses will focus on the later part of the migration process.

In addition to the gradually reduced capsule deformation as it moves away from the tube wall, when comparing capsule shapes at a same lateral position from different viscosity ratios, it can be seen that the capsule deformation is less significant at higher viscosity ratios. This observation is consistent with the $D \sim \lambda$ relation in Table 4.1a for capsules in shear flow: The deformation index D reduces as the imposed shear rate decreases and/or the viscosity ratio increases. Meanwhile, looking at the time intervals between two consecutive shapes after $Z^* = 0.2$, one can see that the migration velocity is also slower for a capsule with a higher interior viscosity. During the migration process, similar to the tank-treading behavior of the capsule in linear shear flow, the membrane rotates around the interior fluid, as shown by the blue points in Fig. 4.4. It is also noticed in Fig. 4.4 that increasing λ slows down the migration process. For instance, to reach the lateral position $Z^* = 0.4$, the capsule with $\lambda = 10$ takes $t^* = 120$ long, almost two times of that for $\lambda = 1$ ($t^* = 65$). The slow migration velocity at higher λ is mainly due to the smaller deformation, as to be discussed in more details.

The streamlines for the case with $\lambda = 1$ are displayed in Fig. 4.5, where the capsule is at lateral location of $Z^* = 0.25$. The streamlines are calculated according to the stream function definition.

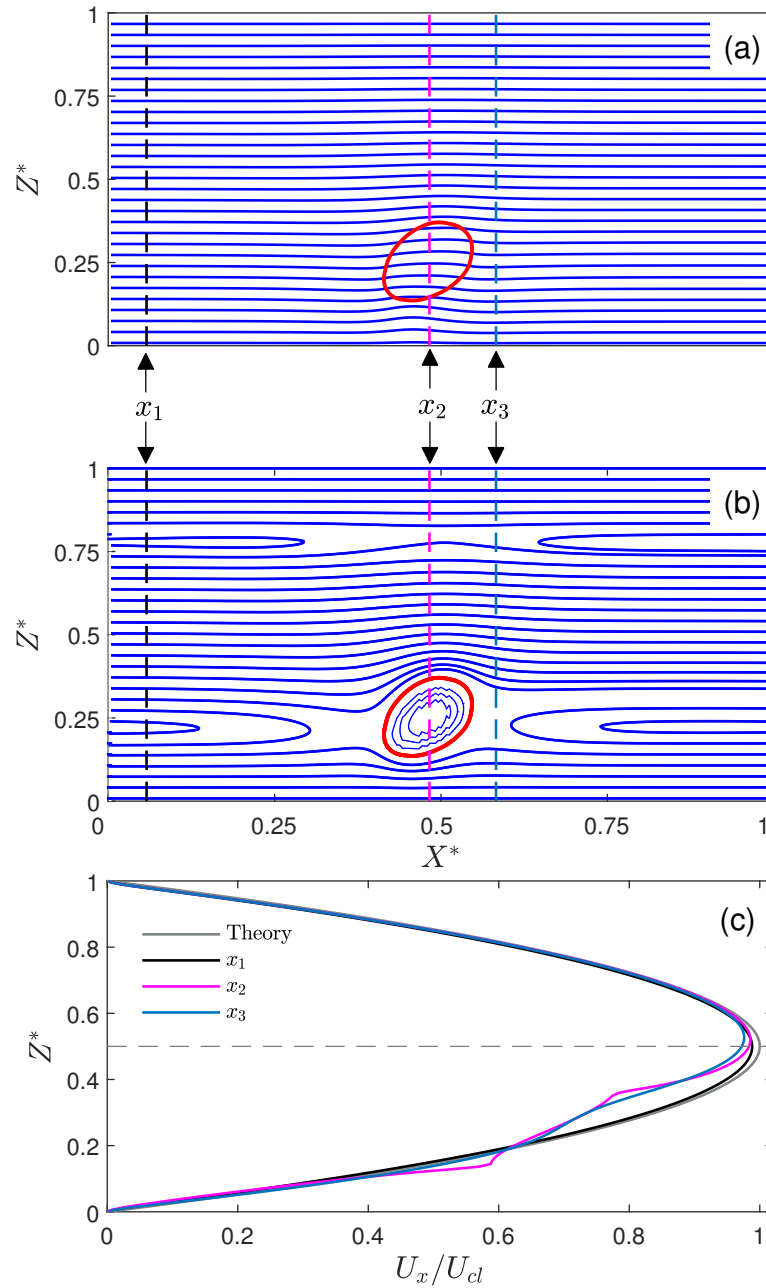


FIGURE 4.5: Streamlines for the flow around and inside the capsule in the $Y = 0$ plane in (a) the original reference frame and (b) a reference frame moving with the velocity of the capsule centroid. The capsule shape is shown in red color and the vertical dashed lines show three representative axial positions: far from the capsule x_1 , on the center of capsule x_2 , and close to the capsule x_3 . The velocity profiles at these three representative axial positions are depicted in (c) along with the theoretical Poiseuille velocity profile. Here, $\lambda = 1$ and the capsule is at lateral location $Z^* = 0.25$.

In Fig. 4.5a, the streamlines are plotted in the original reference frame. It can be seen that the streamlines are smooth and almost parallel. This is expected since the Reynolds

number is low and the migration velocity is small compared to the axial drifting velocity as will be presented in Fig. 4.7. Therefore, presenting the streamlines in a reference frame moving with the axial velocity of the capsule centroid provides clearer view of the flow pattern inside and around the capsule, as shown in Fig. 4.5b. The vertical dashed lines labeled as x_1 , x_2 , and x_3 indicate axial positions far from the capsule, at the capsule centroid, and close to the capsule, respectively. The velocity profiles U_x at these representative positions are illustrated in Fig. 4.5c along with the theoretical Poiseuille velocity profile. The relative error for the maximum velocity at position x_3 (far from the capsule) in comparison to the theoretical results is about 1%. In addition, the velocity profile at position x_2 (center of the capsule) does not indicate any slip velocity between the membrane and ambient flow.

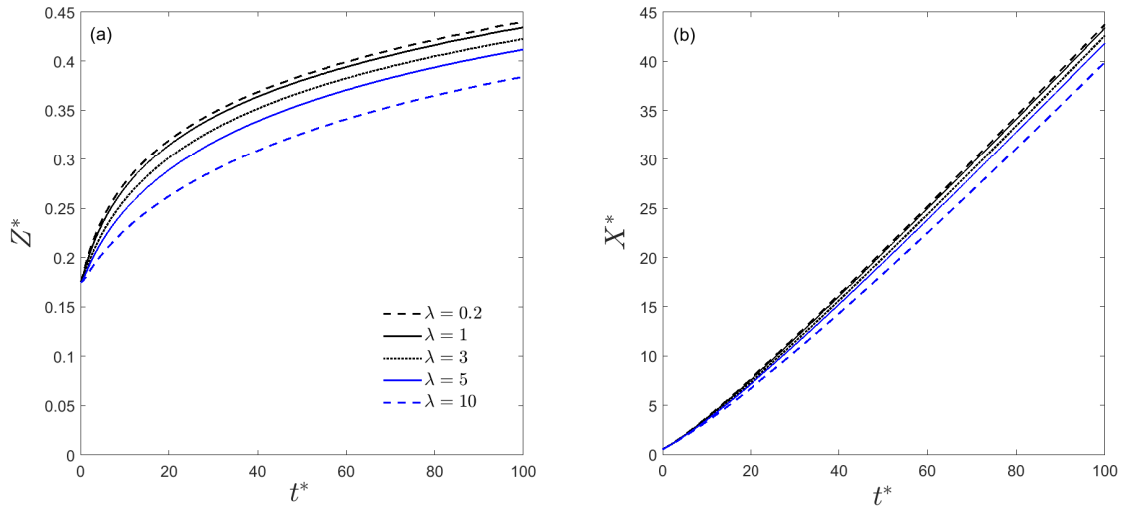


FIGURE 4.6: Temporal evolution of (a) the lateral position and (b) the axial location of the capsule with different λ values.

For a more complete picture of the migration process, we plot the temporal evolution of the lateral and axial locations of the capsule center in Fig. 4.6. The slower lateral migration velocity for a higher λ appears more apparent in Fig. 4.6a. The gradually flattened $Z^* \sim t^*$ curves also suggest that the migration velocity is decreasing as the capsule moves toward the tube centerline. On the other hand, λ exhibits much less profound influence on the axial motion of the capsule in Fig. 4.6b. The slightly slower axial motion at higher λ is mainly caused by the slower lateral migration: At the same time t^* , a capsule with a higher λ is closer to the wall and therefore the ambient flow is slower.

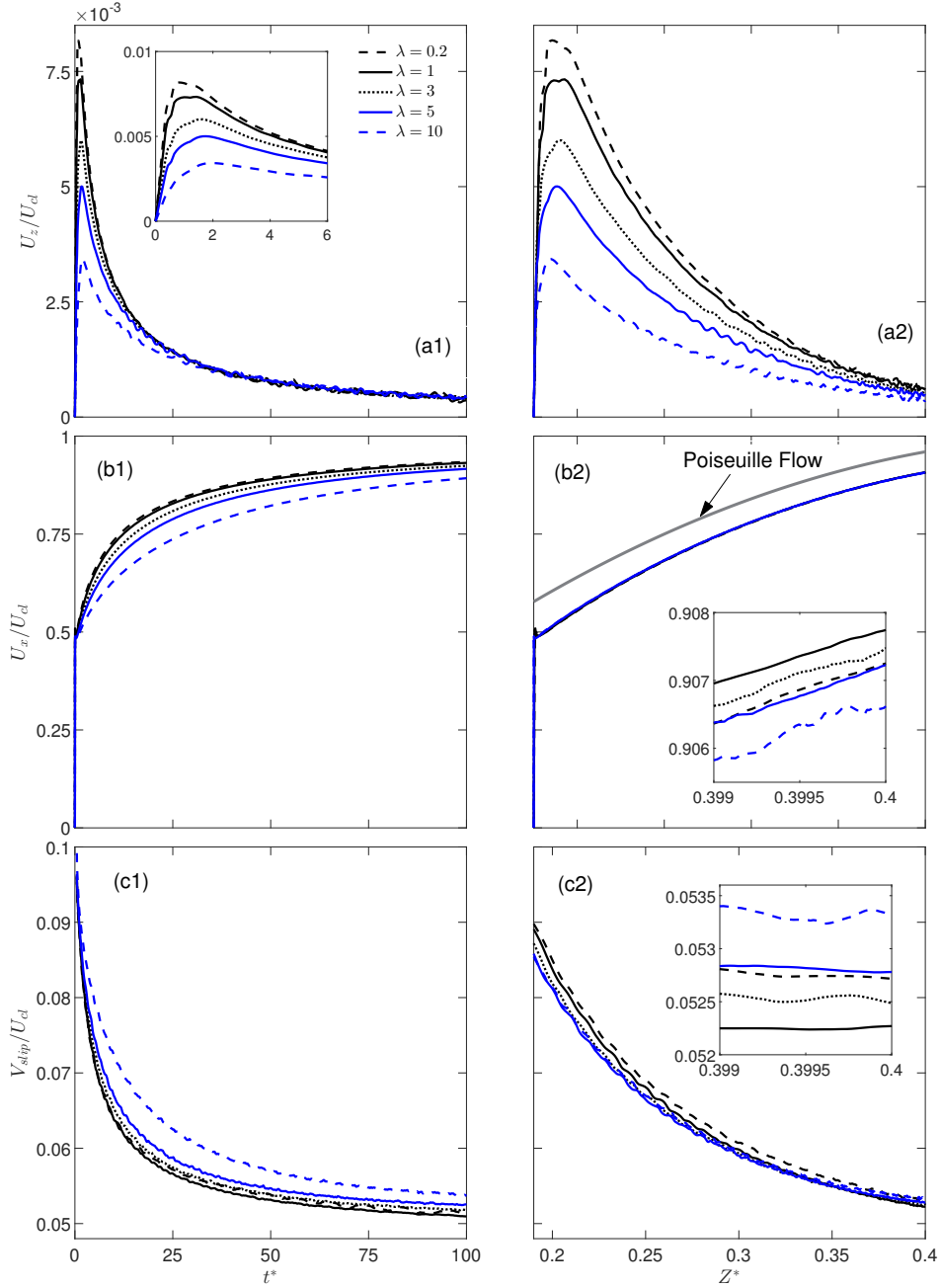


FIGURE 4.7: Variations in (a1 and a2) the migration velocity, (b1 and b2) the axial velocity, and (c1 and c2) the slip velocity plotted with the migration time t^* (a1, b1, c1) and the lateral position Z^* (a2, b2, c2) at different λ values. Also shown in (b2) as a gray curve is the flow velocity from Eq. (4.2) for the undisturbed tube flow.

To analyze the migration process more quantitatively, in Fig. 4.7 (left column), the migration velocity U_z , the axial drifting velocity U_x (both measured at the capsule centroid), and the slip velocity

$$V_{slip} = u_x - U_x \quad (4.4)$$

are plotted with time. Here u_x is the Poiseuille velocity from Eq. (4.2) at the capsule centroid [70].

The general variations for these cases are similar. Upon being released, the capsule starts to migrate toward the tube centerline and migration velocity reaches the maximum value quickly. This initial transient phase is longer for a higher λ , as noticed in Fig. 4.4 and more evident in the inset panel in Fig. 4.7a. After that, the migration velocity U_z gradually decreases with time and becomes indistinguishable among different λ values. This is reasonable by considering the twofold effects of λ : On one side the migration velocity is faster at lower λ , while on the other side the faster migration brings the capsule to a position closer to the tube centerline where the driving factor, the shear gradient, is smaller. These two aspects gradually cancel each other and it can be seen that the $U_z \sim t^*$ curves become close for $t^* > 25$. As for the axial direction, consistent with the axial position plot in Fig. 4.6b, it can be seen that the axial velocity U_x is slightly slower (Fig. 4.7b1), and consequentially the slip velocity V_{slip} is slightly larger (Fig. 4.7c1), for a higher λ .

Recognizing the primary determinant role of Z^* for the capsule dynamics, the capsule velocities with respect to the lateral position Z^* are re-plotted in the right column in Fig. 4.7. Now it becomes clear that, at a same lateral position Z^* and thus a same external shear gradient, the migration velocity is faster for a less viscous capsule (Fig. 4.7a2). As for the axial drifting velocity in Fig. 4.7b2, λ has negligible influence on U_x . The gap between the Poiseuille velocity (gray curve) and the capsule axial velocity represents the slip velocity V_{slip} , which is also displayed in Fig. 4.7c2. No significant difference in V_{slip} is observed as λ varies from 0.2 to 10; instead, the slip velocity is mainly determined by the lateral position Z^* .

The capsule attains an ellipsoid-like shape after the initial transient phase as shown in Fig. 4.4. To characterize the capsule deformation and alignment direction, the deformation index D (Eq. 5.1) and inclination angle θ , and their variations with Z^* are shown in Fig. 4.8 are calculated. Similar to the migration velocity in Fig. 4.7a2, the capsule deformation D undergoes a rapid increase in the initial transient phase and reaches a maximum value (Fig. 4.8a). After that, the capsule gradually rebounds as it moves away from the high-shear region near the tube wall to the low-shear region close to the centerline. On

the other hand, the capsule inclination angle θ exhibits an opposite trend with the lateral position Z^* : it first decreases to a minimum value in the transient period, and then gradually climbs back as the shear gradient becomes weaker (Fig. 4.8b). As for the λ effect, both D and θ decrease with λ ; and similar to our observations in Table 4.1b, they are less sensitive to the change $\lambda = 0.2 \rightarrow 1$ than $\lambda = 1 \rightarrow 5$. It is also interesting to observe that a larger λ postpones the start of recovering trend in θ curves, while on the contrary it promotes the rebounding process in D variations, although both to a relatively minor extend.

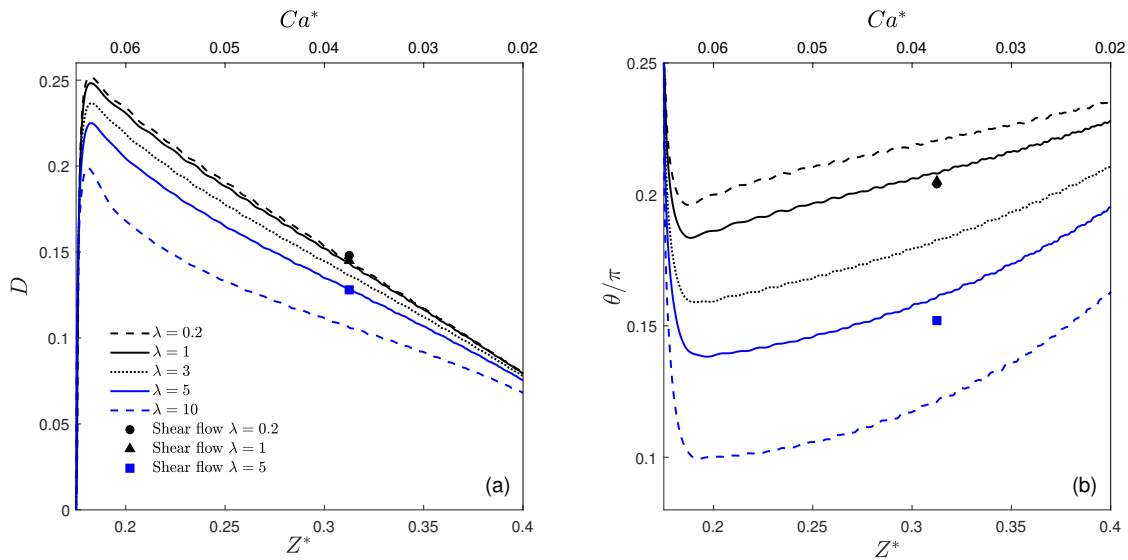


FIGURE 4.8: Evolutions of (a) the deformation index D and (b) the inclination angle θ versus the lateral location Z^* with different λ values. The filled symbols are plotted based on the D and θ results in shear flow at capillary number $Ca = 0.0375$ (Table 4.1).

During the migration process of a capsule, the local capillary number Ca^* is a function of the lateral location Z^* only. For a better representation of the flow situation around the capsule, in Fig. 4.8, the local capillary number Ca^* is also labeled along the top edges. Also, the shear flow results from Table 4.1 for $Ca = 0.0375$ and $\lambda = 0.2, 1, \text{ and } 5$ are added as symbols. It is interesting to see that the capsule deformation is almost the same and the inclination angle is very close ($< 2^\circ$) for the same capillary number (Ca for shear flow and Ca^* for tube flow). This finding suggests that the capsule behavior during the migration process can be approximated with the shear flow situation based on the local capillary number, and the capsule does not have much memory of the previous migration history,

since in this low Reynolds number flow the inertial effect is negligible.

Another feature of the capsule dynamics we would like to examine is the rotation period. Fig. 4.9a plots the rotation angle ϕ of a membrane marker as the capsule migrates. The rotation period T^* can readily be measured between two consecutive maxima at $\phi = \pi$ or minima at $\phi = -\pi$. However, unlike other variables such as the deformation D and migration velocity U_z , only discrete values can be obtained from the ϕ plot for the rotation period T^* , one from each ϕ cycle. For each ϕ cycle, we also calculate the mid-cycle time t^* as the average of the two peaks, and pair the lateral position Z^* at the mid-cycle time t^* with the rotation period T^* in our next analysis, as shown in Fig. 4.9b. Apparently the rotation period is mainly related to the lateral position Z^* ; and this can be associated to the reducing shear gradient as the capsule migrates toward the tube centerline. The λ effect on T^* is less profound, however, still observable. The rotation is slower (i.e., larger T^*) at a higher λ at a same lateral position Z^* , and the difference in T^* is slightly more significant at lower Z^* (i.e., higher Ca^*). This can be attributed to the capsule deformation as shown in Fig. 4.8a: The deformation D is smaller for higher λ , and the difference in D for $\lambda = 0.2 \sim 10$ gradually disappears as the capsule migrates toward the tube center.

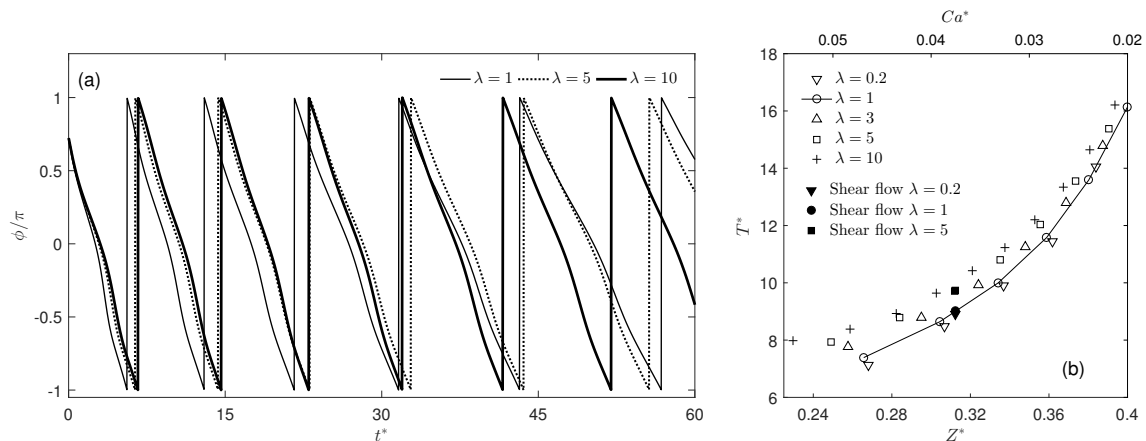


FIGURE 4.9: Variations of (a) the rotation angle ϕ with migration time t^* and (b) the rotation period T^* with lateral location Z^* and local capillary number Ca^* . The filled symbols in (b) depict the converted tank-treading period TTP values for capsules in shear flow with $\lambda = 0.2, 1, \text{ and } 5$ at $Ca = 0.0375$.

The relationships between the rotation period T^* and λ and Ca^* are also consistent with those discussed for the tank-treading period TTP in Table 4.1c. Please note that the TTP

values cannot be compared directly to the rotation period T^* , even with the same capillary number, since TTP is normalized by the inverse of the shear rate $\dot{\gamma}^{-1}$ in Table 4.1c, but for T^* , D_t/U_{cl} is used as the reference time. After appropriate conversion, the TTP values for $Ca = 0.0375$ and $\lambda = 0.2, 1, \text{ and } 5$ are also shown in Fig. 4.9b as symbols for comparison. Similar to the findings in Fig. 4.8, the converted TTP values are close to the rotation periods in tube flow at an equivalent local capillary number.

4.4 Effect of Membrane Shear Viscosity on Capsule Migration

Few studies considered the membrane viscous effect on capsule dynamics in shear flow [84, 83, 54, 46, 58]. However, the impact of membrane viscosity on lateral migration of a viscoelastic capsule in tube flow has not been investigated to my knowledge. The membrane of biological capsules is nearly area incompressible with a large dilatation module, and hence, the dilatation deformation is typically neglected [98, 46, 54]. Following these publications, here only the shear viscosity μ_s of the membrane is considered, which is represented by the shear Boussinesq number $Bq_s = \mu_s/\mu_0 a$. To access the individual effect of the membrane viscosity, we keep the viscosity ratio $\lambda=1$ and capillary number $Ca = 0.2$ fixed, and vary the Boussinesq number $Bq_s=1, 2, 5, 10, 20, 30, \text{ and } 40$. Please note that $Bq_s = 0$ corresponds to the pure elastic membrane studied above.

The lateral location Z^* , migration velocity U_z , slip velocity V_{slip} , and a sequence of the capsule shapes are illustrated in Fig. 4.10 for different Bq_s values. When the membrane viscosity is involved, the capsule deformation reduces (Fig. 4.10d). The reduced capsule deformation with Bq_s has also been noticed in previous studies for shear flows [54, 46, 58]. Accompanied with the smaller deformation, the lateral migration slows down, and the migration velocity decreases. The slip velocity is mainly related to the lateral position Z^* , and the influence of Bq_s is negligible. This is similar to that noticed in Fig. 4.7c2 for different viscosity ratios. Some oscillations can be seen in the migration velocity U_z in Fig. 4.10b for $Bq_s > 20$. This phenomenon has been reported in previous studies for capsule dynamics in shear flow [56, 54], and it is more visible in deformation D and inclination angle θ in Fig. 4.11. Since the capsule membrane experiences continuous variations in the strain status, it is difficult to explain the underlying mechanism for these

oscillations. In general, a large membrane viscosity responds more dramatically to strain rate, which can generate and escalate such oscillations.

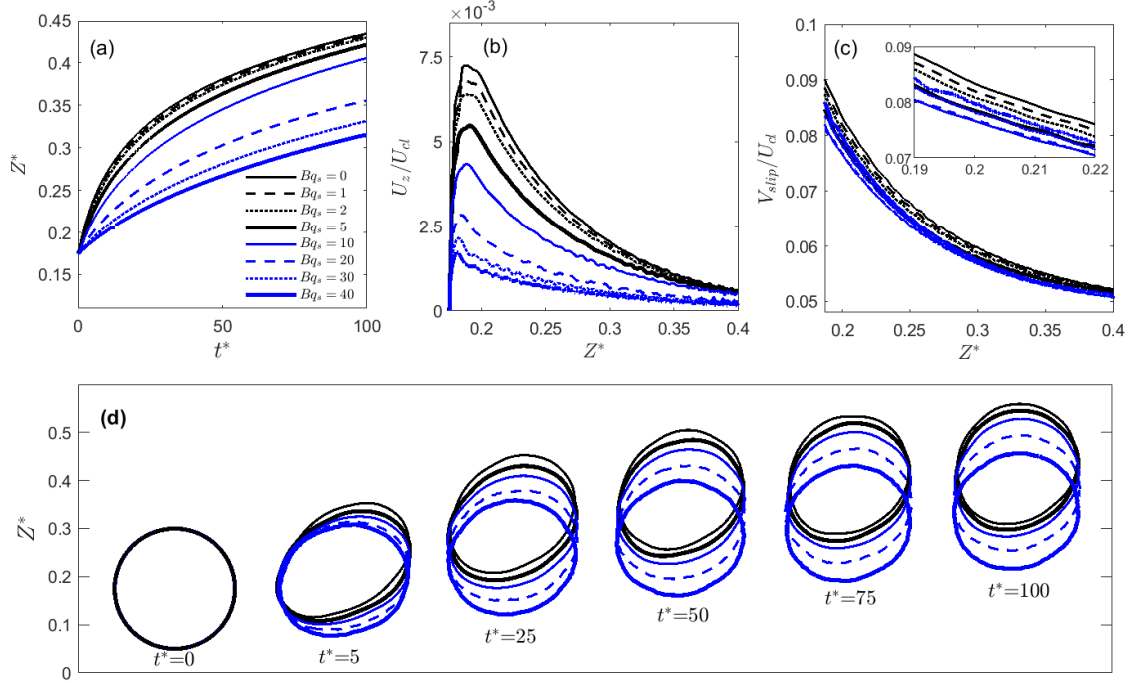


FIGURE 4.10: Effects of the membrane viscosity Bq_s on (a) the lateral location, (b) the migration velocity, and (c) the slip velocity during the migration process. Capsule shapes with different membrane viscosities are also compared in (d) at several time instants.

Variations of the capsule deformation index D and inclination angle θ are collected in Fig. 4.11 for different Bq_s . Similar to the observations in the previous section, the capsule quickly elongates and reaches its maximum D and then rebounds as it migrates toward the tube axis (i.e., smaller Ca^*). On the contrary, θ decreases initially with a steep slope and then increases gradually. The recovering trend in D after the initial transient phase and that in θ for $Bq_s < 5$ are approximately linear; however, it becomes non-linear for θ at higher Bq_s values. Again this is similar to our observations for the effect of λ in Fig. 4.8. In addition, the recovering process can start smoothly for $Bq_s < 10$, and oscillations appear in D and θ for $Bq_s > 20$. The oscillations gradually damp out. In shear flow, both higher λ and Bq_s can induce oscillations in deformation and inclination, but the damping process is relatively faster for oscillations caused by a higher interior fluid viscosity [46]. This might be the reason for not seeing oscillations in higher λ cases in tube flow in the previous section. Furthermore, the inclination angle θ responds to the continuous

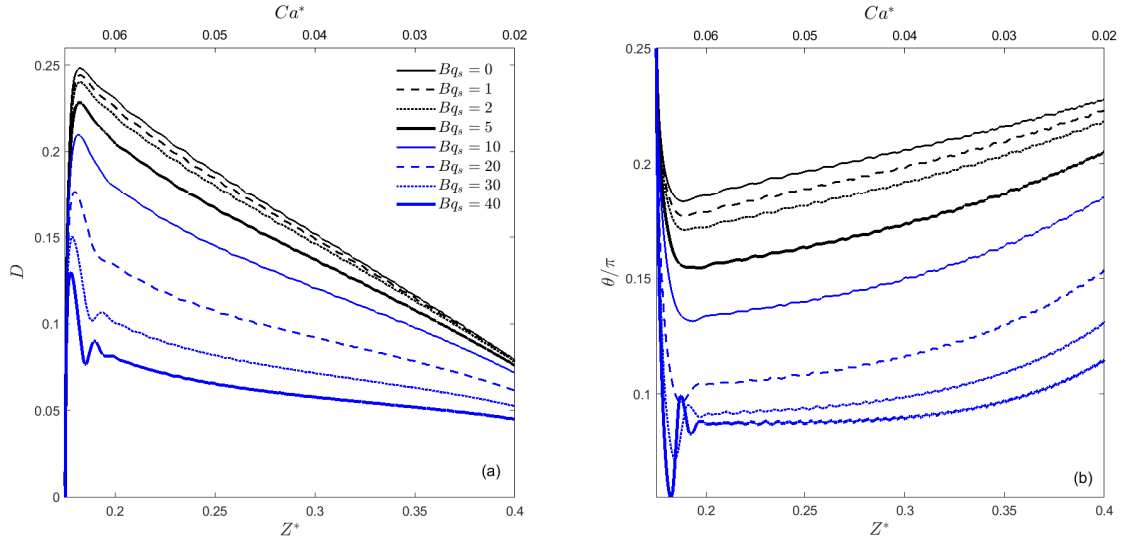


FIGURE 4.11: Effects of membrane viscosity Bq_s on (a) the capsule deformation and (b) the capsule orientation as a function of lateral position Z^* .

increase in Bq_s differently from the deformation D in Fig. 4.11a, and the θ response to λ change in Fig. 4.8b: θ decreases much less at higher Bq_s . Actually, the $\theta \sim Bq_s$ trend even reverses in shear flows, i.e., θ starts to increase with Bq_s for high Bq_s values [46]. We do not see the turning back in $\theta \sim Bq_s$ here, probably because the ambient flow situation is dynamically changing.

The effect of membrane viscosity Bq_s on the capsule rotation during the migration process is shown in Fig. 4.12. The capsule rotation slows down with time, and the decrease in rotation speed is slower for higher Bq_s (Fig. 4.12a). As discussed above, the difference in the rotation reduction rate is mainly due to the slower migration at higher Bq_s . This becomes apparent when we plot the rotation period T^* vs. the lateral location Z^* in Fig. 4.12b, where the local capillary number Ca^* is also labeled along the top edge. In general, our discussions on the promoting effect from a larger shear gradient and the inhibiting influence from a smaller D on capsule rotation still hold here; however, one should not expect a monotonic one-to-one $D \sim T^*$ relationship considering the complex flow-membrane interaction in the system, as revealed in previous studies [9, 46]. In addition, the period T^* is obtained over a rotation cycle and it may not match the capsule rotating speed at the mid-cycle instant where Z^* and Ca^* are calculated.

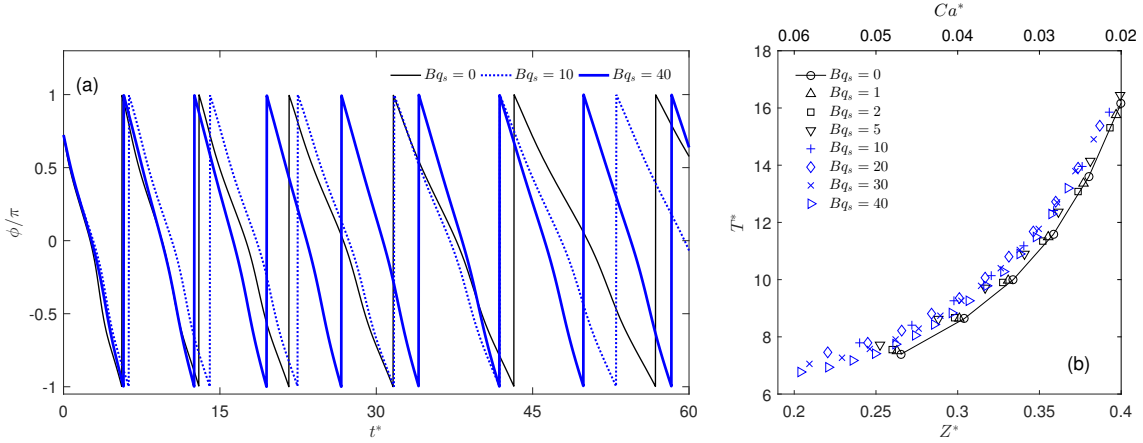


FIGURE 4.12: Effects of the membrane viscosity Bq_s on (a) the rotation angle ϕ and (b) the rotation period T^* . Both the lateral position Z^* and the local capillary number Ca^* are labeled in (b) along the horizontal axis.

4.5 Effect of Capillary Number on Capsule Migration

In previous sections the capillary number is kept constant at $Ca=0.2$ and only one system parameter, λ or Bq_s changes, to investigate their individual effects on the migration dynamics. The capillary number Ca , a direct reflection of the relative strength of the tube flow to the membrane elasticity, is of great interest for capsule and droplet dynamics in various flows [68, 83, 54, 81]. To elucidate the impact of the system capillary number Ca in the capsule migration process, here we consider two different capillary number values, $Ca = 0.05$ and 0.4 . A smaller Ca value can be interpreted as a less flexible membrane, and/or a stronger external flow influence. For the convenience, we take the membrane flexibility interpretation in the next discussion. In addition, to have a better understanding of the interplay among system control parameters, we consider three different membrane viscosity values at $Bq_s = 0, 10$, and 40 . The viscosity ratio is set constant at $\lambda = 5$, which is the typical value for RBCs [1, 98].

Fig. 4.13 depicts the variations of lateral distance Z^* , migration velocity U_z and slip velocity V_{slip} , and the evolution of capsule shapes. Clearly, the increased membrane flexibility with $Ca = 0.4$ significantly enhances the capsule deformation, especially for low Bq_s numbers (Fig. 4.13d). The high membrane viscosity at $Bq_s = 40$ restricts the capsule deformation and thus the difference between $Ca = 0.05$ and 0.4 is less dramatic. Consequently, compared to its counterpart with $Ca = 0.05$, the capsule with $Ca = 0.4$ migrates

faster toward the tube centerline (Fig. 4.13 a, b). Exception is noticed in the early stage of the migration for the cases with $Bq_s = 40$: The migration for the more flexible capsule with $Ca = 0.4$ is slightly behind that of the less flexible capsule of $Ca = 0.05$ (Fig. 4.13b). This is due to the strong oscillations in capsule deformation and orientation (Fig. 4.14) caused by the strong membrane viscosity ($Bq_s = 40$) on the more flexible membrane ($Ca = 0.4$). Once the initial strong oscillations damp to smaller magnitudes at $Z^* = 0.2$, the $Ca = 0.4$ migration curve catches up the $Ca = 0.05$ curve and stays above it in the rest of the migration process (Fig. 4.13b). Overall, the membrane viscosity, as Bq_s increases from 0 to 40, has a much stronger influence on the more flexible capsule with $Ca = 0.4$. As for the slip velocity V_{slip} , the general trend of declining V_{slip} with Z^* agrees well with those observed in Figs. 4.7c2 and 4.10c. However, the difference in V_{slip} among cases is more evident in Fig. 4.13c; and this is due to the large differences in the capsule deformation D (Fig. 4.14a) and migration velocity U_z (Fig. 4.13b). Another interesting feature noticed here is that, unlike the positive correlation between U_z and V_{slip} demonstrated in Figs. 4.7 and 4.10, the faster lateral migration velocity U_z is accompanied with the slower slip velocity V_{slip} from $Ca = 0.4$. We speculate that this is because of the low inclination angle in Fig. 4.14b: The small θ angle means the largely deformed capsule aligns closer to the flow direction and thus a lower resistance is expected.

As referred above, Fig. 4.14 shows the evolution of the capsule deformation D and inclination angle θ for the cases tested here with different Ca and Bq_s values at $\lambda = 5$. The capsule deformation D decreases as the membrane flexibility reduces (smaller Ca) or the membrane viscosity increases (larger Bq_s), and the Bq_s impact on D is more profound for the more flexible capsule of $Ca = 0.4$. On the other hand, the inclination angle θ responds to the change in Bq_s differently. For the less flexible membrane of $Ca = 0.05$, θ keeps decreasing as Bq_s increases from 0 to 40. At $Ca = 0.4$ (more flexible membrane), θ firstly declines as Bq_s changes from 0 to 10; As Bq_s further increases from 10 to 40, large oscillations are developed in deformation D and inclination angle θ , and the mean θ value is approximately the same as for $Bq_s = 10$. The oscillation magnitude quickly drops down, however, it takes a relatively long time for the low magnitude oscillations to completely disappear at $Z^* > 0.35$, where the capsule has migrated very close to the tube centerline

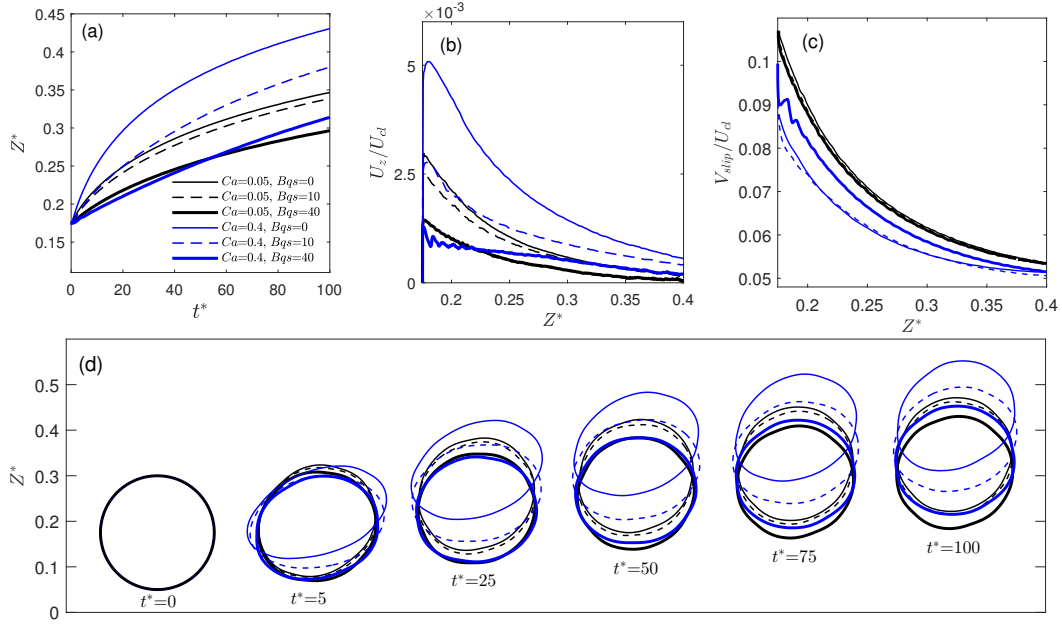


FIGURE 4.13: Effects of the capillary number Ca on (a) the lateral location, (b) the migration velocity, and (c) the slip velocity during the migration process. Here the viscosity ratio is $\lambda = 5$ and three different membrane viscosity values are considered: $Bq_s = 0, 10,$ and 40 . Capsule shapes with different Ca and Bq_s values are also compared in (d) at several time instants.

and the shear gradient has greatly reduced. These descriptions are consistent with observations in previous sections for the λ and Bq_s effects and previous studies for capsules in shear flows [56, 46, 54].

Moreover, the data points for the tank-treading capsules in shear flow with $\lambda = 5$, $Bq_s = 0$, and $Ca = 0.0375$ and 0.075 from Table 4.1 are also plotted. It can be seen that the data points are close to the D and θ curves for $Ca = 0.4$ and $Bq_s = 0$, suggesting the simultaneous status of the migrating capsule can be adequately approximated by the tank-treading motion of the capsule at the equivalent capillary number. Please note that, for a same lateral position Z^* , the local capillary number Ca^* is different for the capsule of $Ca = 0.05$ and $Ca = 0.4$. For this reason, we label the top edge of Fig. 4.14b with the values of $Ca_{0.4}^*$, the local capillary number for the $Ca = 0.4$ capsule. The local capillary number $Ca_{0.05}^*$ for $Ca = 0.05$ is related to $Ca_{0.4}^*$ at a same Z^* as $Ca_{0.4}^*/Ca_{0.05}^* = 0.4/0.05 = 8$, as indicated in the top axis caption of Fig. 4.14. For the migration process from $Z^* = 0.175$ to 0.41 , $Ca_{0.4}^*$ reduces from 0.13 to 0.036 , and $Ca_{0.05}^*$ decreases from 0.016 to 0.005 . The minimum capillary number considered in Table 4.1 is 0.0375 , so there is no comparable

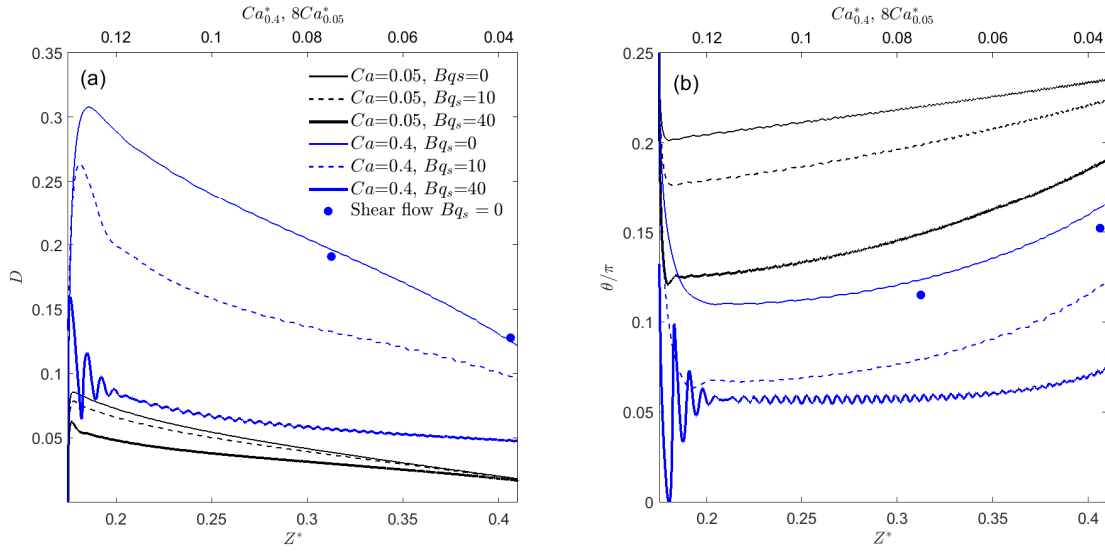


FIGURE 4.14: Effects of the capillary number Ca and membrane viscosity Bq_s on (a) the capsule deformation D and (b) the inclination angle θ . Both the lateral position Z^* (bottom) and the local capillary number Ca^* (top) are labeled along the horizontal axis. Please note that, since different capillary numbers Ca are used in these cases, the local capillary number Ca^* is different for cases with $Ca = 0.05$ and $Ca = 0.4$, even at a same position Z^* . The filled symbols represent the tank-treading results in shear flow for elastic capsules at capillary number $Ca = 0.0375$ and 0.075 with $\lambda = 5$.

cases for the $Ca = 0.05$ curves.

As done in previous sections, next we look at the capsule rotation behavior during the migration at different capillary number Ca . For clarity, Fig. 4.15a shows only the variations of rotation angle ϕ for four representative cases with $(Ca, Bq_s) = (0.05, 0)$, $(0.05, 40)$, $(0.4, 0)$, and $(0.4, 40)$. While for all cases the rotation is slowing down with time t^* , the slowing down process is more dramatic for case $(Ca, Bq_s) = (0.4, 0)$ and more gentle for case $(Ca, Bq_s) = (0.05, 40)$. This observation again is mainly due to the difference in capsule deformation: the largest deformation is found for the more flexible, pure elastic capsule in case $(Ca, Bq_s) = (0.4, 0)$, and the smallest deformation is from the less deformable, highly viscous capsule case $(Ca, Bq_s) = (0.05, 40)$ (Fig. 4.14a).

To have a more meaningful comparison of the rotation period among cases, in Fig. 4.15b, we plot T^* versus the mid-cycle lateral position Z^* for all the six cases in Figs. 4.13 and 4.14. Again we see the rotation period T^* increases with Z^* as the local shear gradient decreases for all cases. The membrane viscosity Bq_s exhibits negligible effect for $Ca = 0.05$ cases, since the deformation D is small for the less flexible capsule.

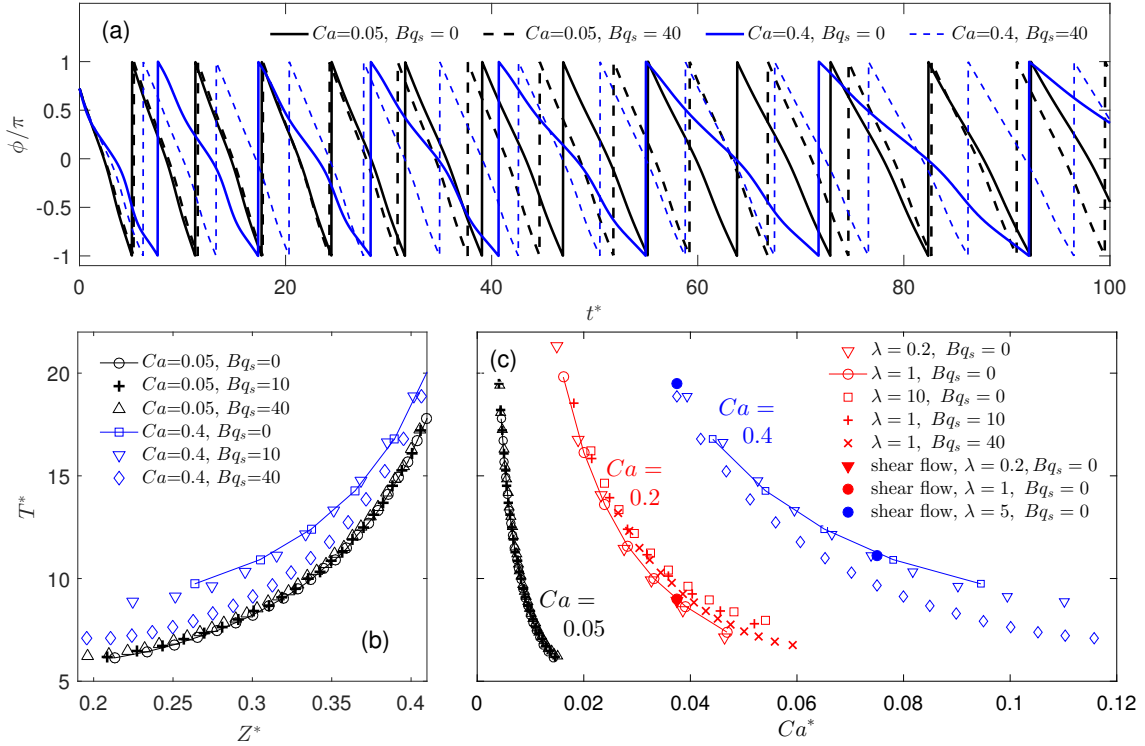


FIGURE 4.15: Effects of Ca and Bq_s on (a) the capsule rotation angles ϕ and (b and c) the rotation period T^* . Since the cases with $Ca = 0.05$ and 0.4 have different local capillary number Ca^* values at a same lateral position Z^* , the data points for $Ca = 0.05$ and 0.4 appear as two separate groups in the $T^* \sim Ca^*$ plot in (c). Also added there are the results (in red color) from Figs. 4.9b and 4.12b for $Ca = 0.2$, and the tank-treading results (filled symbols) for capsules with $\lambda = 0.2, 1$ and 5 at $Ca = 0.0375$ and 0.075 .

On the other hand, the relatively large difference in capsule deformation caused by changes in Bq_s for the more flexible membrane is evident in the rotation period T^* for $Ca = 0.4$. Since different capillary numbers are used in these cases and they do not share the same local capillary number Ca^* at a same Z^* location, we plot the $T^* \sim Ca^*$ data points as an extra figure in Fig. 4.15c. The tank-treading period TTP for $\lambda = 5$ and $Ca = 0.0375$ and 0.075 for shear flow from Table 4.1c are also shown as filled blue circles. These two data points match the curve for $Ca = 0.4$ and $Bq_s = 0$ (blue line) very well, implying that the capsule rotation during the migration is very similar to that in the shear flow with an equivalent capillary number. Also displayed there are data points from Figs. 4.9b and 4.12b with $Ca = 0.2$.

Looking at the data points all together in the $T^* \sim Ca^*$ plot, few remarks can be drawn:

(1) The rotation period T^* decreases with the local capillary number Ca^* , following approximately a hyperbolic trend; (2) At a same Ca^* , T^* increases with the global capillary number Ca ; And (3) other than Ca^* and Ca , the relatively minor influences from λ and Bq_s on T^* can be related to their effects on the capsule deformation D : The larger the deformation, the larger the rotation period T^* . These correlations are helpful for the search of empirical relationships for the capsule migration velocity and rotation period in the next section.

4.6 Empirical Relationships for Migration Velocity and Rotation Period

The clear pattern observed in Fig. 4.15c suggests the possibility to establish an empirical relationship for the rotation period T^* . Another parameter of great interest for capsule migration is the migration velocity U_z . Doddi and Bagchi [70] presented a relation for the migration velocity of an elastic capsule in a plane Poiseuille flow by considering Ca , Z^* , and capsule-to-channel size ratio. In addition, Singh et al. [99] proposed a power law correlation for the migration velocity with respect to Ca and Z^* for an elastic capsule in plane shear near a wall. These studies were for shear flows and pure elastic capsule membranes, and the rotation period T^* was not considered. While the control parameters for the systems considered in this study include λ , Bq_s , and Ca , our results and analysis, in particular the $T^* \sim Ca^*$ plot in Fig. 4.15c, manifest the strong dependence of the rotation time T^* on Ca , Ca^* , and D . Similar relationship is also noticed in our discussions in previous sections for the migration velocity U_z . Therefore, it seems more reasonable to express U_z and T^* with respect to D , Ca , and Ca^* . Based on our simulation results in this study, we establish the following approximate relations for U_z and T^* as

$$\frac{U_z D^{0.75}}{U_{cl}} = 0.05881 \left(\frac{Ca}{Ca^* D} \right)^{-1.464}, \quad (4.5)$$

and

$$\frac{T^*}{D} = 1.586 \left(\frac{Ca}{Ca^* D} \right) + 14.6. \quad (4.6)$$

The relations are written in this particular fashion such that we have only one group parameter Ca/Ca^*D on the right hand sides, and hence we can compare the numerical results from our simulations to the predictions from these equations in 2D graphs, as shown in Fig. 4.16. Here, the gray lines are plotted using Eqs. (4.5) and (4.6), and the data points are taken at the mid-cycle instants with various combinations of λ , Bq_s , and Ca . All cases in this study are included, except the cases with $(Ca, \lambda, Bq_s)=(0.2, 1, 1)$ and $(0.2, 1, 2)$, since their results are very close to the case $(Ca, \lambda, Bq_s)=(0.2, 1, 0)$ (see Figs. 4.10-4.12). The agreement for the rotation period in Fig. 4.16b is surprisingly excellent. On the other hand, while Eq. (4.5) can describe the data point distribution also pretty well in Fig. 4.16a, some discrepancies do exist in the migration velocity, especially for low Ca/Ca^*D values. For a given Ca , a small Ca/Ca^*D suggests a large D or Ca^* , both typically occur in the early stage of the migration. It should be mentioned that the data point values are less accurate in the early period, as the capsule is still recovering from the sudden large deformation at the beginning of the simulation. Singh et al. [99] experienced similar issues for the migration velocity of elastic capsule in plane shear flows near wall. They found that the predicted migration velocities fail to collapse to a single curve beyond a critical capillary number Ca_{cr} , and they proposed two different relations, one for $Ca > Ca_{cr}$ and one for $Ca < Ca_{cr}$. Nevertheless, we are satisfied with the overall good prediction quality for the migration velocity from Eq. (4.5).

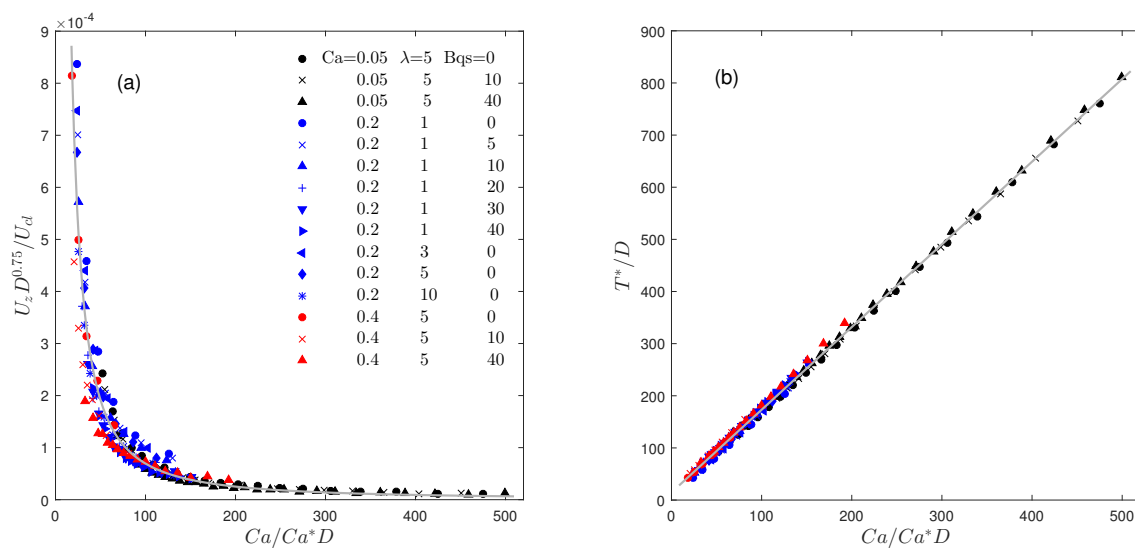


FIGURE 4.16: Comparisons of (a) the migration velocities and (b) the rotation periods from numerical simulations (symbols) with the predictions from Eqs. (4.5) and (4.6) (gray lines).

It is interesting to see that the global and local capillary numbers, Ca and Ca^* , appear as a ratio term in these equations. From their individual definitions, one can show

$$\frac{Ca}{Ca^*} = \frac{R_t/a}{1 - 2Z^*}, \quad (4.7)$$

which depends only on the normalized lateral position Z^* for the systems in this study with a constant tube-capsule size ratio $R_t/a = 2$. Considering Eq. (4.7) together with Eqs. (4.5) and (4.6), it can be said that the migration velocity and rotation period (please note that T^* is the rotation period normalized by D_t/U_{cl} .) are mainly related to the tube flow strength (represented by the centerline velocity U_{cl}), the normalized lateral position Z^* , and the capsule deformation D . This dependence clearly elucidates the fact that the capsule migration is determined by the local flow situation (U_{cl} and Z^*) and capsule deformation (D), which are the major mechanisms for the lateral migration phenomenon. Therefore, although Eqs. (4.5) and (4.6) are obtained purely by numerical fitting, they do, to a certain extent, reflect the physical relationships among these parameters. This does not imply that the capsule properties, such as the interior fluid viscosity, the membrane viscosity, and membrane flexibility, are irrelevant to the migration behaviors; instead, these capsule properties play their roles indirectly by affecting the capsule deformation. At last, we should mention that the system we consider in this study, in principle, is a multiple variable system and there is no theoretical proof that an exact one-to-one relationship exists between two nondimensional parameters. The dynamically varying inclination angle, as well as the various capsule shapes, for sure are also involved in the migration process, although in a less apparent and significant fashion. This may also explain the data point deviations from the empirical relation in Fig. 4.16a.

4.7 Summary and Further Discussions

In this chapter, extensive 3D simulations have been conducted for the lateral migration of viscoelastic capsules in tube flows with various interior-exterior viscosity ratios, membrane viscosities, and capillary numbers. The methodology is validated carefully by comparing the capsule deformation index, inclination angle, and rotation period in shear flow

to previous publications, and good agreement is observed. Furthermore, the migration process of a rigid spherical particle in tube flow has also been simulated. The Segre-Silberberg effect is successfully reproduced and the results agree well with those in the literature.

The simulation results show that, after being released from a location close to the tube wall, a capsule starts to migrate toward the tube centerline. Unlike solid particles, there is no lateral equilibrium position and the capsule migration continues till it reaches the centerline, where the shear gradient disappears. There is a very short initial transient phase, during which the capsule undergoes large deformation and tilts to a low inclination angle close to the flow direction. The capsule quickly responds to this large deformation and rebounds back gradually. Consequently, there is a maximum for the capsule deformation, a maximum in the migration velocity, and a minimum for the capsule inclination angle at the end of the initial transient phase. During the migration, the capsule is also rotating about its center, and the rotation slows down gradually as the capsule migrates toward the low shear gradient central region. The analysis of the results shows that, compared to the normalized lateral position Z^* , the local capillary number Ca^* provides a better representation for the local flow-capsule situation during the migration process. Individual and combined effects on capsule migration behaviors from the fluid viscosity ratio λ , membrane viscosity Bq_s , and the capillary number Ca have been examined. The results show that both the capsule deformation D and the inclination angle θ decrease with the viscosity ratio λ and the membrane viscosity Bq_s , but θ becomes less sensitive to higher Bq_s values. In the meanwhile, oscillations are introduced in the capsule deformation, inclination angle, and migration velocity for a highly viscous membrane. While the oscillations quickly damp to much smaller magnitudes, it may take a relatively long time for them to completely die out, especially in the inclination angle for a more flexible membrane at high capillary number Ca . Furthermore, as the capillary number Ca increases from 0.05 to 0.4, the capsule deformation increases and the inclination angle decreases. Due to the large deformation with $Ca = 0.4$, both the migration velocity and rotation period increase significantly. The capsule deformation, inclination angle, and rotation period for elastic capsules in shear flows have also been compared to those with

equivalent local capillary numbers during the migration process, and a good agreement is obtained for all these characteristic features. This finding suggests that the shear flow results can be used to approximate the capsule behaviors during the migration process in future studies. At last, empirical relations have been proposed for the capsule migration velocity and rotation period with satisfactory agreement.

We acknowledge that the present simulations are limited to the migration process of an isolated spherical capsule, and the individual and combined roles of other parameters and more complex situations, such as the capsule-to-channel size ratio, the non-spherical capsule shape, the strong membrane dilation resistance, and motion of multiple capsules in suspensions, have not been considered in this study. Nevertheless, the results and information revealed from this research are interesting and could be helpful for better understanding the complicated flow-capsule interaction in the migration process.

Chapter 5

Membrane Viscous Effects on the Tank-Treading Dynamics of RBC in Simple Shear Flow

In this chapter, the impact of membrane viscosity on the tank-treading dynamics of RBC is investigated. To simulate the tank-treading motion of a RBC, appropriate values of the mechanical properties of the cell, including elastic shear modulus E_s , bending E_b and dilation moduli E_d , should be utilized in the computer programs. However, as mentioned in Chapter 2, the measured values for these mechanical properties show large variations. To clear this concern and make sure that the RBC parameters used are reasonable, validation tests are first performed for the stretching process of a RBC in optical tweezers. I then conduct comprehensive simulations with different cell properties and flow conditions, and compare the tank-treading frequency, deformation index, and inclination angle of the cell from simulations to experiments. My results show that the experimental results can be reasonably reproduced without introducing the shear-thinning model for membrane viscosity.

5.1 RBC Deformation Under External Stretching Load

As discussed in Chapter 2, stretching a RBC in optical tweezers is accomplished by exerting external mechanical loads on the opposite sides of the cell. Under this external loads,

the RBC elongates and attains a steady deformation. A benefit of this experiment is that the fluid and membrane viscosity are not involved in the steady elongation of the cell as confirmed in Ref. [59]. Therefore, a good agreement between the simulations and experimental results can help to justify the values for E_s , E_b , and E_a utilized in our following simulations.

The tensile stretching of the human RBC in optical tweezers is simulated as follows. The RBC, which is initially at rest, is placed at the center of a cubic domain with size of $24.7 \times 24.7 \times 24.7 \mu\text{m}$ ($76 \times 76 \times 76$ in lattice unit δx). The cell membrane is discretized into 5120 triangular elements and its parameters are listed in Table 5.1. Two external forces with equal value and in opposite directions along X -axis are exerted to the RBC surface nodes at edges, as displayed schematically in Fig. 5.1. The force F is distributed evenly on the nodes on the periphery of the contact area of the microbeads with the cell surface.

TABLE 5.1: The RBC parameters

Radius	$3.9 \mu\text{m}$ [58]
Elastic shear modulus E_s	$5.3 \mu\text{N/m}$ [58]
Elastic dilatational modulus E_a	$50E_s$ [58]
Bending modulus E_b	$2 \times 10^{-19} \text{ Nm}$ [58]

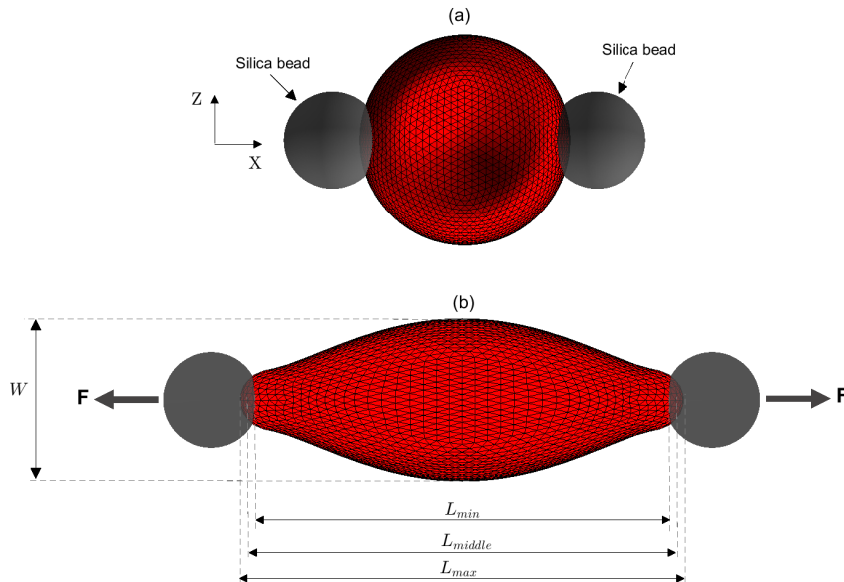


FIGURE 5.1: Schematic illustrations of (a) the undeformed RBC at rest with silica microbeads attached to the cell surface from opposite sides and (b) the elongated cell under external load of F . W is the transverse length of the cell and the axial lengths L_{min} , L_{middle} , and L_{max} are indicated based on different methods for calculating the axial length (see text for details).

After the external forces are imposed, the cell gradually deforms to reach an equilibrium stretched state. The transverse length W can be readily obtained by comparing the maximum and minimum positions of the membrane nodes along transverse direction. For the axial length, different methods had been used in previous studies, such as the distance between the periphery of the force contact areas from two sides [100], the distance between the middle positions of the force contact areas [64], and the maximum distance between the membrane node positions along the axial direction [39]. These distances are indicated by L_{min} , L_{middle} , and L_{max} , respectively, in Fig. 5.1b. Here, to provide better comparisons, all of these distances are considered and the differences between them are presented as error bars. The deformation index can then be defined as

$$D_{xz} = \frac{L - W}{L + W} . \quad (5.1)$$

The RBC stretching simulations are conducted with different external forces and the results are compared with those from experimental measurements [101] in Fig. 5.2.

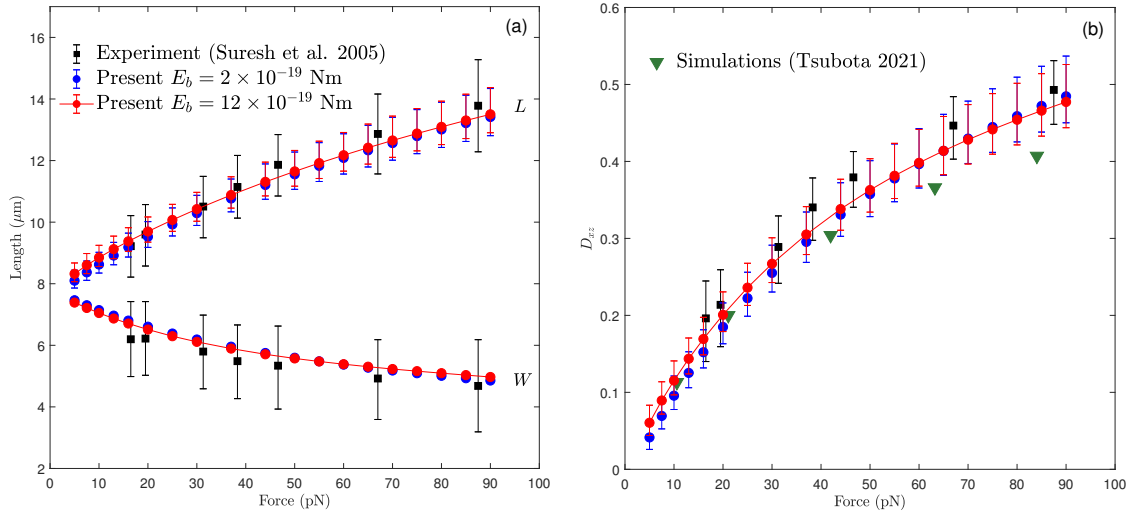


FIGURE 5.2: Comparisons between (a) the axial L and transverse W lengths of the RBC and (b) the deformation index D_{xz} obtained from present simulations and those from optical tweezers experiments [101]. Also shown in (b) as green symbols are the simulation results from Tsubota [64].

It can be seen that there is a good agreement between our simulations and experiments, and thus confirms that the mechanical properties listed in Table 5.1 are appropriate. The simulation results obtained by Tsubota [64] are also depicted in Fig. 5.2b to show the

relatively poor agreement achieved in Ref. [64], particularly at higher external forces. In addition, the simulations are also performed with bending modulus of $E_b = 12 \times 10^{-19}$ Nm (six times of the value in Table 5.1) to confirm that the simulation results are relatively insensitive to the utilized bending modulus.

5.2 Simulation Setup for Tank-Treading Dynamics of RBC

In the following simulations for RBCs in shear flow, the undeformed RBC is placed at the center of a domain with size of $37.3 \times 24.9 \times 24.9 \mu\text{m}$ ($180 \times 120 \times 120$ in lattice unit δx). To impose a simple shear flow, the top and bottom domain boundaries are treated as solid walls moving at velocity U_0 , however, in opposite horizontal directions (Fig. 5.3). This generates a simple shear flow with shear rate of $\dot{\gamma} = 2U_0/H$, where H is the distance between the top and bottom boundaries. Periodic boundary conditions are also imposed along the X and Y directions.

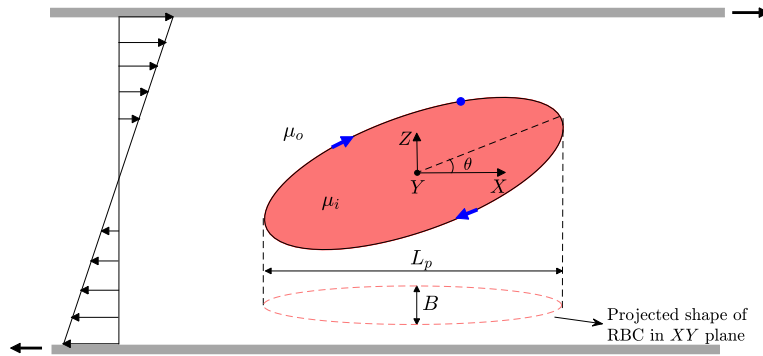


FIGURE 5.3: Illustration of the deformed RBC subject to the simple shear flow. The projected length L_p and width B of the cell in XY plane are used to characterize the cell deformation as L_p/B . The inclination angle θ is defined as the angle between the flow direction and the major axis, and the membrane rotation is indicated by blue arrows.

After the shear flow is imposed, the RBC elongates and aligns itself with an angle θ from the flow direction, similar to the tank-treading dynamics of elastic capsule in Section 4.1.1. It should be noted, however, that depending on the imposed shear rate and exterior viscosity, the cell can oscillate about a mean inclination angle, which is accompanied

by oscillations in its deformation. Following the rheoscopic experiments [48] on RBC tank-treading dynamics, the cell deformation index is defined as the ratio of its projected length L_p to the projected width B in XY plane (Fig. 5.3). The tank-treading frequency TTF (in s^{-1}) can be calculated from the trajectory of a membrane marker point in the middle shear plane. With this setup, the impacts of membrane/interior fluid viscosities on the tank-treading dynamics of the RBC is investigated in the following sections.

5.3 Membrane and Interior Viscous Effects on the Tank-Treading Dynamics of RBC

As mentioned in Chapter 2, there are only few previous studies [39, 60, 62, 64] focusing on the effects of membrane viscosity on the tank-treading dynamics of RBC; however, several concerns exist in these studies, such as neglecting the cell deformation and orientation and the poor agreement compared to optical tweezers experimental results. To address these concerns, a detailed investigation of the tank-treading dynamics of RBC is required. Unlike our nondimensional study in Chapter 4, here, the simulation results are provided in physical units to enable direct comparisons with experimental results.

With the appropriate agreement achieved in the above validation tests, the mechanical properties of the RBC listed in Table 5.1 are used in the following simulations. It should be mentioned that at low shear rates, compressive stresses may develop on the cell surface, which leads to membrane buckling and formation of wrinkles [81]. In addition, including the membrane viscosity can compound this issue as it may generate oscillations in the deformation and orientation of the cell [54, 55, 46]. To mitigate these difficulties and improve stability of the simulations, larger values of the bending modulus can be utilized. Please note that this has negligible impact on the cell deformation (see Fig. 5.2) and has been previously adopted in the literature [62, 102, 103, 104].

Fischer and co-workers [30, 48, 49] studied the RBC dynamics in shear flow by rheoscopy. In these studies, the exterior fluid was dextran suspensions of viscosity in the range of $10.7 \sim 109.3$ cP. Also, they imposed different shear rates $\dot{\gamma}$ from about 1 to $260 s^{-1}$ [30, 48,

49] by controlling the rheoscope rotation speed. Fig. 5.4 shows the experimental conditions in these studies, as well as the exterior fluid viscosity μ_o and shear rate $\dot{\gamma}$ values considered in the present simulations. In addition, the conditions considered by Matteoli et al. [62] and Tsubota [64] are also shown in Fig. 5.4. It can be seen that Refs. [62, 64] have only considered a narrow range of the available experimental data.

From the literature, the membrane viscosity of RBC is in the range of $(0.53 \sim 10) \times 10^{-7}$ mPas [58]. Accordingly, we consider $\mu_s = 0$ (pure elastic membrane), 1×10^{-7} , and 5×10^{-7} mPas. In addition, the reported values for cytoplasm (interior fluid) viscosity μ_i show a large spectrum from 6 to 46 cP [9, 98, 105]. Refs. [62] and [64] considered fixed μ_i values of 10.78 and 28.9 cP, respectively, which might not be the real μ_i for the cells employed in the experiments. In this study, we consider three different values of $\mu_i=6, 10,$ and 15 cP. Therefore, as shown in Fig. 5.4 and discussed above, we have 12 different $\mu_o \sim \dot{\gamma}$ situations, 3 different membrane viscosities, and 3 different interior fluid viscosities, which results in 108 cases in total.

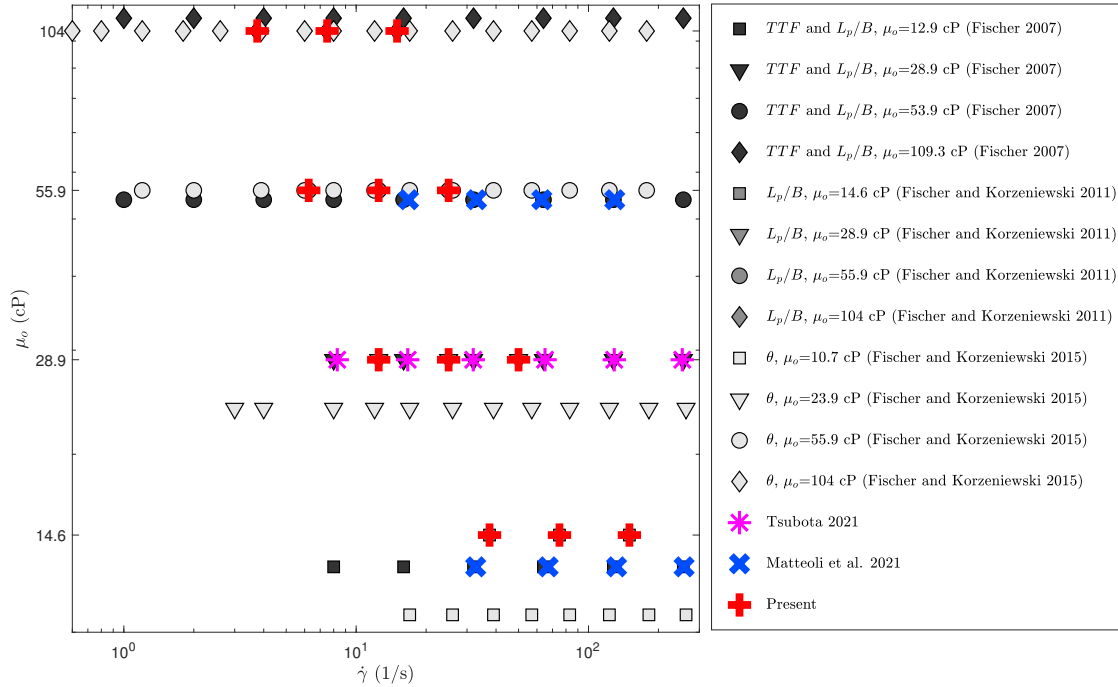


FIGURE 5.4: Range of the exterior fluid viscosity μ_o and shear rate $\dot{\gamma}$ used in present simulations and experiments [30, 48, 49]. The conditions considered in Refs. [62, 64] are also shown for comparison.

The tank-treading motion of RBC in simple shear flow is a dynamic process, in which

the cell deformation and inclination angle oscillate about mean values [9]. Therefore, the simulations are performed until these characteristics reach periodic variations, and then the minimum, mean, and maximum values of TTF , L_p/B , and θ are calculated over the last three periods.

5.3.1 Tank-Treading Frequency

We first look at variations of TTF as a function of shear rate for four different exterior viscosities, as depicted in Fig. 5.5 in logarithmic scale. For the simulation results, the mean values of TTF are indicated by the filled symbols, while the minimum and maximum values are presented by error bars. Please note that the error bars for the simulation results are not clearly noticeable because the maximum and minimum values of TTF are close to each other. For the experimental results from Fischer [30], the TTF values of the cells for all three donors are considered and shown as gray error bars. In Figs. 5.5(a, c, and d), the experimental results are not available at the μ_o values we used in the simulations, and hence, the experimental results at close μ_o values are presented for approximate comparisons. It can be seen from Fig. 5.5 that TTF increases with shear rate, which is in agreement with the experiments. In general, for all flow situations tested, TTF reduces with both membrane viscosity and interior fluid viscosity. This reduction is caused by the additional dissipation in the membrane and/or the interior fluid, which is consistent with the observations from previous studies [62, 64]. However, some irregular but minor variations occur at small shear rates with high membrane viscosity (see insets in Fig. 5.5d), which are attributable to oscillations caused by the membrane viscosity. In addition, compared to the experimental results, TTF values for $\mu_i = 6$ cP are somewhat overpredicted at different μ_o for the pure elastic RBC ($\mu_s = 0$). Even for higher internal fluid viscosities of $\mu_i = 10$ and 15 cP, one can see that the results are close to the upper range of the experimental results. However, including the membrane viscosity can efficiently slow down the tank-treading motion and reduce TTF . This suggests that the membrane viscosity cannot be neglected for a good agreement of TTF in Fig. 5.5.

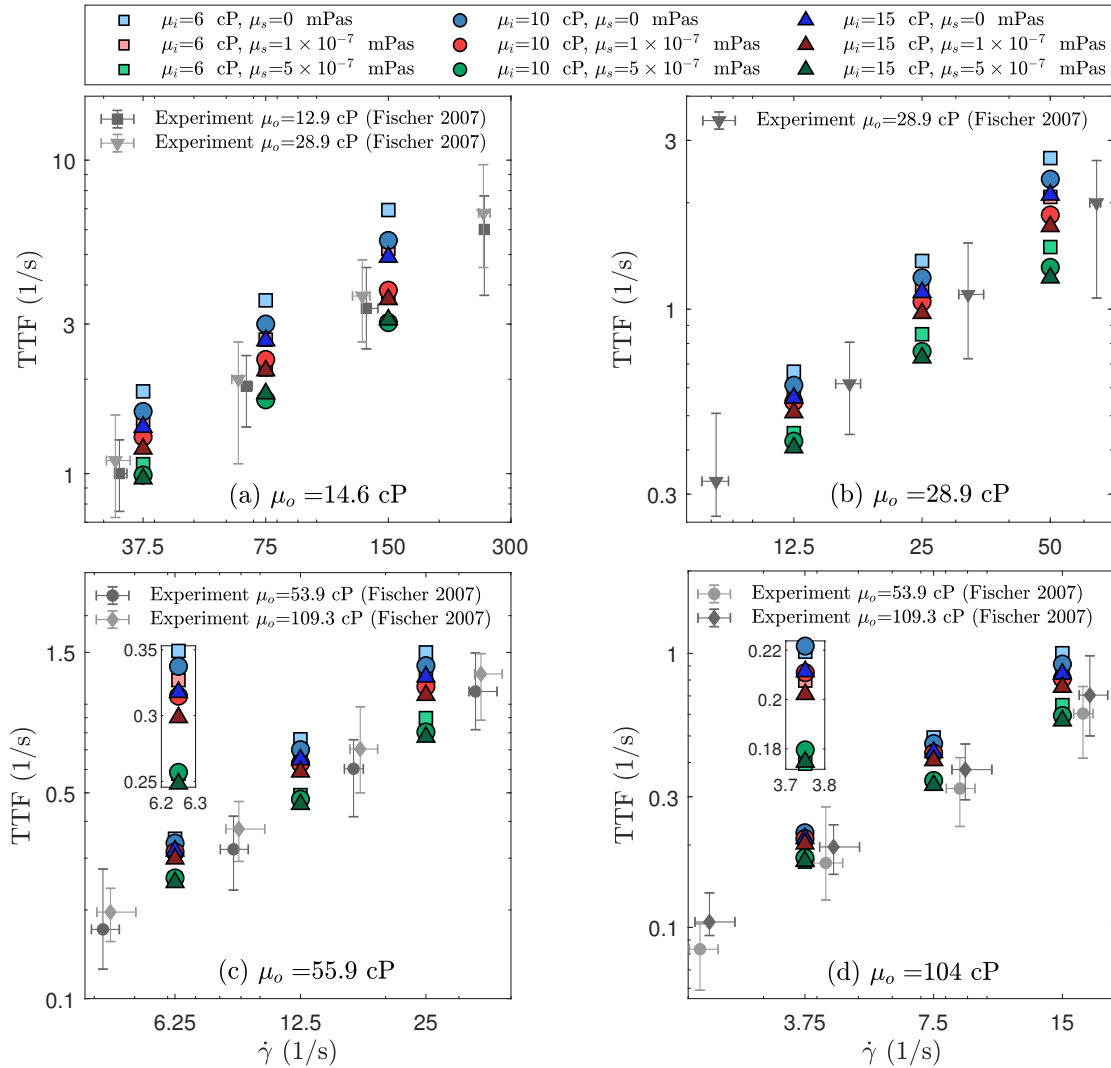


FIGURE 5.5: Effects of membrane viscosity μ_s and interior fluid viscosity μ_i on tank-treading frequency TTF of the RBC in simple shear flow with different exterior fluid viscosities. The error bars for the present results indicate the minimum and maximum values of TTF , while the filled symbols present the mean values of TTF . The gray symbols with error bars indicate the experimental results from Fischer [30], where the measured TTF values for the cells of all 3 donors are included. Insets are also adopted to show more details.

Variations of TTF for all cases in Fig. 5.5 are plotted together in Fig 5.6 to see the general trends in the results. It can be seen that the simulation results reasonably cover the experimental data. Moreover, a high membrane viscosity of $\mu_s = 5 \times 10^{-7}$ mPas yields a favorable agreement at lower shear rates, while a smaller membrane viscosity provides better agreement compared to the experimental results at higher shear rates. This suggests that the RBC membrane exhibits a larger viscosity at low shear rates but a smaller

viscosity at higher shear rates; i.e., the shear-thinning behavior.

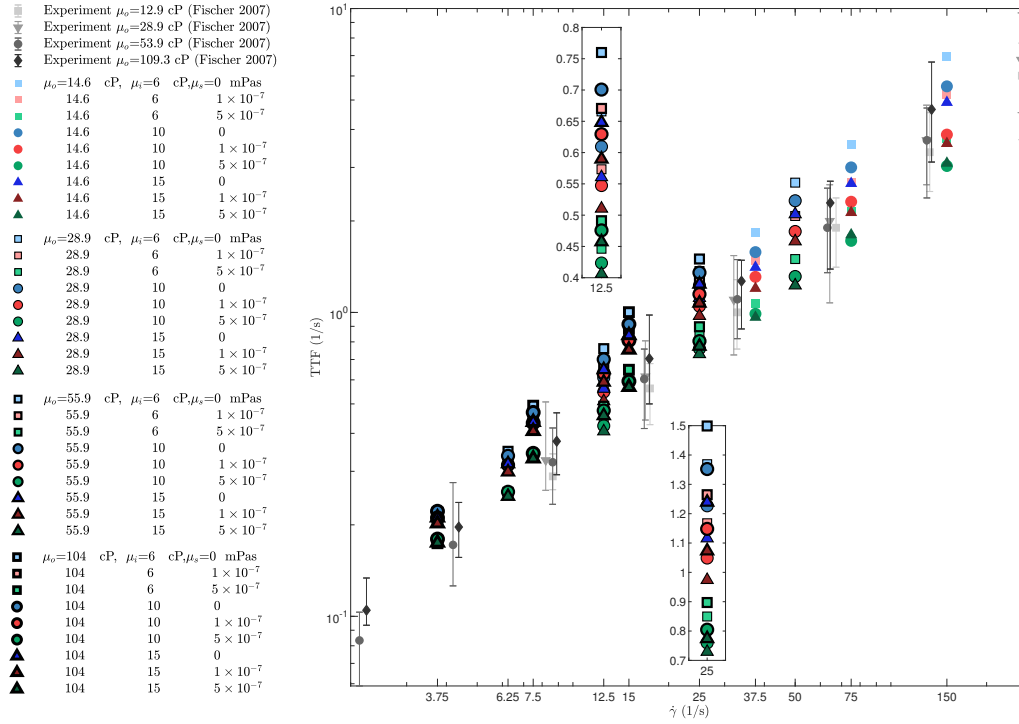


FIGURE 5.6: Variations of TTF with respect to shear rate $\dot{\gamma}$ for different shear flow conditions, membrane viscosities, and interior fluid viscosities. The experimental results from Fischer [30] are also shown for comparison, and the insets are presented to show more details.

5.3.2 RBC Deformation

Variations of the RBC deformation under different shear flow conditions and with various combinations of membrane viscosity and interior fluid viscosity are collected in Fig. 5.7. Unsurprisingly, the cell becomes more elongated at higher shear rates. At higher shear rates, the results are less vulnerable to the oscillations caused by membrane viscosity. Also, we can see that increasing the membrane viscosity leads to lower deformation index. For the highest value of membrane viscosity $\mu_s = 5 \times 10^{-7}$ mPas considered in this study, the cell deformation show remarkable deviations from experiments. As the membrane viscosity reduces, a fairly reasonable agreement can be obtained with experiments. On the contrary, increasing μ_i increases the cell deformation, and the influence is more significant at higher shear rates. From the tank-treading dynamics of spherical capsules in Table 4.1, we observed that increasing μ_i (λ in Table 4.1) reduces the capsule deformation, which seems contradictory to our deformation results for tank-treading RBC.

It should be remarked, however, that here for RBC the deformation index is defined as L_p/B (L_p and B are the projected length and width of the cell in XY plane, respectively), while for the spherical capsule it was defined as $\frac{L-W}{L+W}$ (L and W are the largest and shortest axes in the shear plane, respectively). Therefore, these two definitions of the deformation index are different from each other and their results are not comparable. Although not illustrated here, presenting the deformation of tank-treading RBC using $D = \frac{L-W}{L+W}$ as the deformation index indicates that increasing μ_i reduces D , which is consistent with our observations for tank-treading capsules in Section 4.1.1.

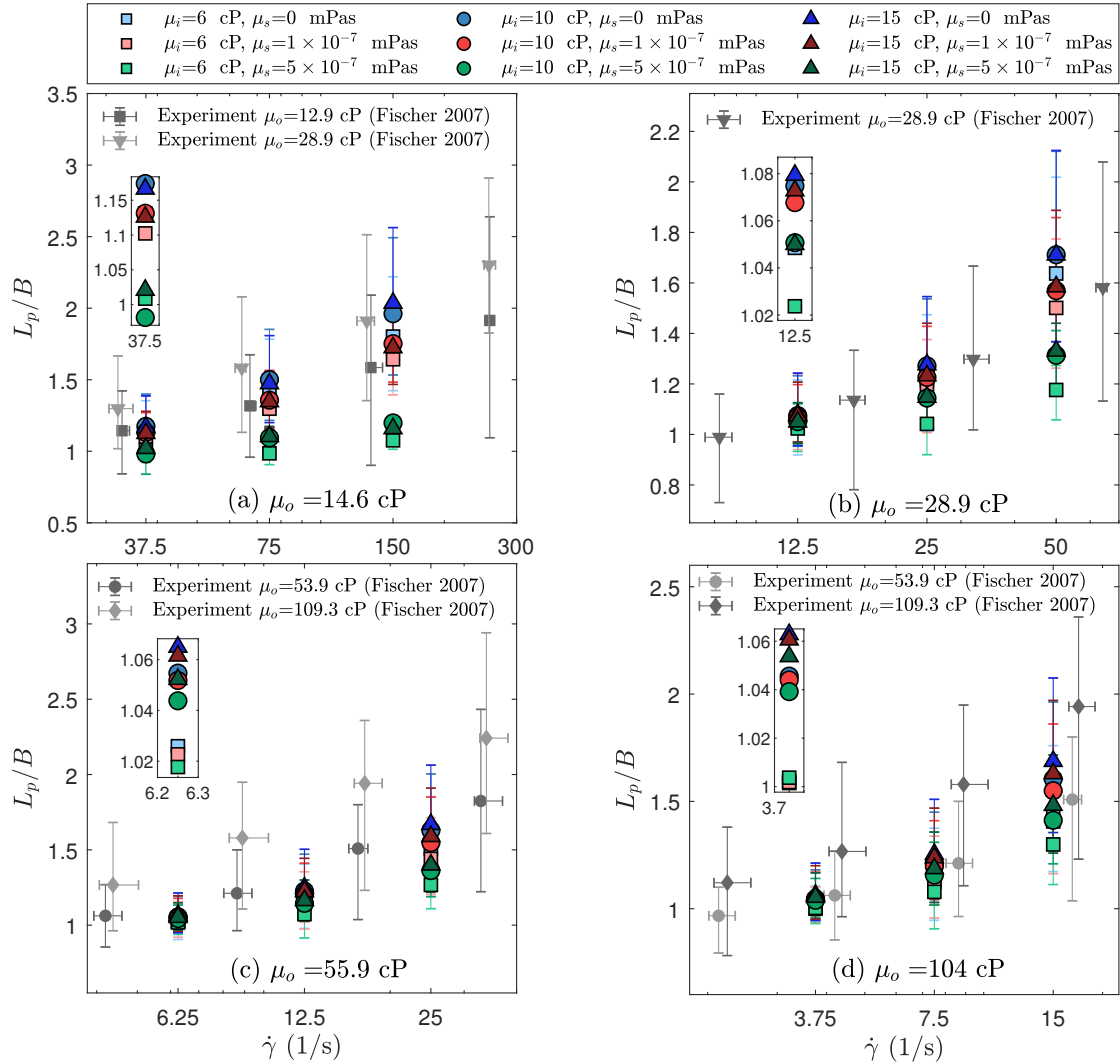


FIGURE 5.7: Comparison of the deformation index obtained from present simulations with experimental results of Fischer [30] for different shear flow conditions. The shear rate is presented in a logarithmic scale and the insets are adopted to present clearer views of the results.

In Fig. 5.7, the shear rate values are smaller at higher exterior fluid viscosities. Hence, it could be useful to observe variations of L_p/B as a function of shear stress $\mu_o\dot{\gamma}$ instead of shear rate $\dot{\gamma}$. Since illustrating all of 108 data points in Fig. 5.7 together could make it difficult to notice the general trends in variations of L_p/B , we present approximate regions covered by each set of (μ_i, μ_s) with respect to shear stress. In this way, linear regressions of maximum and minimum L_p/B values versus $\mu_o\dot{\gamma}$ are performed, which results in two lines for each set of (μ_i, μ_s) . Then, the area between these two lines are presented as a shaded area with corresponding symbols on its vertices, as shown in Fig. 5.8.

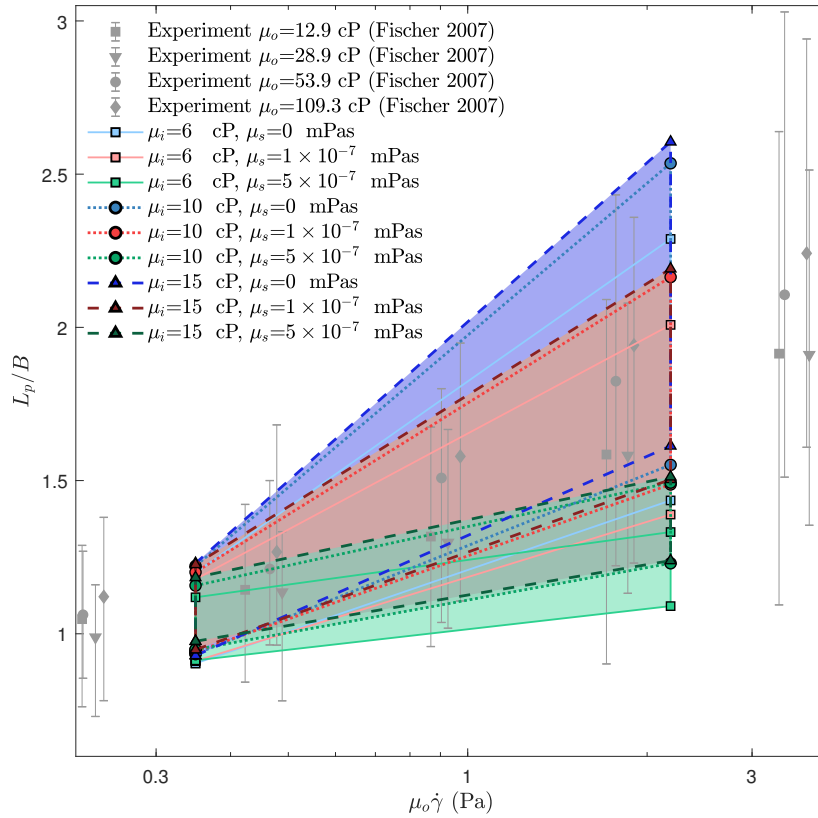


FIGURE 5.8: Impact of membrane viscosity and interior fluid viscosity on the RBC deformation L_p/B with respect to shear stress $\mu_o\dot{\gamma}$. The shaded areas are calculated through linear regression of maximum and minimum values of L_p/B versus $\mu_o\dot{\gamma}$ (see the text for details).

Obviously, larger shear stresses increase the cell deformation for all combinations of membrane and interior fluid viscosities. Moreover, the suppression effect of membrane viscosity on the deformation is evident, especially at higher shear stresses. At low shear stresses, the impacts of both membrane viscosity and interior fluid viscosity seem to be

negligible. This is actually expected since at lower shear stresses the dissipation caused by membrane and/or internal fluid viscosities is also lower. The results in Fig. 5.8 indicates that a favorable agreement can be achieved in comparison to the experiments using $\mu_s \approx 10^{-7}$ mPas and $\mu_i = 10$ cP.

5.3.3 RBC Orientation

Next, we investigate the effects of membrane and interior fluid viscosities on the RBC orientation, as shown in Fig. 5.9.

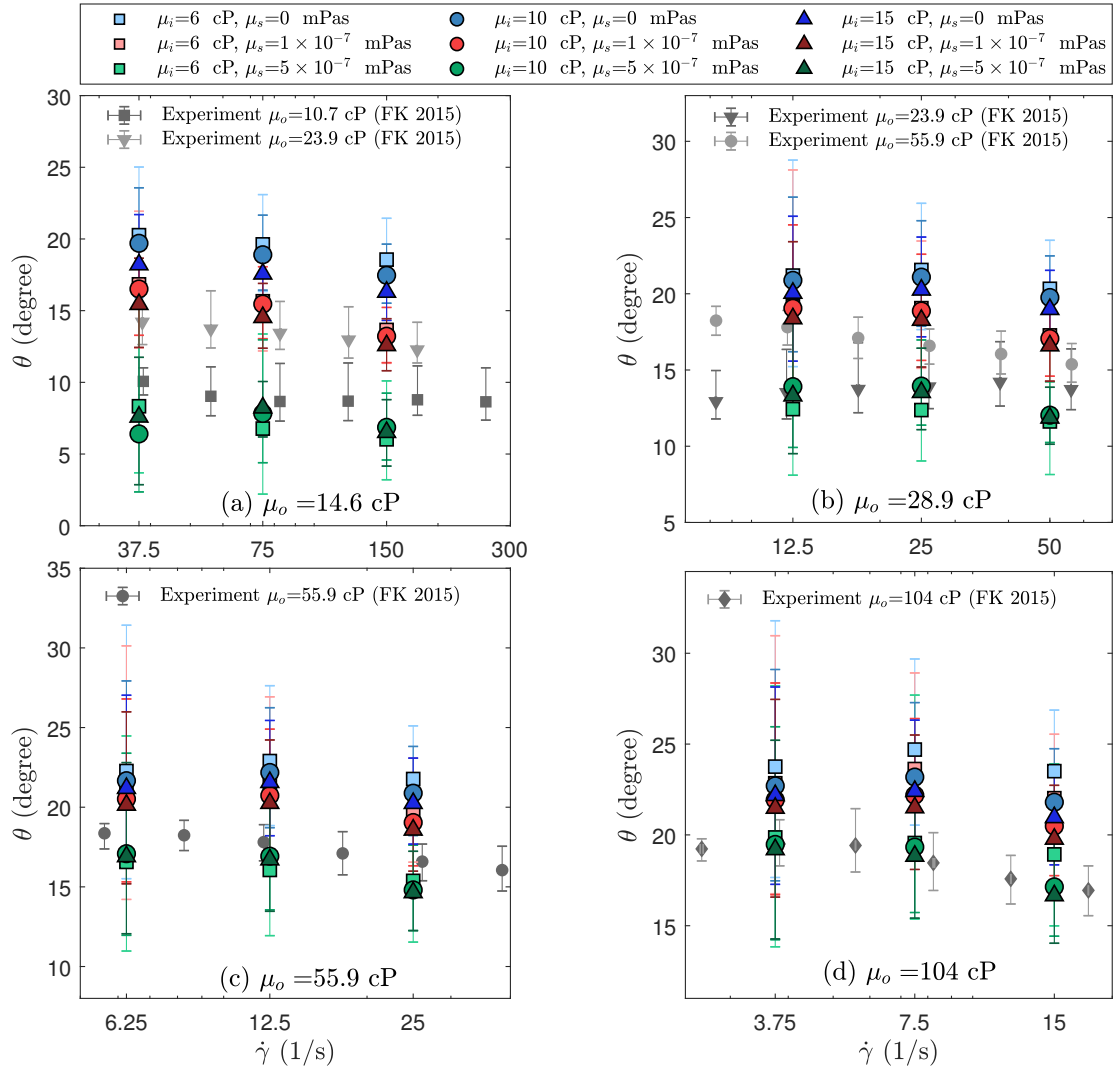


FIGURE 5.9: Sensitivity of the RBC inclination angle to membrane viscosity and interior fluid viscosity for various flow conditions. The experimental results from Fischer and Korzeniewski [49] (FK 2015) are also presented for comparison.

It can be seen from Fig. 5.9 that the inclination angle θ in general decreases with shear rate. This is reasonable since a higher shear rate generates stronger shear stresses on the cell membrane, and thus aligns the deformed cell orientation closer to the flow direction. For a pure elastic membrane, increasing the interior fluid viscosity diminishes the inclination angle, which is consistent with our observations for tank-treading results of spherical capsules in Table 4.1. Similar effect can also be noticed for variations of the inclination angle with membrane viscosity at a constant internal fluid viscosity. However, comparing inclination angle at different μ_i for the same $\mu_s = 5 \times 10^{-7}$ mPas indicates sporadic variations of θ with μ_i . The reason for this behavior could be the intensified oscillations of inclination angle at high membrane viscosity. As mentioned previously, such behaviors have also been reported for tank-treading spherical capsules in simple shear flow [46]. Nevertheless, the differences among the θ values from different μ_i and a relatively high membrane viscosity $\mu_s = 5 \times 10^{-7}$ mPas are relatively insignificant. It can be seen that increasing the interior fluid viscosity without considering the membrane viscosity does not present a favorable comparison with experiments. On the other hand, a remarkable reduction in θ values can be obtained by elevating the membrane viscosity, especially at higher shear rates. Furthermore, the experimental data is well covered by the cell property range ($\mu_i = 6 \sim 15$ cP and $\mu_s = 0 \sim 5 \times 10^{-7}$ mPas) considered in this study without adopting the shear-thinning model for membrane viscosity. Please note that plotting θ versus $\mu_o \dot{\gamma}$ for all cases together yields scatters of data points for both experimental and simulation results. For this reason, we do not have a similar figure for θ as Fig. 5.6 for TTF and Fig. 5.8 for L_p/B .

5.3.4 Assessment of Shear-Thinning Model for Membrane Viscosity

In Chapter 2, it was mentioned that a shear-thinning model for the membrane viscosity was applied in Ref. [62] to fit the simulated TTF values to the experimental measurements for $\mu_o = 12.9$ and 53.9 cP with considering $\mu_i = 10.78$ cP. In this model, a lower membrane viscosity is applied at higher shear rates. A similar approach has also been adopted by Tsubota [64] for $\mu_o = 28.9$ cP with considering $\mu_i = 28.9$ cP. By adjusting the membrane viscosity value, excellent agreements were obtained in these studies for TTF . It should be remarked, however, that these studies did not investigate the effect of the

shear-thinning model on the cell orientation. Furthermore, they tested the model only with specific exterior fluid viscosities, although experimental results are available for $\mu_0 = 12.9, 28.9, 53.9,$ and 109.3 cP. In the following, we examine validity of the shear-thinning model through qualitative comparisons.

At first, one should not treat the experimental results as golden standards; instead one should be aware that they are susceptible to inevitable errors, uncertainties, and intraindividual distributions of cell parameters in the sample. For example, Fischer [30] measured *TTF* values of three different blood samples, and noticeable differences are observed among the results for these three samples. Regarding RBC deformation, Fischer and co-workers [30, 48] measured deformation index of the cells by taking microscopic images of the elongated cells and processing the digitized images to detect the cell geometry using a threshold criterion. However, RBC deformation is a dynamic process and taking images of the cells may not cover the whole range of the deformation experienced by the cell. Processing the images using a threshold criterion may also cause inaccuracy in the measurements. In addition, the authors observed a wide distribution of L_p/B in a single blood sample, and attributed this to fluctuations of the imposed shear rate in experiments and distributions of the membrane shear modulus and membrane viscosity, among others. Concerning RBC inclination angle, Fischer and Korzeniewski [49] measured the cell orientation in a tube flow, which may be different from the cell orientation in a simple shear flow. For instance, in our discussions in Chapter 4 for lateral migration of viscoelastic capsules in tube flow, it has been observed that the capsule inclination angle is slightly higher in tube flow compared to that in simple shear flow (please see Fig. 4.8). Considering all of these uncertainties in the experimental results for tank-treading dynamics of RBCs, it seems inappropriate to pursue a perfect fit of parts of available experimental results by tuning the membrane viscosity as done in Refs. [62, 64].

With that being said, we evaluate the impact of shear-thinning model on tank-treading frequency, deformation, and orientation of RBCs through qualitative comparisons. From the present results in Fig. 5.6 it can be seen that the shear-thinning approach is generally true: at lower shear rates the *TTF* values from $\mu_s = 5 \times 10^{-7}$ mPas are closer to the

experimental results, and as the shear rate increases, $\mu_s = 1 \times 10^{-7}$ mPas yields a better agreement. Nonetheless, a closer look at the results reveals that the *TTF* values from $\mu_i = 6$ cP and $\mu_s = 5 \times 10^{-7}$ mPas (green squares) presents a fairly good agreement in comparison to the experimental results for all values of the exterior fluid viscosity. Regarding the deformation index of the RBC in Fig. 5.8, it can be seen that the L_p/B values from $\mu_i = 6$ cP and $\mu_s = 1 \times 10^{-7}$ mPas show a relatively good agreement with experimental results suggesting that the shear-thinning model might not be necessary. For the RBC inclination angle in Fig. 5.9, reasonable agreement with experiments are also observed for the membrane viscosity value between 10^{-7} and 5×10^{-7} mPas.

Based on the above discussions for dependency of the tank-treading frequency, deformation, and inclination angle on the membrane viscosity, it seems that considering a membrane viscosity value between 10^{-7} and 5×10^{-7} mPas with $\mu_i = 6$ cP can reproduce the experimental results for RBC tank-treading dynamics from Refs. [30, 48, 49] to a sufficient level. Here, we want to emphasize again that obtaining a precise agreement with experiments is not only unnecessary but also improper considering the vulnerability of the experimental results to various errors and uncertainties. It should also be mentioned that we do not deny the possible shear-thinning behavior of membrane viscosity. Instead, our results of *TTF* in Fig. 5.5 suggest that the RBC membrane may exhibit a shear-thinning fashion in viscosity; however, to model the non-Newtonian behavior of membrane viscosity and further to determine the model coefficient values, more thorough and comprehensive studies are necessary.

5.4 Summary and Concluding Remarks

In this chapter, 3D simulations have been performed for the tank-treading dynamics of RBC in simple shear flow. Validation tests are conducted for stretching process of the RBC in optical tweezers and a good agreement is obtained in comparison to the experiments. The dynamics of RBCs in simple shear flow has been investigated by considering different combinations of membrane viscosity and interior fluid viscosity, and various shear flow conditions. Unlike previous publications, all characteristics of the cell dynamics (tank-treading frequency, deformation, and inclination angle) have been considered

and the simulations are performed over a wide range of flow and cell parameters. The results indicate that the tank-treading frequency TTF reduces with the membrane viscosity μ_s and internal fluid viscosity μ_i . Nonetheless, increasing the interior fluid viscosity alone cannot efficiently slow down the tank-treading motion to obtain proper agreement with experiments. This accentuates that membrane viscosity is an essential ingredient in dynamics of RBCs, which cannot be represented by increased internal fluid viscosity. Furthermore, membrane viscosity exhibits a relatively strong suppression influence on the cell deformation index L_p/B , while the interior fluid viscosity increases L_p/B . For the inclination angle θ , both membrane viscosity and interior fluid viscosity reduce θ , which is consistent with previous observations for tank-treading spherical capsules in shear flow.

Regarding the inherent errors and uncertainties in experimental measurements for tank-treading RBCs, we pointed out that it is inappropriate to pursue a perfect fit to parts of the available experimental results by adjusting the membrane viscosity. In fact, our results suggest that compared to the experiments, a reasonable agreement for all the key tank-treading parameters could be obtained by considering fixed values for membrane viscosity rather than a shear dependent membrane viscosity. Therefore, more research is required to further understanding the membrane viscous behaviors.

Chapter 6

Summary and Future Research

6.1 Summary

In this thesis, I have presented the general background of the RBC behaviors in microcirculation in Chapter 1. The relevant literature for RBC flow modeling and simulations and experimental measuring techniques has been reviewed in Chapter 2. In addition, RBC membrane mechanics and the numerical techniques employed in my research, including the lattice Boltzmann method and immersed boundary method, have been described in details in Chapter 3.

The lateral migration of viscoelastic capsules in tube flow has been investigated in Chapter 4. The impacts of the three control parameters, the interior-exterior viscosity ratio λ , the membrane viscosity represented by Bq_s , and the capillary number Ca , on the migration processes and capsule dynamics have been examined systematically. It is observed that unlike solid particles, the capsule continuously migrates toward the centerline. The capsule deformation and inclination angle decrease at higher λ and/or Bq_s , which leads to slower migration rate. Further, the effect of membrane viscosity on the migration processes escalates at higher Ca . The results show that the capsule rotation period is mainly related to the local shear condition. Although viscosity ratio and membrane viscosity have similar suppression impacts on the capsule deformation and migration, distinctive differences exist in the capsule dynamic characteristics, especially for large membrane viscosity values. This suggests that the membrane viscous effects on capsule dynamics

cannot be compensated by using an elevated interior fluid viscosity. These findings could be of interest for studying RBC behaviors in microcirculation.

In Chapter 5 we have considered realistic properties of RBC in 3D simulations to examine the tank-treading dynamics of the RBC in simple shear flows. Detailed comparisons are made with experiments over a wide range of exterior fluid viscosity and shear rate. Our results show that both membrane viscosity and interior fluid viscosity decrease TTF . Nevertheless, TTF exhibited much stronger dependency on membrane viscosity than interior fluid viscosity. This stronger influence of membrane viscosity has also been noticed for the cell deformation and inclination angle. In particular, raising the interior fluid viscosity alone cannot yield a reasonable agreement with experiments in terms of the inclination angle implying that the membrane viscosity cannot be neglected. Moreover, our results suggest that a fairly good agreement with experiments can be obtained using invariant membrane viscosity value without adopting the shear-thinning model for membrane viscosity.

6.2 Future Research

As mentioned in Chapter 2 of this thesis, formation of the cell free layer induced by lateral migration of RBCs plays a key role in hemodynamics. However, we simulated only the lateral migration of isolated spherical capsules in Chapter 4. It is of future interest to extend our simulations to multiple cells to elucidate the role of membrane viscosity in rheological behaviors of blood based on the microhydrodynamics of individual cells. In particular, the impacts of membrane viscosity on migration process of cells, development of the CFL, variations of the apparent viscosity, and trajectory of individual cells could be examined. Furthermore, studying the interplay between membrane viscosity and other properties such as viscosity ratio, capillary number, hematocrit, and cell-cell interactions could be of importance. These aspects can be further investigated for more complex situations, such as multiple RBC flows in microvascular networks with several bifurcating and converging microvessels.

In addition, our analyses for the effects of membrane viscosity on tank-treading behaviors

of RBC in Chapter 5 was limited to a single cell. For future research, one can consider a suspension of RBCs in a simple shear flow. It would be interesting to examine how the observed suppression effects of membrane viscosity on the single cell dynamics (tank-treading frequency, deformation, and orientation) impact on the apparent viscosity, shear stress distribution, and shear-thinning behavior of blood.

In principle, the methodology and our current computer programs can handle multiple cells to simulate dilute or dense suspensions. However, the execution time of simulations can be of concern as cell population and computational domain increase. Currently, our simulation codes are parallelized using OpenMP for shared memory. Parallelizing the codes using MPI or combinations of MPI and OpenMP may help to decrease the execution time.

References

- [1] A. S. Popel and P. C. Johnson. "Microcirculation and hemorheology". In: *Annual Review of Fluid Mechanics* 37 (2005), p. 43.
- [2] F. S. Laroux, K. P. Pavlick, R. E. Wolf, and M. B. Grisham. "Dysregulation of intestinal mucosal immunity: implications in inflammatory bowel disease". In: *Physiology* 16.6 (2001), p. 272.
- [3] P. Zarda, S. Chien, and R. Skalak. "Elastic deformations of red blood cells". In: *Journal of Biomechanics* 10.4 (1977), p. 211.
- [4] L. Thomas. In: *Blood Plasma Components and Function* (accessed Oct 14, 2020).
- [5] A. C. Swanepoel and E. Pretorius. "Scanning electron microscopy analysis of erythrocytes in thromboembolic ischemic stroke". In: *International Journal of Laboratory Hematology* 34.2 (2012), p. 185.
- [6] M. Dao, C. T. Lim, and S. Suresh. "Mechanics of the human red blood cell deformed by optical tweezers". In: *Journal of the Mechanics and Physics of Solids* 51.11-12 (2003), p. 2259.
- [7] X. Li, Z. Peng, H. Lei, M. Dao, and G. E. Karniadakis. "Probing red blood cell mechanics, rheology and dynamics with a two-component multi-scale model". In: *Philosophical Transactions of the Royal Society A: Mathematical, Physical and Engineering Sciences* 372.2021 (2014), p. 20130389.
- [8] R. Skalak, A. Tozeren, R. Zarda, and S. Chien. "Strain energy function of red blood cell membranes". In: *Biophysical Journal* 13.3 (1973), p. 245.
- [9] O. Oulaid, A. K. W. Saad, P. S. Aires, and J. Zhang. "Effects of shear rate and suspending viscosity on deformation and frequency of red blood cells tank-treading

- in shear flows". In: *Computer Methods in Biomechanics and Biomedical Engineering* 19.6 (2016), p. 648.
- [10] R. P. Rand and A. Burton. "Mechanical properties of the red cell membrane: I. Membrane stiffness and intracellular pressure". In: *Biophysical Journal* 4.2 (1964), p. 115.
- [11] R. Rand. "Mechanical properties of the red cell membrane: II. Viscoelastic breakdown of the membrane". In: *Biophysical Journal* 4.4 (1964), p. 303.
- [12] E. Evans and Y. C. Fung. "Improved measurements of the erythrocyte geometry". In: *Microvascular Research* 4.4 (1972), p. 335.
- [13] E. Evans and R. Hochmuth. "Membrane viscoelasticity". In: *Biophysical Journal* 16.1 (1976), p. 1.
- [14] R. Tran-Son-Tay, S. Suter, and P. Rao. "Determination of red blood cell membrane viscosity from rheoscopic observations of tank-treading motion". In: *Biophysical Journal* 46.1 (1984), p. 65.
- [15] M. Puig-de Morales-Marinkovic, K. T. Turner, J. P. Butler, J. J. Fredberg, and S. Suresh. "Viscoelasticity of the human red blood cell". In: *American Journal of Physiology-Cell Physiology* 293.2 (2007), p. 597.
- [16] R. Hochmuth and R. Waugh. "Erythrocyte membrane elasticity and viscosity". In: *Annual Review of Physiology* 49.1 (1987), p. 209.
- [17] S. Suresh. "Mechanical response of human red blood cells in health and disease: Some structure-property-function relationships". In: *Journal of Materials Research* 21.8 (2006), p. 1871.
- [18] T. Fischer and H. Schmid-Schönbein. "Tank tread motion of red cell membranes in viscometric flow: behavior of intracellular and extracellular markers (with film)". In: *Red Cell Rheology*. Springer, 1978, p. 347.
- [19] J. Zhang, P. C. Johnson, and A. S. Popel. "An immersed boundary lattice Boltzmann approach to simulate deformable liquid capsules and its application to microscopic blood flows". In: *Physical Biology* 4.4 (2007), p. 285.

- [20] M. Abkarian, M. Faivre, and A. Viallat. "Swinging of red blood cells under shear flow". In: *Physical Review Letters* 98.18 (2007), p. 188302.
- [21] J. Zhang, P. C. Johnson, and A. S. Popel. "Simulating microscopic hemodynamics and hemorheology with the immersed-boundary lattice-Boltzmann method". In: *Computational Hydrodynamics of Capsules and Biological Cells*. CRC, Boca Raton (2010).
- [22] R. Fahraeus and T. Lindqvist. "The viscosity of the blood in narrow capillary tubes". In: *American Journal of Physiology-Legacy Content* 96.3 (1931), p. 562.
- [23] C. Pozrikidis. "Axisymmetric motion of a file of red blood cells through capillaries". In: *Physics of Fluids* 17.3 (2005), p. 031503.
- [24] R. M. Hochmuth. "Micropipette aspiration of living cells". In: *Journal of Biomechanics* 33.1 (2000), p. 15.
- [25] D. Rugar and P. Hansma. "Atomic force microscopy". In: *Physics Today* 43.10 (1990), p. 23.
- [26] S. Suter, R. Gardner, C. Boylan, G. Carroll, K. Chang, J. Marvel, C Kilo, B Gonen, and J. Williamson. "Age-related changes in deformability of human erythrocytes". In: *Blood* 65 (1985), p. 275.
- [27] S. Henon, G. Lenormand, A. Richert, and F. Gallet. "A new determination of the shear modulus of the human erythrocyte membrane using optical tweezers". In: *Biophysical Journal* 76.2 (1999), p. 1145.
- [28] J. P. Mills, L. Qie, M. Dao, C. T. Lim, and S. Suresh. "Nonlinear elastic and viscoelastic deformation of the human red blood cell with optical tweezers". In: *Molecular and Cellular Biomechanics* 1.3 (2004), p. 169.
- [29] J. Dobbe, G. Streekstra, M. Hardeman, C. Ince, and C. Grimbergen. "Measurement of the distribution of red blood cell deformability using an automated rheoscope". In: *Cytometry: The Journal of the International Society for Analytical Cytology* 50.6 (2002), p. 313.
- [30] T. M. Fischer. "Tank-tread frequency of the red cell membrane: dependence on the viscosity of the suspending medium". In: *Biophysical Journal* 93.7 (2007), p. 2553.

- [31] G. Tomaiuolo. "Biomechanical properties of red blood cells in health and disease towards microfluidics". In: *Biomicrofluidics* 8.5 (2014), p. 051501.
- [32] P. Bagchi and R. M. Kalluri. "Dynamic rheology of a dilute suspension of elastic capsules: effect of capsule tank-treading, swinging and tumbling". In: *Journal of Fluid Mechanics* 669 (2011), p. 498.
- [33] S. R. Keller and R. Skalak. "Motion of a tank-treading ellipsoidal particle in a shear flow". In: *Journal of Fluid Mechanics* 120 (1982), p. 27.
- [34] M. Ju, S. S. Ye, B. Namgung, S. Cho, H. T. Low, H. L. Leo, and S. Kim. "A review of numerical methods for red blood cell flow simulation". In: *Computer Methods in Biomechanics and Biomedical Engineering* 18.2 (2015), p. 130.
- [35] J. B. Freund. "Numerical simulation of flowing blood cells". In: *Annual Review of Fluid Mechanics* 46 (2014), p. 67.
- [36] C. Pozrikidis. *Boundary Integral and Singularity Methods for Linearized Viscous Flow*. Cambridge University Press, 1992.
- [37] S. Ramanujan and C. Pozrikidis. "Deformation of liquid capsules enclosed by elastic membranes in simple shear flow: large deformations and the effect of fluid viscosities". In: *Journal of Fluid Mechanics* 361 (1998), p. 117.
- [38] H. Krüger. *Computer Simulation Study of Collective Phenomena in Dense Suspensions of Red Blood Cells Under Shear*. Springer Science & Business Media, 2012.
- [39] D. A. Fedosov, B. Caswell, and G. E. Karniadakis. "A multiscale red blood cell model with accurate mechanics, rheology, and dynamics". In: *Biophysical Journal* 98.10 (2010), p. 2215.
- [40] C. S. Peskin. "Numerical analysis of blood flow in the heart". In: *Journal of Computational Physics* 25.3 (1977), p. 220.
- [41] C. D. Eggleton and A. S. Popel. "Large deformation of red blood cell ghosts in a simple shear flow". In: *Physics of Fluids* 10.8 (1998), p. 1834.
- [42] R. Mittal and G. Iaccarino. "Immersed boundary methods". In: *Annual Review of Fluid Mechanics* 37 (2005), p. 239.

- [43] J. Zhang, P. C. Johnson, and A. S. Popel. "Red blood cell aggregation and dissociation in shear flows simulated by lattice Boltzmann method". In: *Journal of Biomechanics* 41.1 (2008), p. 47.
- [44] P. Balogh and P. Bagchi. "A computational approach to modeling cellular-scale blood flow in complex geometry". In: *Journal of Computational Physics* 334 (2017), p. 280.
- [45] S. K. Doddi and P. Bagchi. "Three-dimensional computational modeling of multiple deformable cells flowing in microvessels". In: *Physical Review E* 79.4 (2009), p. 046318.
- [46] P. Li and J. Zhang. "Similar but distinct roles of membrane and interior fluid viscosities in capsule dynamics in shear flows". In: *Cardiovascular Engineering and Technology* (2021), p. 1.
- [47] T. M. Fischer, M. Stohr-Lissen, and H. Schmid-Schonbein. "The red cell as a fluid droplet: tank tread-like motion of the human erythrocyte membrane in shear flow". In: *Science* 202.4370 (1978), p. 894.
- [48] T. M. Fischer and R. Korzeniewski. "Effects of shear rate and suspending medium viscosity on elongation of red cells tank-treading in shear flow". In: *Cytometry Part A* 79.11 (2011), p. 946.
- [49] T. M. Fischer and R. Korzeniewski. "Angle of inclination of tank-treading red cells: dependence on shear rate and suspending medium". In: *Biophysical Journal* 108.6 (2015), p. 1352.
- [50] C. Pozrikidis. "Numerical simulation of the flow-induced deformation of red blood cells". In: *Annals of Biomedical Engineering* 31.10 (2003), p. 1194.
- [51] Y. Sui, Y. Chew, P. Roy, Y. Cheng, and H. Low. "Dynamic motion of red blood cells in simple shear flow". In: *Physics of Fluids* 20.11 (2008), p. 112106.
- [52] A. Z. Yazdani, R. M. Kalluri, and P. Bagchi. "Tank-treading and tumbling frequencies of capsules and red blood cells". In: *Physical Review E* 83.4 (2011), p. 046305.

- [53] D. Barthes-Biesel and H. Sgaier. "Role of membrane viscosity in the orientation and deformation of a spherical capsule suspended in shear flow". In: *Journal of Fluid Mechanics* 160 (1985), p. 119.
- [54] A. Yazdani and P. Bagchi. "Influence of membrane viscosity on capsule dynamics in shear flow". In: *Journal of Fluid Mechanics* 718 (2013), p. 569.
- [55] J. Gounley and Y. Peng. "Computational modeling of membrane viscosity of red blood cells". In: *Communications in Computational Physics* 17.4 (2015), p. 1073.
- [56] P. Li and J. Zhang. "A finite difference method with sub-sampling for immersed boundary simulations of the capsule dynamics with viscoelastic membranes". In: *International Journal for Numerical Methods in Biomedical Engineering* (2019), p. 3200.
- [57] P. Li and J. Zhang. "Finite-difference and integral schemes for Maxwell viscous stress calculation in immersed boundary simulations of viscoelastic membranes". In: *Biomechanics and Modeling in Mechanobiology* 19.6 (2020), p. 2667.
- [58] F. Guglietta, M. Behr, L. Biferale, G. Falcucci, and M. Sbragaglia. "On the effects of membrane viscosity on transient red blood cell dynamics". In: *Soft Matter* 16.26 (2020), p. 6191.
- [59] F. Guglietta, M. Behr, G. Falcucci, and M. Sbragaglia. "Loading and relaxation dynamics for a red blood cell". In: *Soft Matter* (2021).
- [60] D. A. Fedosov, H. Noguchi, and G. Gompper. "Multiscale modeling of blood flow: from single cells to blood rheology". In: *Biomechanics and Modeling in Mechanobiology* 13.2 (2014), p. 239.
- [61] F. Guglietta, M. Behr, L. Biferale, G. Falcucci, and M. Sbragaglia. "Lattice Boltzmann simulations on the tumbling to tank-treading transition: effects of membrane viscosity". In: *Philosophical Transactions of the Royal Society A* 379.2208 (2021), p. 20200395.
- [62] P. Matteoli, F. Nicoud, and S. Mendez. "Impact of the membrane viscosity on the tank-treading behavior of red blood cells". In: *Physical Review Fluids* 6.4 (2021), p. 043602.

- [63] R. M. Hochmuth, P. R. Worthy, and E. A. Evans. "Red cell extensional recovery and the determination of membrane viscosity". In: *Biophysical Journal* 26.1 (1979), p. 101.
- [64] K. i. Tsubota. "Elongation deformation of a red blood cell under shear flow as stretch testing". In: *Journal of the Mechanics and Physics of Solids* 152 (2021), p. 104345.
- [65] D. Di Carlo, D. Irimia, R. G. Tompkins, and M. Toner. "Continuous inertial focusing, ordering, and separation of particles in microchannels". In: *Proceedings of the National Academy of Sciences* 104.48 (2007), p. 18892.
- [66] A. Farutin and C. Misbah. "Analytical and numerical study of three main migration laws for vesicles under flow". In: *Physical Review Letters* 110.10 (2013), p. 108104.
- [67] A. Helmy and D. Barthes-Biesel. "Migration of a spherical capsule freely suspended in an unbounded parabolic flow". In: *de Mécanique Théorique et Appliquée* (1982), p. 859.
- [68] C. Pozrikidis. "Numerical simulation of cell motion in tube flow". In: *Annals of Biomedical Engineering* 33.2 (2005), p. 165.
- [69] S. Nix, Y. Imai, and T. Ishikawa. "Lateral migration of a capsule in a parabolic flow". In: *Journal of Biomechanics* 49.11 (2016), p. 2249.
- [70] S. K. Doddi and P. Bagchi. "Lateral migration of a capsule in a plane Poiseuille flow in a channel". In: *International Journal of Multiphase Flow* 34 (2008), p. 966.
- [71] S. Succi. *The lattice Boltzmann Equation: for Fluid Dynamics and Beyond*. Oxford University Press, 2001.
- [72] X. He, Q. Zou, L. S. Luo, and M. Dembo. "Analytic solutions of simple flows and analysis of nonslip boundary conditions for the lattice Boltzmann BGK model". In: *Journal of Statistical Physics* 87.1-2 (1997), p. 115.
- [73] P. L. Bhatnagar, E. P. Gross, and M. Krook. "A model for collision processes in gases. I. Small amplitude processes in charged and neutral one-component systems". In: *Physical Review* 94.3 (1954), p. 511.

- [74] J. M. Buick. "Lattice Boltzmann Methods in Interfacial Wave Modelling". PhD thesis. University of Edinburgh, 1997.
- [75] J. Zhang. "Lattice Boltzmann method for microfluidics: models and applications". In: *Microfluidics and Nanofluidics* 10.1 (2011), p. 1.
- [76] C. S. Peskin. "The immersed boundary method". In: *Acta Numerica* 11 (2002), p. 479.
- [77] T. Krüger, F. Varnik, and D. Raabe. "Efficient and accurate simulations of deformable particles immersed in a fluid using a combined immersed boundary lattice Boltzmann finite element method". In: *Computers and Mathematics with Applications* 61.12 (2011), p. 3485.
- [78] M. Styner, I. Oguz, S. Xu, C. Brechbühler, D. Pantazis, J. J. Levitt, M. E. Shenton, and G. Gerig. "Framework for the statistical shape analysis of brain structures using SPHARM-PDM". In: *The Insight Journal* 1071 (2006), p. 242.
- [79] J. M. Charrier, S. Shrivastava, and R. Wu. "Free and constrained inflation of elastic membranes in relation to thermoforming—non-axisymmetric problems". In: *The Journal of Strain Analysis for Engineering Design* 24.2 (1989), p. 55.
- [80] P. Bagchi, P. C. Johnson, and A. S. Popel. "Computational fluid dynamic simulation of aggregation of deformable cells in a shear flow". In: *Journal of Biomechanical Engineering* 127.7 (2005), p. 1070.
- [81] X. Li and K. Sarkar. "Front tracking simulation of deformation and buckling instability of a liquid capsule enclosed by an elastic membrane". In: *Journal of Computational Physics* 227.10 (2008), p. 4998.
- [82] D. Fedosov, B. Caswell, G. Karniadakis, and C. Pozrikidis. *Dissipative Particle Dynamics Modeling of Red Blood Cells*. CRC Press Boca Raton, FL, 2010, p. 183.
- [83] J. Gounley, G. Boedec, M. Jaeger, and M. Leonetti. "Influence of surface viscosity on droplets in shear flow". In: *Journal of Fluid Mechanics* 791 (2016), p. 464.
- [84] C. Pozrikidis. "Effects of surface viscosity on the finite deformation of a liquid drop and the rheology of dilute emulsions in simple shearing flow". In: *Journal of Non-Newtonian Fluid Mechanics* 51.2 (1994), p. 161.

- [85] T. Secomb and R. Skalak. "Surface flow of viscoelastic membranes in viscous fluids". In: *The Quarterly Journal of Mechanics and Applied Mathematics* 35.2 (1982), p. 233.
- [86] D. Barthès-Biesel. "Motion and deformation of elastic capsules and vesicles in flow". In: *Annual Review of Fluid Mechanics* 48 (2016), p. 25.
- [87] S. P. Marques and G. J. Creus. *Computational Viscoelasticity*. Springer Science & Business Media, 2012.
- [88] E. Foessel, J. Walter, A. Salsac, and D. Barthès-Biesel. "Influence of internal viscosity on the large deformation and buckling of a spherical capsule in a simple shear flow". In: *Journal of Fluid Mechanics* 672 (2011), p. 477.
- [89] E. Lac, D. Barthes-Biesel, N. Pelekasis, and J. Tsamopoulos. "Spherical capsules in three-dimensional unbounded Stokes flows: effect of the membrane constitutive law and onset of buckling". In: *Journal of Fluid Mechanics* 516 (2004), p. 303.
- [90] G. Segre and A. Silberberg. "Behaviour of macroscopic rigid spheres in Poiseuille flow Part 2. Experimental results and interpretation". In: *Journal of Fluid Mechanics* 14.1 (1962), p. 136.
- [91] J. A. Schonberg and E. Hinch. "Inertial migration of a sphere in Poiseuille flow". In: *Journal of Fluid Mechanics* 203 (1989), p. 517.
- [92] W. P. Breugem. "A second-order accurate immersed boundary method for fully resolved simulations of particle-laden flows". In: *Journal of Computational Physics* 231.13 (2012), p. 4469.
- [93] C. R. Choi and C. N. Kim. "Inertial migration and multiple equilibrium positions of a neutrally buoyant spherical particle in Poiseuille flow". In: *Korean Journal of Chemical Engineering* 27.4 (2010), p. 1076.
- [94] B. H. Yang, J. Wang, D. D. Joseph, H. H. Hu, T. Pan, and R. Glowinski. "Migration of a sphere in tube flow". In: *Journal of Fluid Mechanics* 540 (2005), p. 109.
- [95] T. W. Pan and R. Glowinski. "Direct simulation of the motion of neutrally buoyant balls in a three-dimensional Poiseuille flow". In: *Comptes Rendus Mécanique* 333.12 (2005), p. 884.

- [96] A. Rezghi and J. Zhang. "A counter-extrapolation approach for the boundary velocity calculation in immersed boundary simulations". In: *International Journal of Computational Fluid Dynamics* 35.4 (2021), p. 248.
- [97] A. H. Raffiee, S. Dabiri, and A. M. Ardekani. "Elasto-inertial migration of deformable capsules in a microchannel". In: *Biomicrofluidics* 11 (2017), p. 064113.
- [98] J. D. Bronzino. *Biomedical Engineering Handbook*. Vol. 2. CRC Press, 1999.
- [99] R. K. Singh, X. Li, and K. Sarkar. "Lateral migration of a capsule in plane shear near a wall". In: *Journal of Fluid Mechanics* 739 (2014), p. 421.
- [100] T. Krüger, D. Holmes, and P. V. Coveney. "Deformability-based red blood cell separation in deterministic lateral displacement devices—A simulation study". In: *Biomicrofluidics* 8.5 (2014), p. 054114.
- [101] S. Suresh, J. Spatz, J. P. Mills, A. Micoulet, M. Dao, C. Lim, M. Beil, and T. Seufferlein. "Connections between single-cell biomechanics and human disease states: gastrointestinal cancer and malaria". In: *Acta Biomaterialia* 1.1 (2005), p. 15.
- [102] D. Cordasco, A. Yazdani, and P. Bagchi. "Comparison of erythrocyte dynamics in shear flow under different stress-free configurations". In: *Physics of Fluids* 26.4 (2014), p. 041902.
- [103] D. Cordasco and P. Bagchi. "Orbital drift of capsules and red blood cells in shear flow". In: *Physics of Fluids* 25.9 (2013), p. 091902.
- [104] W. Dodson III and P. Dimitrakopoulos. "Tank-treading of erythrocytes in strong shear flows via a nonstiff cytoskeleton-based continuum computational modeling". In: *Biophysical Journal* 99.9 (2010), p. 2906.
- [105] B. L. McClain, I. J. Finkelstein, and M. Fayer. "Vibrational echo experiments on red blood cells: comparison of the dynamics of cytoplasmic and aqueous hemoglobin". In: *Chemical Physics Letters* 392.4-6 (2004), p. 324.